Tran-SET

Transportation Consortium of South-Central States

Solving Emerging Transportation Resiliency, Sustainability, and Economic Challenges through the Use of Innovative Materials and Construction Methods: From Research to Implementation

Bridge Deck Inspection Using Small Unmanned Aircraft Systems Based Airborne Imaging Techniques

Project No. 19STUNM04

Lead University: University of New Mexico

Final Report

November 2020

Disclaimer

The contents of this report reflect the views of the authors, who are responsible for the facts and the accuracy of the information presented herein. This document is disseminated in the interest of information exchange. The report is funded, partially or entirely, by a grant from the U.S. Department of Transportation's University Transportation Centers Program. However, the U.S. Government assumes no liability for the contents or use thereof.

Acknowledgements

The authors would like to express their sincere thanks and gratitude to the students who participated in this research project, including Caleb Garrett and Tyler Eshelman. The authors would also like to thank Mr. Timothy Parker from the New Mexico Department of Transportation District 2 and George Baca from PSB Engineering. The authors would also like to thank Dr. Mahmoud Taha, Dr. Christopher Lippitt, and Dr. David Hadwiger for serving as the Project Review Committee.

TECHNICAL DOCUMENTATION PAGE

1. Project No.	2. Government Accession No.	3. Recipient's Catalog No.
19STUNM04		

4. Title and Subtitle	5. Report Date
Bridge Deck Inspection Using Small Unmanned Aircraft Systems Based Airborne Imaging Techniques	Nov. 2020
	6. Performing Organization Code
7. Author(s)	**8. Performing Organization Report No.**
PI: Su Zhang https://orcid.org/0000-0002-0396-2518 Co-PI: Shirley V. Baros https://orcid.org/0000-0002-0842-1219 Co-PI: Susan Bogus Halter https://orcid.org/0000-0003-1685-6367	
9. Performing Organization Name and Address	**10. Work Unit No. (TRAIS)**
Transportation Consortium of South-Central States (Tran-SET) University Transportation Center for Region 6 3319 Patrick F. Taylor Hall, Louisiana State University, Baton Rouge, LA 70803	**11. Contract or Grant No.** 69A3551747106
12. Sponsoring Agency Name and Address	**13. Type of Report and Period Covered**
United States of America Department of Transportation Research and Innovative Technology Administration	Final Research Report Aug. 2019 – Aug. 2020
	14. Sponsoring Agency Code

15. Supplementary Notes

Report uploaded and accessible at Tran-SET's website (http://transet.lsu.edu/).

16. Abstract

As one of critical components of a transportation infrastructure system, bridges are very important to a country's economy because they provide passage over physical obstacles to substantially reduce travel time and travel cost. Similar to other types of transportation infrastructure, bridges deteriorate over time. Therefore, bridges should be routinely inspected to ensure their serviceability, capacity, and safety under current traffic. Subsequently, transportation agencies at all levels (e.g., federal, state, local, and tribal) dedicate large amounts of time and money to routinely monitor and inspect bridge conditions as part of their infrastructure asset management programs. These transportation agencies use the collected data to make maintenance, repair, and construction decisions. As one important component of bridge inspection, bridge deck inspection ensures the serviceability and safety of everything above, on, and in bridge decks. Traditionally, bridge deck inspection is performed on the ground by having inspectors either visually inspect surface conditions or interpret the acoustic feedback from hammer sounding or chain dragging to determine subsurface conditions. These traditional methods have many limitations, including but not limited to, expensive, labor-intensive, time-consuming, can exhibit a high degree of variability, requiring specialized staff on a regular basis, and unsafe. Recent advancements in remote sensing, especially small-unmanned aircraft systems (S-UAS) based airborne imaging techniques and object based image analysis techniques, have shown promise in improving bridge deck inspection. This project explored the utility of S-UAS based airborne imaging techniques and object based image processing techniques in developing a complete data acquisition and analysis system to accurately and rapidly detect and assess bridge deck wearing surface and subsurface distresses at a low cost. This project developed a guidebook for the implementation of the proposed S-UAS based inspection system to assist transportation agencies with workforce development and professional training.

17. Key Words	18. Distribution Statement
Bridge Deck, Inspection, Small Unmanned Aircraft Systems, Airborne Imaging Techniques	No restrictions. This document is available through the National Technical Information Service, Springfield, VA 22161.

19. Security Classif. (of this report)	20. Security Classif. (of this page)	21. No. of Pages	22. Price
Unclassified	Unclassified	76	

Form DOT F 1700.7 (8-72) **Reproduction of completed page authorized.**

SI* (MODERN METRIC) CONVERSION FACTORS

APPROXIMATE CONVERSIONS TO SI UNITS

Symbol	When You Know	Multiply By	To Find	Symbol
		LENGTH		
in	inches	25.4	millimeters	mm
ft	feet	0.305	meters	m
yd	yards	0.914	meters	m
mi	miles	1.61	kilometers	km
		AREA		
in^2	square inches	645.2	square millimeters	mm^2
ft^2	square feet	0.093	square meters	m^2
yd^2	square yard	0.836	square meters	m^2
ac	acres	0.405	hectares	ha
mi^2	square miles	2.59	square kilometers	km^2
		VOLUME		
fl oz	fluid ounces	29.57	milliliters	mL
gal	gallons	3.785	liters	L
ft^3	cubic feet	0.028	cubic meters	m^3
yd^3	cubic yards	0.765	cubic meters	m^3
		NOTE: volumes greater than 1000 L shall be shown in m^3		
		MASS		
oz	ounces	28.35	grams	g
lb	pounds	0.454	kilograms	kg
T	short tons (2000 lb)	0.907	megagrams (or "metric ton")	Mg (or "t")
		TEMPERATURE (exact degrees)		
°F	Fahrenheit	5 (F-32)/9 or (F-32)/1.8	Celsius	°C
		ILLUMINATION		
fc	foot-candles	10.76	lux	lx
fl	foot-Lamberts	3.426	$candela/m^2$	cd/m^2
		FORCE and PRESSURE or STRESS		
lbf	poundforce	4.45	newtons	N
lbf/in^2	poundforce per square inch	6.89	kilopascals	kPa

APPROXIMATE CONVERSIONS FROM SI UNITS

Symbol	When You Know	Multiply By	To Find	Symbol
		LENGTH		
mm	millimeters	0.039	inches	in
m	meters	3.28	feet	ft
m	meters	1.09	yards	yd
km	kilometers	0.621	miles	mi
		AREA		
mm^2	square millimeters	0.0016	square inches	in^2
m	square meters	10.764	square feet	ft^2
m	square meters	1.195	square yards	yd^2
ha	hectares	2.47	acres	ac
km	square kilometers	0.386	square miles	mi^2
		VOLUME		
mL	milliliters	0.034	fluid ounces	fl oz
L	liters	0.264	gallons	gal
m	cubic meters	35.314	cubic feet	ft^3
m	cubic meters	1.307	cubic yards	yd^3
		MASS		
g	grams	0.035	ounces	oz
kg	kilograms	2.202	pounds	lb
Mg (or "t")	megagrams (or "metric ton")	1.103	short tons (2000 lb)	T
		TEMPERATURE (exact degrees)		
C	Celsius	1.8C+32	Fahrenheit	°F
		ILLUMINATION		
lx	lux	0.0929	foot-candles	fc
cd/m^2	$candela/m^2$	0.2919	foot-Lamberts	fl
		FORCE and PRESSURE or STRESS		
N	newtons	0.225	poundforce	lbf
kPa	kilopascals	0.145	poundforce per square inch	lbf/in^2

TABLE OF CONTENTS

LIST OF FIGURES

LIST OF TABLES

ACRONYMS, ABBREVIATIONS, AND SYMBOLS

AGL	Above Ground Level
CCEE	Civil, Construction, and Environmental Engineering
DEM	Digital Elevation Model
DSM	Digital Surface Model
EDAC	Earth Data Analysis Center
FRP	Fiber-Reinforced Polymer
GCP	Ground Control Point
GIS	Geographic Information Systems
GPR	Ground Penetration Radar
GSD	Ground Sampling Distance
IE	Impact Echo
IRT	Infrared Thermography
LiDAR	Light Detection and Ranging
MVS	Multi-View Stereo
NDE	Non-Destructive Testing
NMDOT	New Mexico Department of Transportation
OBIA	Object Base Image Analysis
RTK	Real-Time Kinematics
SfM	Structure-from-Motion
S-UAS	Small Unmanned Aircraft Systems
TIR	Thermal-Infrared
UNM	University of New Mexico
USDOT	U.S. Department of Transportation
USW	Ultrasonic Wave

EXECUTIVE SUMMARY

Bridges are critical transportation infrastructure assets because they provide passage over physical obstacles to substantially reduce travel time and travel cost. Similar to other types of transportation infrastructure, bridges deteriorate over time. Therefore, bridges should be consistently monitored and routinely inspected to ensure their serviceability, capacity, and safety under current traffic. In the United States, routine and in-depth bridge inspections are conducted by transportation infrastructure management agencies at all levels (e.g., federal, state, local, and tribal) to detect the signs of deterioration, identify the causes, and make decisions on the distribution of limited resources for maintenance, repair, rehabilitation, and construction projects.

The primary components of a bridge can be categorized into three classes, including bridge deck, superstructure (e.g., girders), and substructure (e.g., piers and abutments). Bridge decks should be evaluated and assessed on a more frequently schedule to address potential problems in a timely manner because degraded decks could severely reduce the serviceability of bridges, cause the deterioration of superstructures and substructures, and lead to structural failure. Bridge deck inspection ensures the serviceability and safety of everything above, on, and in bridge decks. Traditional bridge deck inspection is conducted on the ground by having inspectors either visually inspect surface conditions or interpret the acoustic feedback from hammer sounding or chain dragging method to determine subsurface conditions. These traditional methods are expensive, time-consuming, labor-intensive, unsafe, and requiring specialized staff on a regular basis. They can also exhibit a high degree of variability.

To overcome these challenges, researchers from the Earth Data Analysis Center (EDAC) and the Department of Civil, Construction, and Environmental Engineering (CCEE) at the University of New Mexico collaborated on this research to explore the utility of small-unmanned aircraft systems (S-UAS) based airborne imaging techniques in bridge deck surface and subsurface condition evaluation. The research team tested various S-UAS and selected DJI Mavic Pro 2 as the most effective one for collecting hyper-spatial resolution aerial images. The research team also tested various thermal-infrared (TIR) cameras and selected the most effective one for collecting TIR images. The research team also compared and selected Agisoft Metashape as the software application to conduct Structure-from-Motion (SfM) for the production of co-registered hyper-spatial resolution orthophoto and digital surface model (DSM). In addition, the research team used object based image analysis (OBIA) techniques, image enhancement techniques, image difference techniques, image fusion techniques, and principal component analysis (PCA) techniques to analyze the derived orthophotos and TIR images to detect and extract bridge deck surface (i.e., cracks) and subsurface (i.e., delamination) distress.

This research also developed a robust and powerful toolset that be used in standard geographic information systems (GIS) for operational implementation. This toolset can be used to detect, extract, and map bridge deck surface and subsurface distresses with an adequate degree of accuracy while maximizing the ability to assist inspectors with varying expertise. Research results revealed that the toolset is able to effectively detect and evaluate bridge deck surface and subsurface distresses at a high accuracy. This research also developed a guidebook on using the developed tools for professional education and training. The ultimate goal of this research is to train a new generation of transportation engineers that can effectively use the developed S-UAS based data collection and analysis system to accurately and rapidly detect, extract, and map bridge deck surface and surface distresses at a low cost.

1. INTRODUCTION

Bridges provide passage over physical obstacles to substantially reduce travel time and travel cost. They are one of the infrastructure components critical for the safety of traveling public and sustainability of economic activity *(1)*. Similar to other types of transportation infrastructure, bridges deteriorate over time due to various factors such as heavy traffic loads, aging of structures, and adverse weather conditions *(2)*. The most widely adopted method for bridge management is using bridge management systems (BMS) that often take into account stochastics progresses based on bridge inspection information *(3)*. Subsequently, transportation agencies at all levels (e.g., federal, state, local, and tribal) dedicate large amounts of time and funding to routinely inspect bridge conditions as part of their infrastructure asset management programs. The collected condition data are used by these agencies to make decisions on the distribution of limited resources for maintenance, repair, rehabilitation, and replacement projects.

The primary purpose of bridge inspection is to ensure public safety while the secondary purpose is to preserve the remaining service life of a bridge through early detection and rapid response to address deficiencies *(4)*. An effective bridge inspection program should be able to detect signs of deterioration, identify the causes, and recommend any needed maintenance or repair work to ensure the safety, serviceability, and structural capacity of a bridge under current traffic conditions *(5)*.

The Federal Highway Act in the U.S. established a mandatory national bridge inspection program in 1968, which was extended afterward to include all bridges that are managed by public entities *(6)*. In the U.S., five basic types of bridge inspection are normally performed, including initial, routine, in-depth, damage, and special, although the two common ones are routine inspection and in-depth inspection *(6-7)*. All bridge inspections need to be conducted in accordance with the National Bridge Inspection Standards (NBSI). An initial inspection is the first inspection that needs to be completed on a bridge when it is open for public use, and it is designed to establish baseline structural conditions and to identify and record any existing problems or potential problems in the structure. A routine inspection is generally performed every two years, and the purpose is to determine the functional conditions and serviceability of a bridge *(6)*. Routine visual inspection is the most common form of bridge inspection to satisfy the requirements of NBSI *(6, 8)*. An in-depth inspection normally performed every five years, and it is a close-up, boots on the ground inspection of all components (e.g., above and below water level) of a bridge to identify any potential deficiencies not readily detectable using routine inspection procedures *(6)*. A damage inspection is essentially an emergency inspection performed immediately following an accident or natural or human made disaster to determine whether structural damage has occurred. Lastly, a special inspection is designed to monitor known or suspected deficiencies on a regular basis (e.g., monthly).

In recent years, bridges have received a great amount of attention because of catastrophic failures, deteriorating conditions, and even political pressure *(5)*. According to the data obtained from the Bureau of Transportation Statistics, in 2017 there were more than 617,000 bridges in the U.S., and approximately 9.1% of them are rated as structurally deficient and 13.6% of them are rated as functionally obsolete because the average age of them was more than 40 years *(9)*. Therefore, high-risk bridges or bridges in poor condition may need to be inspected on a more frequent basis than the routine inspection.

The components of a bridge can be grouped into three classes (Figure 1), including deck (i.e., a deck on top of superstructure), superstructure (e.g., girders), and substructure (e.g., piers and abutments). Although all three components are equally critical to the performance of a bridge, this research focuses on bridge deck evaluation because the deterioration of bridge decks progresses more rapidly than any other bridge components *(10)*.

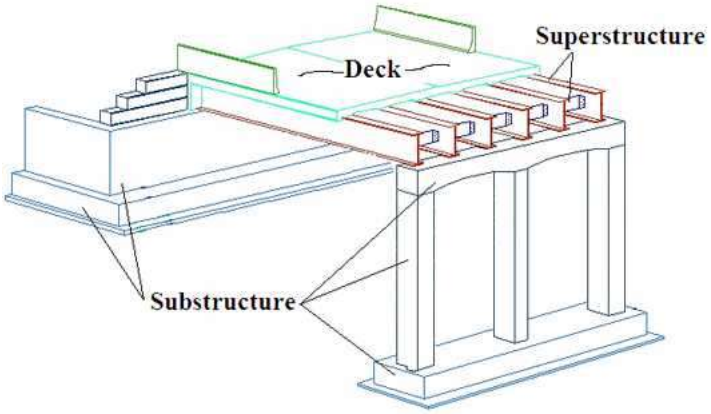

Figure 1. Components of a typical highway bridge (adopted from Michigan Department of Transportation).

Bridge decks can be constructed of concrete, steel, timber, and fiber-reinforced polymer (FRP). The primary function of bridge decks is to provide a safe and comfortable riding surface for traffic and distribute wheel loads to the superstructure. In addition, bridge decks protect the superstructure and substructure from environmental harm and various contaminants such as salts and chemicals *(5)*. Bridge decks are also vulnerable because they are subject to deterioration caused by various factors such as heavy traffic loads, adverse weather conditions, and chemicals (e.g., chloride). Therefore, to a certain extent, bridges can be considered as a sacrificial component because early bridge deck replacements must be done before the bridge superstructure needs to be replaced *(5, 10)*.

A degraded bridge deck could severely reduce a bridge's safety and serviceability. Additionally, a degraded bridge deck could cause the protection afforded to the superstructure and substructure diminish and could even cause the deterioration of these two components in an accelerating mode, ultimately leading to structural failure *(5, 11)*. Furthermore, evaluating bridge deck conditions has become increasingly critical as transportation agencies endeavor to optimize the timing and approaches for bridge preventative maintenance, repair, rehabilitation, and replacement. Therefore, bridge decks need to be evaluated and assessed on a more frequent schedule to identify and address potential problems in a timely manner. To characterize the conditions of a bridge deck, surveys are conducted to assess the following four elements: wearing surface, deck joints, guardrails, and structural deck *(12)*.

It is always a major challenge to conduct bridge deck evaluation because inspectors will be exposed to traffic and weather conditions *(5)*. Traditionally, bridge deck inspection is performed on the ground by having inspectors either visually inspect surface conditions or interpret the acoustic feedback from hammer sounding or chain dragging to determine subsurface conditions. These traditional methods have many limitations, including but not limited to, expensive, labor-intensive, time-consuming, can exhibit a high degree of variability, requiring specialized staff on a regular basis, and unsafe. Recent advancements in remote sensing, especially small-unmanned

aircraft systems (S-UAS) based airborne imaging techniques and object based image analysis (OBIA) techniques, have shown promise in improving bridge deck inspection. To leverage these emerging technologies to transform evaluation practices, this project explored the utility of S-UAS based airborne imaging techniques and object based image processing techniques in developing a complete data acquisition and analysis system to accurately and rapidly detect and assess bridge deck wearing surface distresses (i.e., cracking) and subsurface distresses (e.g., delamination) at a low cost.

2. OBJECTIVES

The main objective of this research is to develop a new approach to accurately and rapidly detect, extract, and map bridge deck wearing surface and subsurface distresses with S-UAS based airborne imaging techniques and transfer the technologies to transportation infrastructure management agencies at all levels (e.g., federal, state, local, and tribal) for implementation and workforce development. Specifically, this research project was focused on: (1) developing a S-UAS based bridge deck condition data acquisition and analysis system which can be used to accurately and rapidly detect bridge deck wearing surface distresses (i.e., cracks) and subsurface distresses (i.e., delamination) at a low cost; (2) developing a guidebook for the implementation of the S-UAS based bridge deck inspection system to assist transportation agencies with workforce development and professional training.

3. LITERATURE REVIEW

As one crucial component of bridge inspection, bridge deck inspection ensures the safety and serviceability of everything above, on, and underneath a bridge deck. The elements that need to be evaluated include, but not limited to, wearing surface, deck joints, guardrails, and structural deck elements such as concrete slabs *(12)*.

A wearing surface is a layer placed on the bridge deck to form a maintainable riding surface and protect the underlying deck from intrusion of water, salt, and chemicals. Wearing surfaces are typically constructed of timber, bituminous materials (asphalt), or concrete. As the roadway surface that in direct contact with vehicle traffic, general deteriorated condition of a wearing surface indicates possible reduced safety, serviceability, and capacity. Therefore, wearing surfaces need to be frequently inspected, and if a wearing surface shows significant deterioration such as cracking and spalling, it must be further evaluated for repair or replacement work.

Deck joints are designed to allow for traffic between structures while facilitating decks' transversal, longitudinal, and rotational movement. If the joints are substantially deteriorated, they must be further evaluated for repair or replacement work. Guardrails are designed to provide passive protection to vehicles, pedestrians, and bicyclists to keep them inside the road in a secure way. Guardrails must be evaluated for conformance to a transportation agency's policy to remain in place. Structural deck elements such as concrete slabs comprise the basic bridge deck plate. Structural deck elements are typically constructed of concrete, steel, timber, or FRP. If structural deck elements show substantial deterioration such as delamination, it must be further evaluated to estimate percentage of the total deck area that require full and partial deck slab repairs or even replacement.

As aforementioned, it is always a challenging work to evaluate bridge deck conditions *(13)*. To perform a bridge deck inspection, a team of inspectors, each of whom has different expertise, needs to visit the target bridge to identify defects and distresses on the deck and then measure their extent and severity. At the end, the inspectors need to prepare a report that includes ratings reflecting the condition of each bridge deck element *(6)*. The report typically includes textural descriptions of the extent and severity of the detected defects and distresses. Additionally, photos will be taken by inspectors on the ground and included in the report to document the observations *(6)*.

Currently, many methods are available for bridge deck inspection, and in general, they can be categorized as destructive method and non-destructive (NDE) evaluation methods *(6)*. Destructive evaluation methods involve obtaining core samples from a bridge deck to test their mechanical and chemical properties. Some examples of destructive evaluation methods include core control and chloride-ion concentration measurements *(11)*. NDE methods are useful for evaluating properties and characteristics of materials and systems without causing damage *(6)*. They are more commonly used for bridge deck inspection and they include, but not limit to, visual inspection, ground penetrating radar (GPR), impact echo (IE), ultrasonic wave (USW), chain dragging, infrared thermography (IR), and half-cell potential *(11)*.

Traditionally, bridge deck inspection is conducted on the ground by having inspectors either visually inspect surface conditions or interpret the acoustic feedback from hammer sounding or chain dragging to determine subsurface conditions. In recent years, in spite of the advancements of sensor-based NDE methods such as GPR and IR, they are still primarily deployed on the ground as visual inspection and chain dragging method, which can be considered as the "boots on the

ground" or ground-based methods. The major issues of the ground-based methods include, but not limited to, expensive, tedious, time-consuming, labor-intensive, require specialized staff on a regular basis, and potentially dangerous to inspectors in the hazardous traffic environments *(13-14)*. In addition, when performing ground-based visual inspection, the inspection process is subjective since the outcomes rely heavily on the experience of the inspectors and on the conditions under which the inspection process is completed, and thereby survey results can exhibit a high degree of variability, causing inconsistencies in surveyed data over space and across evaluation *(6, 15)*. When performing ground-based in-depth bridge deck inspection, another major challenge that inspectors encounter is the need to close the bridge to traffic, which can potentially cause severe traffic congestion and interruption *(13)*.

In a study to investigate the overall accuracy and reliability of visual routine and in-depth inspections, the Federal Highway Administration (FHWA) concluded that an in-depth visual inspection might not reveal deficiencies beyond those noted during a routine inspection *(6, 14)*. The study also concluded that there are many factors impact the effectiveness of visual inspection, including, but not limited to, the tools used, overall thoroughness with which inspectors completed the inspection, time to complete inspection, and the number of annual inspections completed *(6, 14)*. Therefore, deployment of technologies in bridge inspection and data collection can enhance efficiency, accuracy, and reliability of the bridge inspection process *(6)*.

In an effort to adopt technologies for bridge deck inspection, some researchers explored the utility of airborne observation in evaluating bridge deck wearing surface conditions. The method is also known as aircraft-based evaluation, which is typically accomplished with a manned aircraft and a natural color digital camera. The resulting natural color aerial images, which typically have ground-sampling distance (GSD) or spatial resolutions ranging from 7.62 cm (3-inch) to 15.24 cm (6-inch), can be used to evaluate bridge deck wearing surface distresses such as cracks. However, the GSD of these images limit their ability to detect and assess finer-scale wearing surface distresses such as individual cracks at sub-inch level *(16)*. Large-scale panchromatic aerial images (1:100) might be able to identify cracks on the wearing surface, but the extremely high cost ultimately prevent the further exploration of their applications for bridge deck wearing surface inspection. In addition, natural color aerial images cannot penetrate bridge deck to detect and assess subsurface defects such as delamination, although having information on both wearing surface and subsurface indicators of condition is vital in assigning a bridge deck rating *(13)*.

Therefore, it is necessary to explore and investigate technologies that are able to collect bridge deck wearing surface and subsurface condition data in an accurate, rapid, and cost-effective manner. Recent advancements in remote sensing technologies, including, but not limited to, S-UAS based hyper-spatial resolution airborne imaging and IR airborne imaging, SfM, and OBIA, have shown promise in inspecting bridge deck wearing surface and subsurface conditions.

S-UAS can fly lower to the ground than traditional manned aircraft, and therefore, allowing for collecting more detailed bridge deck condition data. In recent years, sUAS have emerged as an important platform for collecting of various types of hyper-spatial resolution aerial imagery to provide a synoptic view of the ground objects such as bridges. As an advanced photogrammetric method, SfM can be used to create the three-dimensional (3D) coordinates of objects by analyzing overlapping aerial images captured from varied perspective at approximately the spatial resolution of input images *(17-18)*. In addition, OBIA can be used to segment a raster image and then group individual pixels into vector objects based on spatial, spectral, and contextual information *(19)*.

OBIA is an ideal tool for finer infrastructure defects detection and assessment based on hyper-spatial resolution aerial images *(20)*. When coupled with hyper-spatial resolution aerial data and OBIA, SfM holds the potential to permit the estimation of horizontal and vertical measurement at sub-inch scales, and ultimately, the detection and assessment of bridge deck wearing surface distresses (e.g., cracks and spalling) at a finder scale. Bridge deck subsurface delamination interfere the heat transfer through the concrete and influence the amount of radiant energy emitted from the concrete surface *(21)*. Therefore, airborne IR imaging techniques can be used to detect and assess bridge deck subsurface distresses (i.e., delamination).

These technologies can be considered as a form of NDE method for bridge deck because they can be used to collect condition data without direct contact with the bridge deck being sensed *(22-23)*. More importantly, these technologies can collect bridge deck condition data above the ground, providing a synoptic view of the bridges being sensed, ultimately reducing the inspection cost. It should be noted that remote sensing is different from remote monitoring which typically has emplaced sensors such as strain gauges or accelerators that are indirect contact with the bridge components *(5)*.

Although there are many promising remote sensing technologies available for bridge deck wearing surface and subsurface condition assessment, to date there has been little evidence to prove that integrated results can be obtained from these technologies during a real field deployment *(13)*. The major challenge is to integrate these technologies to develop a complete data acquisition and analysis system to rapidly acquire, integrate, and analyze bridge deck wearing surface and subsurface data to determine their conditions.

Based on the review of literature, using S-UAS based airborne imaging techniques for bridge deck inspection is lacking and presents a significant gap in the research. Therefore, this research project is focused on integrating various S-UAS based airborne techniques and image processing techniques to develop a complete data acquisition and analysis system to detect bridge deck wearing surface and subsurface defects and distresses in an accurate, rapid, and cost-effective manner.

This research leverages various technologies including geographic information systems (GIS), S-UAS, hyper-spatial resolution natural color aerial imagery, SfM, OBIA, IR aerial imagery, and computer vision to develop a complete data acquisition and analysis system for bridge deck wearing surface and subsurface condition inspection. The proposed system uses an S-UAS as the flight platform, use two sensors (natural color and IR digital cameras) to collect hyper-spatial resolution aerial imagery, use the SfM technique to process the acquired aerial data to generate co-registered orthophotos and digital surface models (DSM) for bridge decks, and use pixel-based image processing, OBIA, and computer vision techniques to develop a few standard GIS (i.e., ArcGIS) compatible software tools for automated detection of bridge deck wearing surface and subsurface distresses. This is because the volume of the data delivered by the S-UAS based airborne imaging techniques necessities the development of an automated analytical workflow that indicates to a qualified bridge engineer or bridge inspector which distresses on the bridge deck wearing surface and subsurface warrant further engineering review.

4. METHODOLOGY

This research project was focused on developing a S-UAS based bridge deck condition data acquisition and analysis system which can be used to accurately and rapidly detect bridge deck wearing surface distresses (i.e., cracks) and subsurface distresses (i.e., delamination) at a low cost. Specifically, this research project's methodology includes: (1) S-UAS testing and data acquisition; (2) data processing; (3) analysis tool development; and (4) accuracy validation.

4.1. S-UAS Testing and Data Acquisition

4.1.1. S-UAS Testing

For S-UAS testing, the project team focused on testing and selecting the best S-UAS to develop an aerial data acquisition system for collecting bridge deck aerial images. It should be noted that an Unmanned Aerial Vehicle (UAV) is different from an UAS, although these two terms are often used interchangeably when referring to drones and aerial mapping. UAV indicates the actual aircraft platform that flies around to collected aerial data. In contrast, UAS indicates the entire system needed for aerial mapping, including UAV and sensors (e.g., natural color digital cameras). Therefore, a sensor or multiple sensors can be mounted to a UAV to create a UAS. According to the Federal Aviation Administration (FAA)'s Small Unmanned Aircraft Regulations (Part 107), an S-UAS is defined as an aircraft system that weighs more than 0.25 kg or 0.55 lbs. and less than 25 kg or 55 lbs. *(24)*. That being said, when testing the best S-UAS, it is necessary to make sure the combination of UAV and sensors are less than 25 kg. Based on previous experience and literature, the following S-UAS have been tested (Table 1 and Table 2).

Table 1. A list of tested S-UAS for collecting hyper-spatial resolution natural color (NC) aerial images.

S-UAS ID	Type	Description
NC1	Rotary	DJI Matrice 600 Pro UAV + Sony Alpha a6000 natural color digital camera (24.3-megapixel, sensor size 23.5 x 15.6 mm)
NC2	Rotary	DJI Matrice 210 V2 UAV + Sony Alpha a6000 natural color digital camera (24.3-megapixel, sensor size 23.5 x 15.6 mm)
NC3	Rotary	DJI Mavic Pro 2 UAV + onboard Hasselblad L1D-20c natural color digital camera (20-megapixel, sensor size 13.2 x 8.8 mm)
NC4	Rotary	DJI Phantom 4 Pro V2 UAV + onboard natural color digital camera (20-megapixel, sensor size 13.2 x 8.8 mm)
NC5	Rotary	DJI Mavic Air UAV + onboard 1/2.3-inch natural color digital camera (12-megapixle, sensor size 6.17 x 4.55 mm)
NC6	Rotary	DJI Mavic Air 2 UAV + onboard 1/2-inch natural color digital camera (12-megapixel, sensor size 6.4 x 4.8 mm)
NC7	Rotary	3DR Solo UAV + Canon SX260HS natural color digital camera (12.1-megapixel, sensor size 6.17 x 4.55 mm)
NC8	Rotary	3DR Iris+ UAV + Canon SX260HS natural color digital camera (12.1-megapixel, sensor size 6.17 x 4.55 mm)
NC9	Fixed-Wing	Event38 E384 UAV + Sony ILCE-QX1 natural color digital camera (20.1-megapixel, sensor size 23.2 x 15.4 mm)
NC10	Fixed-Wing	HCS XENO FX UAV + MAPIR Survey 3 natural color digital camera (12-megapixel, sensor size 6.25 x 4.69 mm)

Table 2. A list of tested S-UAS for collecting thermal-infrared aerial images.

S-UAS ID	Type	Description
TIR1	Rotary	DJI Mavic Pro UAV + customized FLIR Boson 320 thermal-infrared digital camera (pixel resolution 320 x 256)
TIR2	Rotary	DJI Mavic Pro Platinum UAV + customized FLIR Boson 320 thermal-infrared digital camera (pixel resolution 320 x 256)
TIR3	Rotary	DJI Mavic 2 Enterprise Zoom UAV + customized FLIR Boson 320 thermal-infrared digital camera (pixel resolution 320 x 256)
TIR4	Rotary	DJI Mavic 2 Enterprise Zoom UAV + customized FLIR Boson 640 thermal-infrared digital camera (pixel resolution 640 x 512)
TIR5	Rotary	DJI Mavic 2 Enterprise Dual UAV + onboard FLIR Lepton thermal-infrared digital camera (pixel resolution 160 x 120)

Based on the project team's previous experience and literature, the criteria for determining the best S-UAS for collecting hyper-spatial resolution natural color aerial imagery include: (1) operational simplicity (e.g., time and effort to get the system ready for aerial data collection); (2) flight time; (3) payload; (4) aerial imagery quality; and (5) cost. Each of the criteria was scored on a scale of 1 to 5 (1 = Very Poor, 2 = Poor, 3 = Fair, 4 = Good, and 5 = Very Good). The total score for a perfect option will be 25, and a passing grade needs to be 15 (60%). Table 3 lists the ratings for each tested S-UAS and the best option for collecting hyper-spatial resolution natural color aerial imagery for bridge deck wearing surface inspection is using the DJI Mavic Pro 2 UAV and the onboard Hasselblad L1D-20c NC digital camera. It has the highest score of 23 (Figure 2).

Based on the project team's previous experience and literature, the criteria for determining the best S-UAS for collecting thermal-infrared aerial imagery include: (1) operational simplicity (i.e., time and effort to get the system ready for aerial data collection); (2) flight time; (3) aerial imagery quality; (4) pixel resolution; and (5) cost. Each of the criteria was scored on a scale of 1 to 5 (1 = Very Poor, 2 = Poor, 3 = Fair, 4 = Good, and 5 = Very Good). The total score for a perfect option will be 25, and a passing grade needs to be 15 (60%). Table 4 lists the ratings for each tested S-UAS and none of them received a passing grade. Therefore, the project team did not select any of the tested S-UAS for collecting thermal-infrared aerial images.

Table 3. A list of scores for the tested S-UAS for collecting hyper-spatial resolution natural color (NC) aerial images.

S-UAS ID	Operational Simplicity	Flight Time	Payload Capacity	Imagery Quality	Cost	Total Score
NC1	3	40-min (4)	6.0kg (5)	4	~$12,000 (2)	18
NC2	3	27-min (3)	1.5kg (4)	4	~$10,000 (2)	16
NC3	5	31-min (4)	1.1kg (4)	5	~$1,800 (5)	23
NC4	5	30-min (4)	1.0kg (4)	5	~$2,500 (4)	22
NC5	5	21-min (2)	0.3kg (2)	3	~$1,000 (5)	17
NC6	5	34-min (4)	0.8kg (3)	4	~$1,000 (5)	21
NC7	4	25-min (3)	0.7kg (3)	4	~$1,500 (5)	19
NC8	4	22-min (2)	0.4kg (2)	4	~$1,000 (5)	17
NC9	3	90-min (5)	1.0kg (4)	5	~$8,000 (3)	20
NC10	3	60-min (5)	1.0kg (4)	4	~$8,000 (3)	19

Figure 2. DJI Mavic Pro 2 UAV and onboard Hasselblad L1D-20c natural color digital camera.

Table 4. A list of scores for the tested S-UAS for collecting thermal-infrared aerial images.

S-UAS ID	Operational Simplicity	Flight Time	Imagery Quality	Pixel Resolution	Cost	Total Score
TIR1	1	27-min (3)	1	320 x 256 (2)	~$5,000 (4)	11
TIR2	1	27-min (3)	1	320 x 256 (2)	~$5,000 (4)	11
TIR3	1	31-min (4)	1	320 x 256 (2)	~$6,000 (4)	12
TIR4	1	31-min (4)	1	640 x 512 (3)	~$8,000 (3)	12
TIR5	2	31-min (4)	1	160 x 120 (1)	~$4,000 (4)	12

As shown in Table 4, none of the tested S-UAS is able to collect aerial photos that have high enough spatial resolution to be able to detect bridge deck subsurface distresses such as delamination. When conducting operational evaluation, an S-UAS has to fly at an altitude that is safe to avoid drone collision and driver distraction. There is no official guidance on how to select a safe flight height, because it depends on many onsite environmental factors such as the height of overhead power lines, height of buildings, and height of trees, and the anticipated spatial resolution of the collected aerial images. In general, for aerial mapping purpose, it is suggested to fly the S-UAS at lower as possible, as permitted by the surrounding structures and trees, to acquire hyper-spatial resolution aerial images. According to the American Society for Testing and Materials (ASTM), when collecting thermal-infrared images for evaluating bridge deck delamination, the image quality and utility is highly dependent on the camera field of view (FOV) and lens *(25)*. They suggest that the ideal option for image collection is one single image can cover one entire lane that typically has a width of 3 to 3.65 m *(25)*.

However, a previous study revealed that obtaining a horizontal field view of 3 to 3.65 m is not always achievable in the field *(13)*. They discovered that order to collect effective thermal images for bridge deck subsurface distress evaluation, a thermal camera (FLIR SC640) with a very high

pixel resolution (640 x 480) should be placed at a height 1.88 m (6.2-feet) from the ground *(13)*. This is because the pixel count for thermal cameras is very low, which leads to very low spatial-resolution images that cannot be used to effectively resolve delamination distress. After testing, it revealed that none of the tested S-UAS and other potential S-UAS could fly at this height safely, because in general they have to fly at a minimum height 10 m (33-feet) from the ground to avoid collision with obstacles. Subsequently, the project team did not suggest use any of the currently available S-UAS to collect thermal-infrared aerial imagery for bridge deck subsurface distress (i.e., delamination) evaluation.

Because of the impracticality, instead of using an S-UAS to collect thermal-infrared aerial imagery for detecting bridge deck delamination, the research team decided to use a handheld compact thermal-infrared camera (FLIR C5) for data collection. This camera is manufactured by FLIR Systems, which is a leading company in thermography. FLIR C5 is also known as the pocket thermal-infrared camera (Figure 3). It can fit in a bridge inspector's pocket and it is a go-to toll for infrastructure inspection, facility maintenance, and other troubleshooting applications. This camera has a 160 x 120-pixel resolution thermal-infrared camera (6.5 to 14 µm). It also has a 5-megapixel natural color digital camera that can be used to collect natural color images that can be co-registered with the thermal-infrared images. This dual camera configuration enables a multi-spectral dynamic imaging (MSX) technology to add visible light details to thermal-infrared images in real time for greater clarity, feature edge sharpening, and enhance outline detail. This feature makes this camera very suitable for detecting bridge deck delamination because it adds context to thermal-infrared images and makes it easier to understand what the inspectors are observing. It should be noted that a thermal image without reference details might cause confusion later.

Figure 3. FLIR C5 compact thermal-infrared camera (adopted from FLIR Systems).

4.1.2. Data Acquisition

After the S-UAS and thermal camera had been selected for collecting natural color aerial photos and thermal images, the research team selected ten bridges that could potentially be used for data collection based on their location and surrounding environment (limited amount of power lines or trees). With regard to location, there are three aspects to consider: (1) bridges have to be at least five nautical miles or 9.3 km away from an airport; (2) bridges are not located on arterial roads or interstate highways to avoid high traffic volumes; (3) bridges are not located in densely populated neighborhoods or open areas that have a large number of pedestrians. Regarding surrounding environment, there are two aspects to consider: (1) there are no or limited amount of power lines around the bridges; and (2) there are no or limited number of trees around the bridges. Figure 4 shows the airports and their five nautical miles (9.3 km) buffer.

It should be noted that all selected bridges are located in Bernalillo County. The research team also considered other bridges in New Mexico such as bridges that are located in Chavez County, Lea County, or Eddy County. However, they were not selected for data collection due to undesired long-distance traveling. Figure 5 shows the location of the selected bridges that are located in Bernalillo County. As it reveals in Figure 5, ten bridges that could potentially be used for data collection were selected and they are located in the north and east of the Bernalillo County. The research team obtained the information about these bridges from NMDOT and summarized them in Table 5.

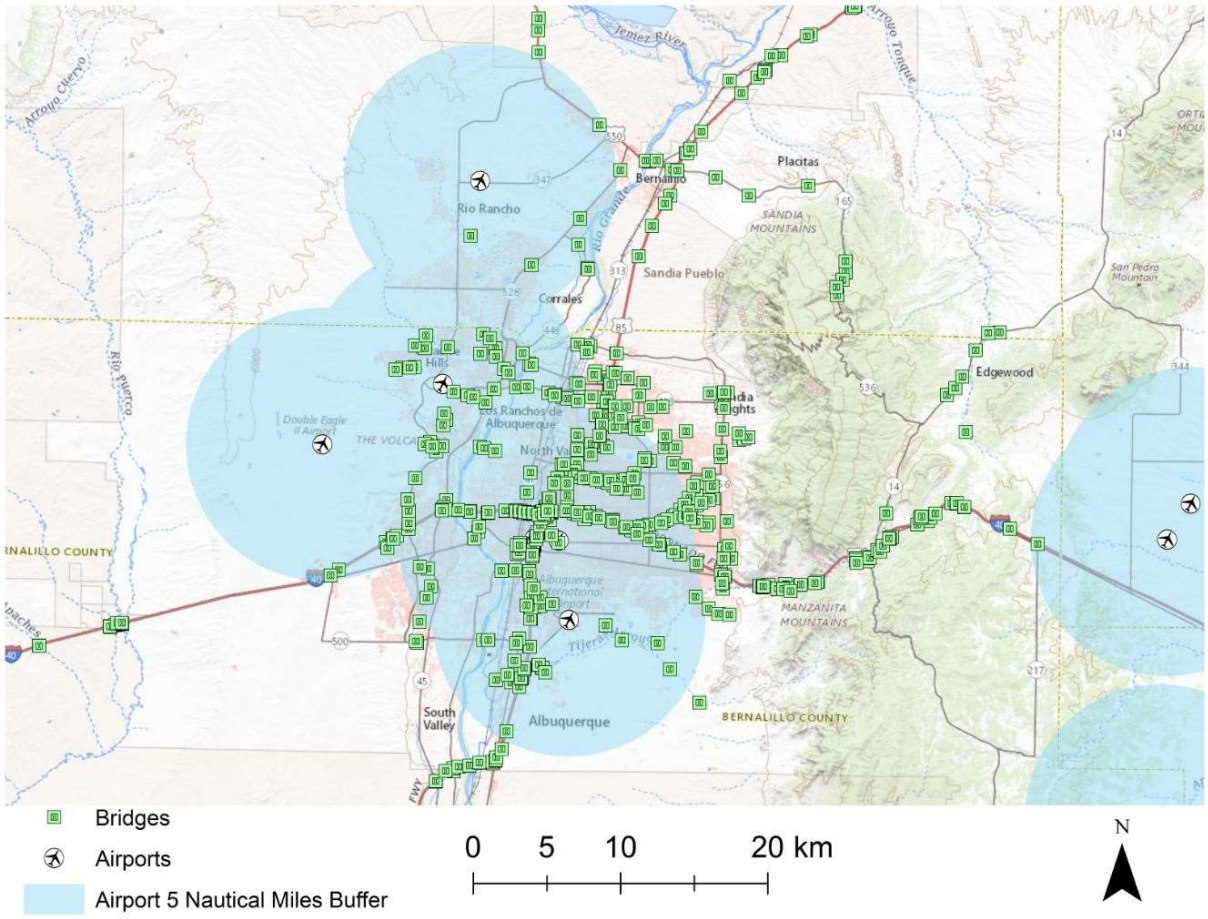

Figure 4. A demonstration of using airport buffer to filter bridges that are potentially suitable for data collection.

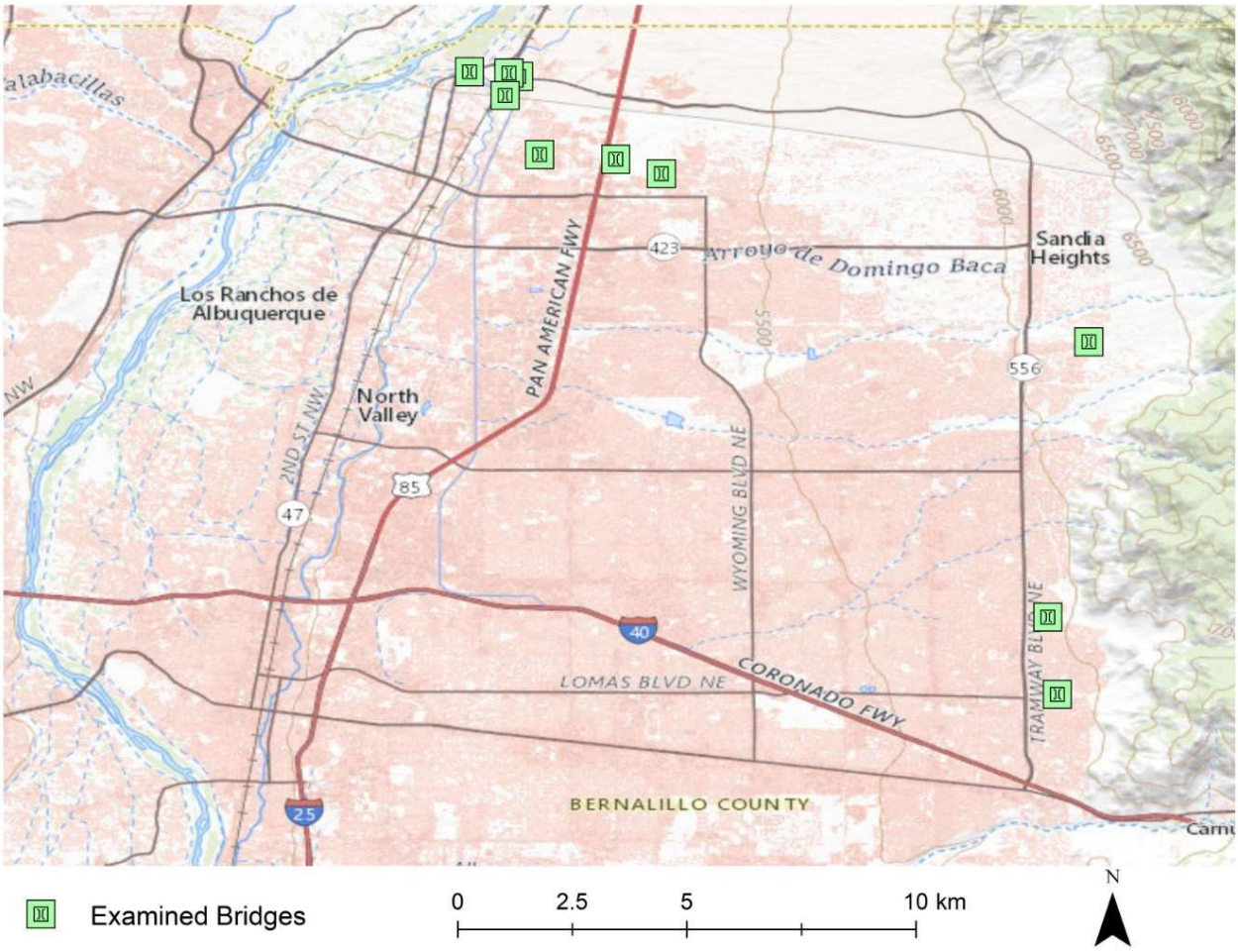

Figure 5. The location of the selected bridges for examination.

Table 5 presents detailed information about these examined bridges. According the FAA Part 107 rule, remote pilots cannot fly S-UAS over moving vehicles unless they have obtained waivers from FAA. In addition, remote pilots cannot operate S-UAS directly over another person unless that person is directly involved in the operation or within a safe cover such as a stationary vehicle or protective structure. Therefore, the research team further examined each bridge's annual average daily traffic (AADT, data collected in 2013 by NMDOT) to see if a low traffic volume can be observed for any of the bridges because the research team wanted to ensure no moving vehicles during data collection. Additionally, the research team needs collect ground control points (GCP) for aerial image processing (discussed in data processing section), and a low traffic volume bridge can ensure safety during CGP data collection on the ground. The research team also visited these bridges to inspect the wearing surfaces to see if any distresses can be visually observed. This is because it is not practical to collect data for image analysis or tool development if no distresses being observed. In other words, image analysis and tool development are depending on sample distresses and a wearing surface that does not any distresses cannot be used for distress detection and evaluation. A bridge will be considered as the best one for data collection if it has low traffic volume and at the same time has many visible distresses. Based on these criteria, the bridge with ID number of 358620 was selected for data collection.

Table 5. A list of examined bridges for data collection.

ID	Year Built	Deck Width	Length	AADT	Comments
355703	1955	9.8 m	30.5 m	6,647	High traffic volume, no visible distresses
355704	1955	9.8 m	39.3 m	6,647	High traffic volume, no visible distresses
356651	1966	20.2 m	169.2 m	8,883	High traffic volume, no visible distresses
358331	1980	16.5 m	7.3 m	936	Low traffic volume, no visible distresses
358620	1967	10.2 m	23.5 m	1,051	Low traffic volume, many visible distresses
358662	1986	30.2 m	14.0 m	633	Low traffic volume, no visible distresses
358796	1989	17.9 m	7.9 m	1,670	Low traffic volume, no visible distresses
359296	2003	18.3 m	10.3 m	3,666	Medium traffic volume, few visible distresses
359297	2003	29.9 m	13.1 m	12,129	High traffic volume, no visible distresses
359319	2003	11.3 m	21.3 m	875	Low traffic volume, no visible distresses

Bridge 358620 is located at the intersection of Edith Blvd and the North Division Channel (Figure 6). For geographic reference purpose, it is located 2.25 km (1.4 miles) north of Alameda Blvd. This bridge was built in 1967, and its end of functional service life (EFSL) is 2033. The material for the bridge is pre-stressed concrete. The material for the wearing surface is asphalt concrete. The road width is 8.5 m (2 lanes), and there is no parallel bridge to it. According to the last inspection conducted in 2019, the deck condition is satisfactory. However, the wearing surface has many distresses such as cracks and bleeding. Additionally, superstructure condition is good while the substructure condition is fair.

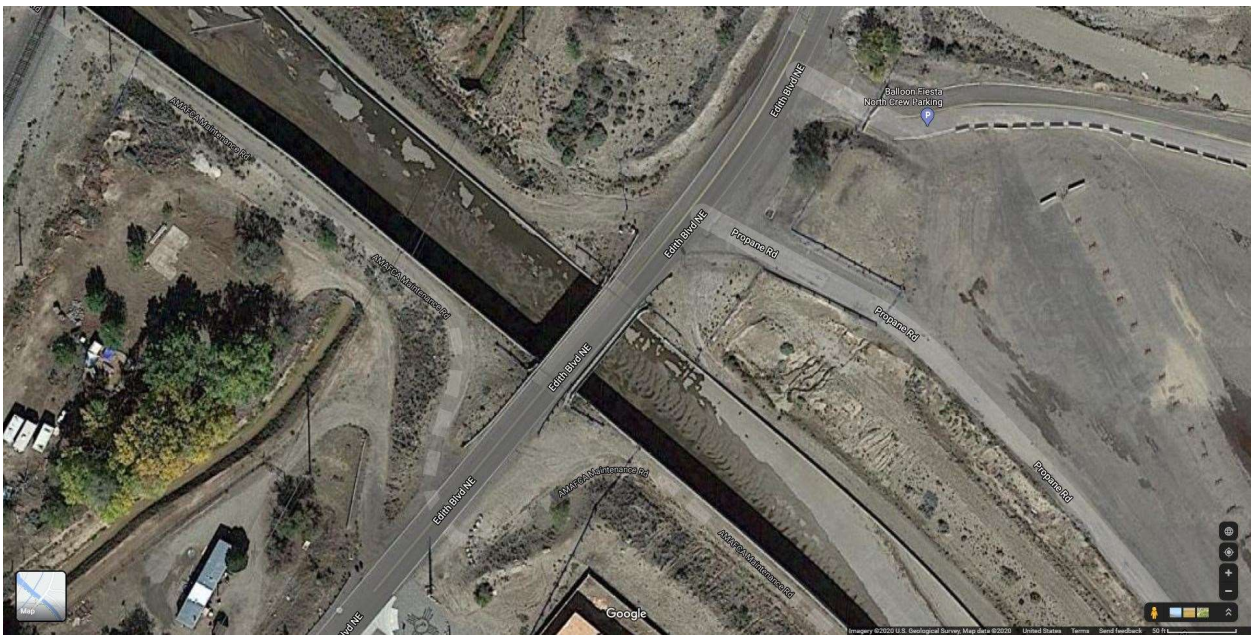

Figure 6. Google Maps Satellite view of Bridge 358620.

Once the bridge was selected for data collection, the project team visited the bridge 12 times to fly the selected S-UAS to develop best practices for field data collection. The project team visited the bridge on a bi-weekly basis from January to June 2020. The project team successfully developed best practices for using the selected S-UAS to collect natural color aerial photos.

During the field test, the project team also explored the utility of the thermal-infrared camera in collecting thermal-infrared images. Unfortunately, the project team did not successfully find any delamination in the bridge deck with the Flir C5 thermal-infrared camera. Mr. George Baca, who is NMDOT's contractor to perform bridge inspection across the State of New Mexico, also confirmed that Bridge 358620 does not have any delamination issues. The project team wanted to collect data in the same field to avoid multiple trips and save time. With the help of Mr. George Baca, the project team identified and located a concrete retaining wall that has delamination issues. The concrete retaining wall is close to a railroad bridge, which is approximately 150 meters away from Bridge 358620 (Figure 7). The project team was not able to find any information regarding the railroad bridge.

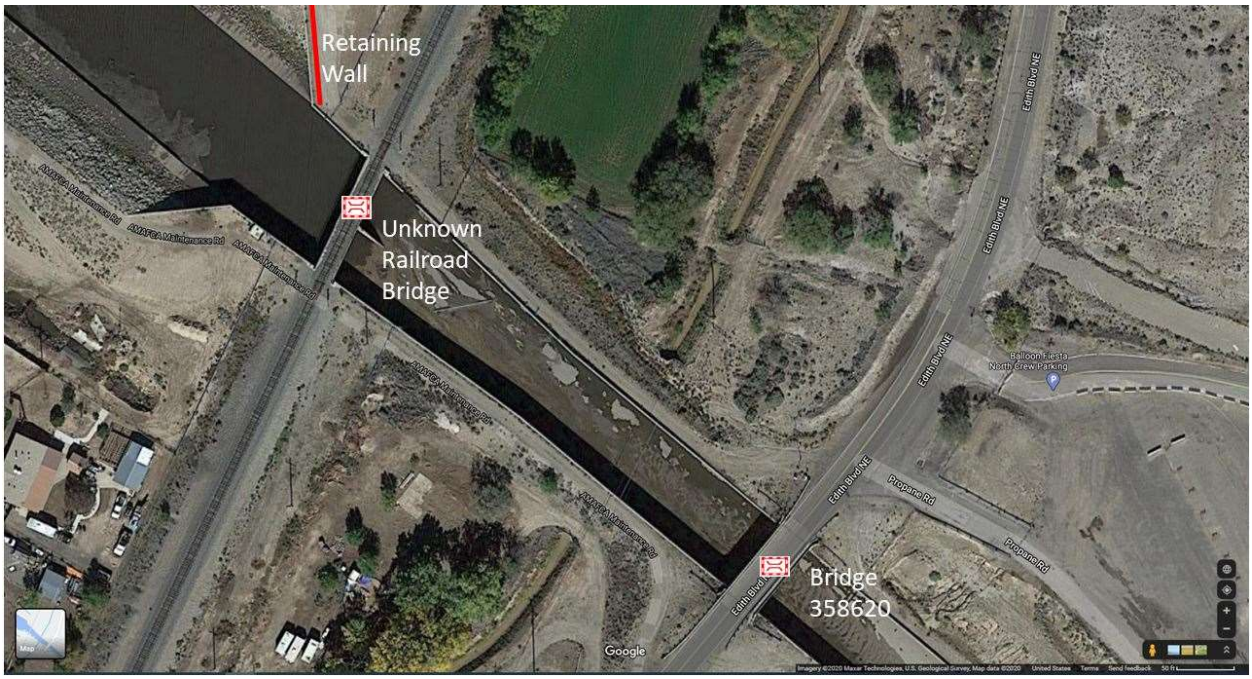

Figure 7. The retaining wall with delamination issues near Bridge 358620.

For natural color aerial imagery collection, the project team visited Bridge 358620 on August 14, 2020 from 10:00 am to noon. The date was also coordinated with Mr. George Baca to conduct ground survey (visual inspection and tape measurement) of the wearing surface distresses. The ground survey was focused on the count, length, and width of the cracks in the wearing surface. The ground survey results were used in the Analysis and Findings Section.

A mobile application referred to as Map Pilot for DJI developed by Drones Made Easy was used for flight planning. Users can use it to create and fly their own optimal flight paths to collect geotagged (longitude, latitude, and ellipsoidal height) aerial photos that are in highly overlapping patterns. According to Zhang et al. *(18)*, SfM requires a high degree of overlap (75% for sidelap and 80% for forward overlap). To ensure sufficient overlap, this study used a grid flight path instead of a normal flight path (Figure 8). There are power lines on the west side of bridge, and the height of the power lines are approximately 20 meters. Therefore, the project team decided to fly the S-UAS at an altitude of 23 meters above the ground level (AGL) to avoid collision with power lines and at the same time to obtain natural color aerial images with acceptable spatial resolution (5 mm) to identify cracks on the wearing surface.

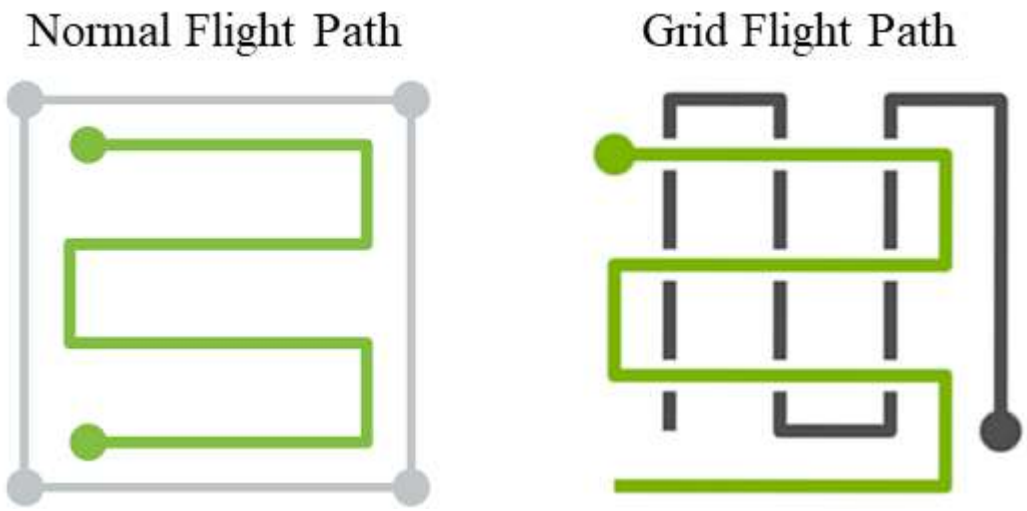

Figure 8. An Illustration of the normal flight path and grid flight path (adopted from Pix4D).

Figure 9 shows the graphic user interface (GUI) of the Map Pilot for DJI mobile application. The purple solid dot indicates the take-off and landing point for the S-UAS. The orange dots indicate the corner points of the bounding box of the flight path. The small green and red dots indicate the start point and end point of the flight path, respectively. The bridge was completely covered the flight path. The flight path also covered the immediate surroundings of the bridge to ensure the positional accuracy of the rapid depth change of the bridge structure. According to Hughes et al. *(26)*, a 10 to 25 meters buffer should be applied to the study to minimize depth errors of DSMs. Their investigations revealed that DSM depth errors are greatest on steeper slopes. A bridge deck is similar to a flat ground, while the edge of the bridge structure is similar to a cliff.

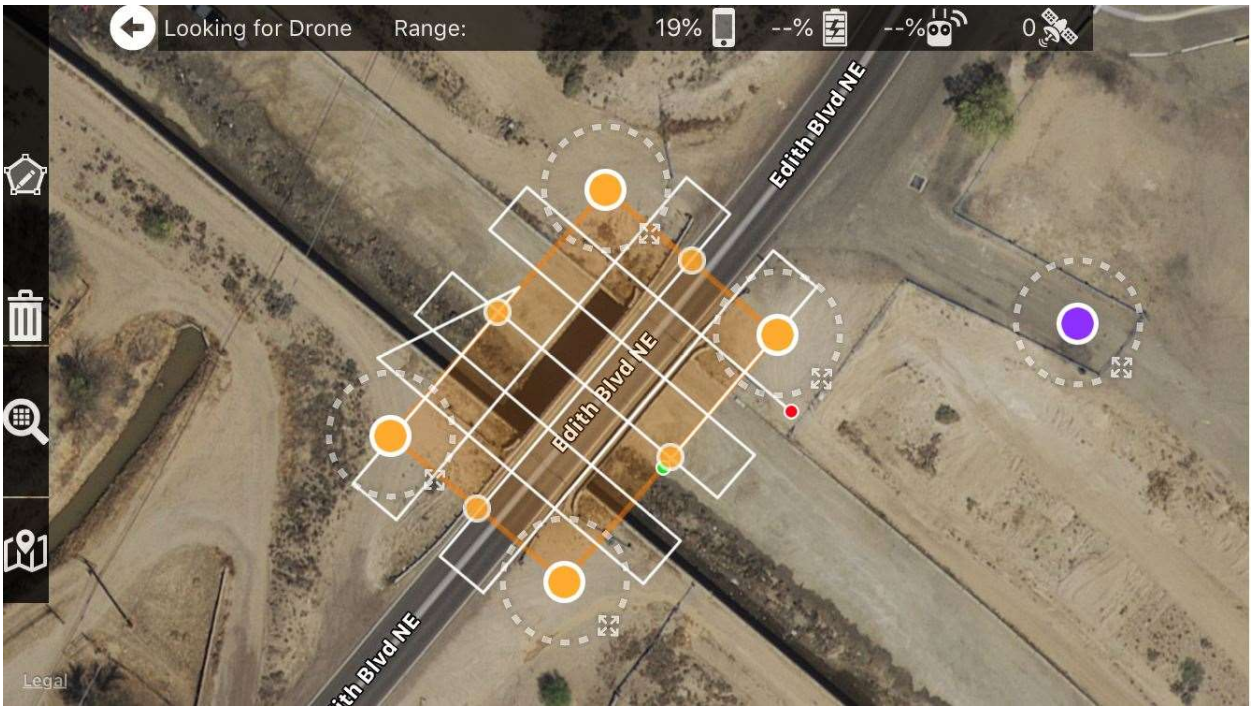

Figure 9. An Illustration of the flight path for natural color aerial imagery collection.

With a grid flight path, a total of 92 geotagged aerial photos in JPEG format were collected. The entire flight duration is 5 minutes and 30 seconds, and the total data volume is 0.75GB. The flight altitude is 23 meters AGL, which results in a spatial resolution of 0.5 cm or 5 mm. The forward overlap is 80% and the sidelap is 75%. Figure 10 and Figure 11 show the flight plan specifications.

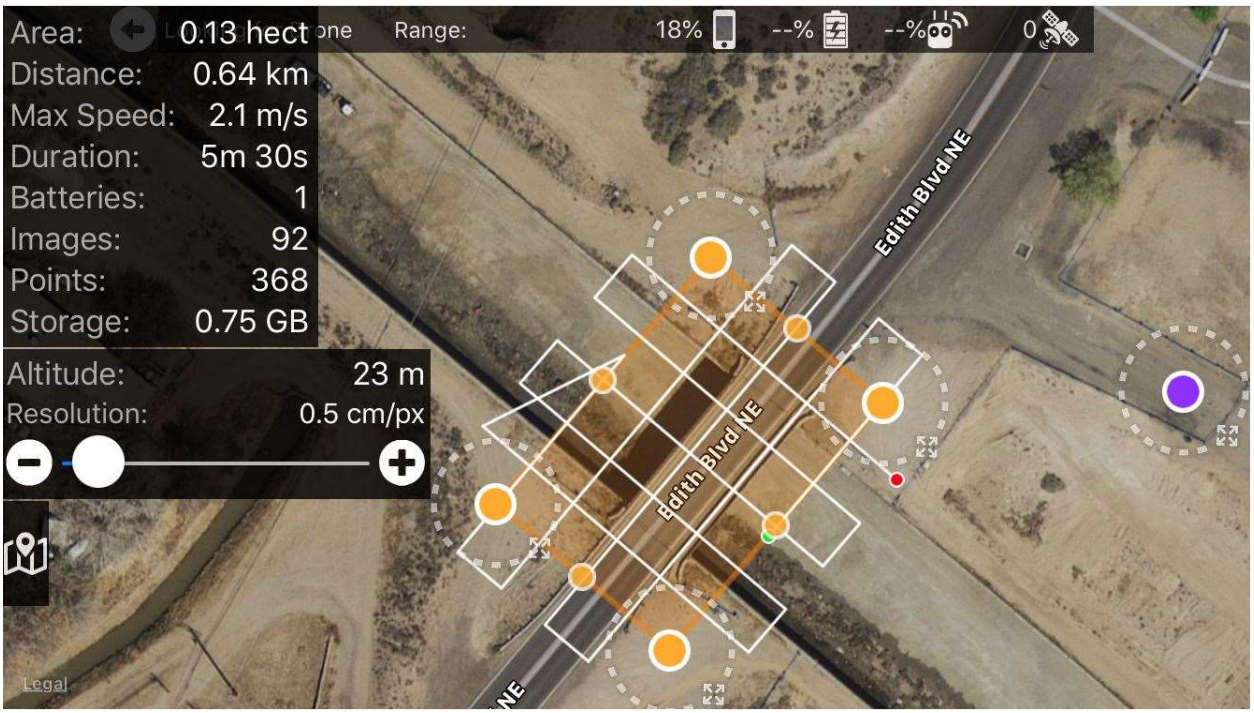

Figure 10. The duration, photo quantify, photo size, and altitude of the designed flight path.

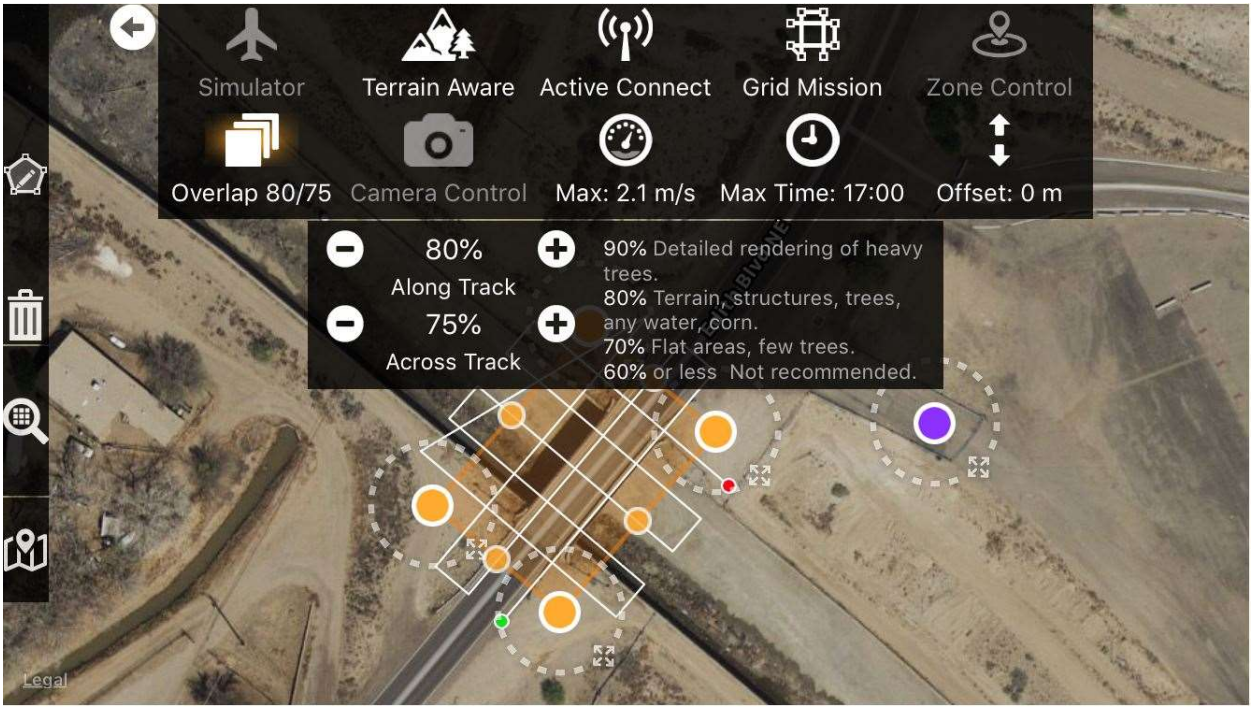

Figure 11. The forward overlap and sidelap of the designed flight path.

Figure 12 shows an example of the collected natural color aerial photos (5,472 x 3,648 pixels). The spatial resolution of these photos is 0.5 cm (5 mm). The cracks on the wearing surface can be easily identified. The asphalt crack sealing can also be identified. During data collection, the sky was overcast, and therefore, there are no shadows in the photos. It should be noted that none of these aerial images cover the entire bridge due to hyper-spatial resolution imagery acquisition. The higher the spatial resolution, the more detail it will contain, and the smaller ground coverage it will contain. Figure 13 shows the location of exposure stations of all 92 aerial photos.

Figure 12. An example of the natural color aerial imagery collection.

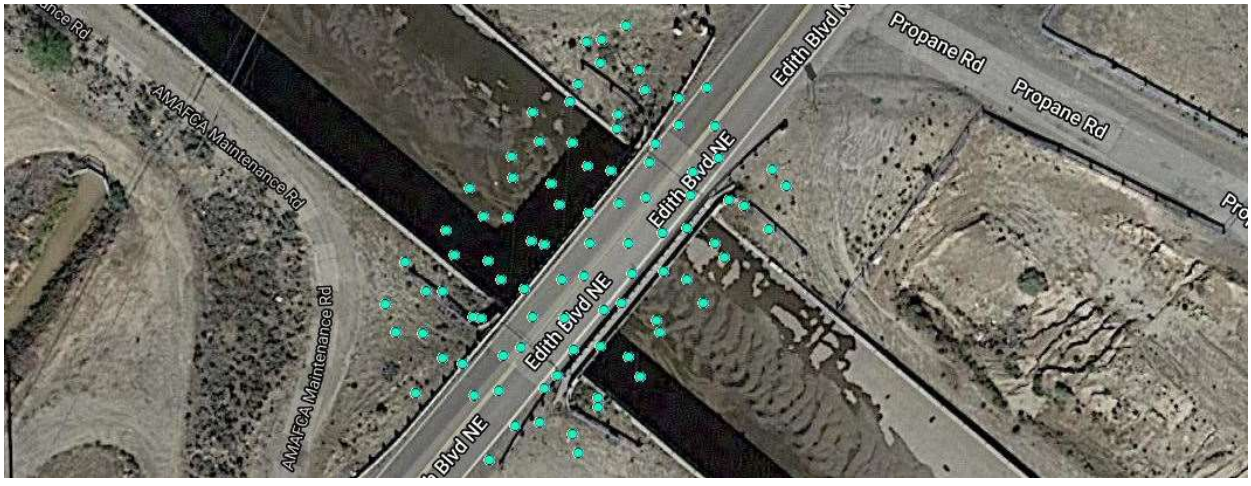

Figure 13. The exposure stations of all 92 aerial photos.

After aerial photo collection, the project team also collected ground control points (GCP) for image processing in SfM. GCPs are points on the ground surface with known coordinates (longitude, latitude, and altitude). They are commonly used in the SfM process to orientate and calibrate the output point cloud to ensure a high degree of global positional accuracy. Detailed information regarding GCPs will be discussed in the next section.

The project team collected 10 GCPs (Figure 14 and Figure 15). As a rule of thumb, SfM requires a minimum of three GCPs for image processing, and no more than 10 are usually needed. These 10 GCPs are noticeable objects on the wearing surface, including sharp edges of cracking, intersections of cracking, and asphalt stains. These GCPs are evenly distributed across the bridge deck, and they are not obstructed by visual obstacles such as shadows or glares. Another rule of thumb is that if the study area being mapped has noticeable elevation changes like hills and valleys, at least one GCP should be placed on each of the major elevation terrains. The 10 GCPs are all located on the bridge deck because there are no noticeable elevation changes across the bridge.

The coordinates of the GCPs were collected using a Real-Time Kinematics (RTK) system in a rover/based configuration. RTK is used to enhance the precision of positional data obtained from Global Navigation Satellite System (GNSS), which is the combination of existing satellite navigation systems such as GPS, GLONASS, Galileo, and Beidou. RTK uses not only the satellite signal's information content but also the measurements of the phase of the signal's carrier wave, and it is characterized by using a moving device referred to as the rover and a single reference station referred to as the base to provide real-time corrections, delivering up to mm-level accuracy.

The project team has access to a few RTK systems. These systems include a Trimble R10, an Emlid Reach RS, and an Emlid Reach RS2. The project team used the Emlid Reach RS2 system to collect the coordinates of the GCPs because of its simplicity, low cost, and high accuracy.

Figure 14. The locations of the collected GCPs.

Figure 15. A zoomed-in example of the collected GCPs.

The coordinates of the collected GCPs are presented in longitude, latitude, and altitude (ellipsoidal height) formats. The GCPs were post-processed with the software of EZSurv developed by Effigis (Figure 16). This software uses the National Oceanic and Atmospheric Administration (NOAA) Online Positioning User Service (OPUS) to post-process the surveyed coordinates and the ultimate root mean square error (RMSE) was 0.003m + 1 ppm horizontally and 0.006m + 1 ppm vertically. Considering the spatial resolution of the aerial photos is 0.005 m, the accuracy of the GCP is able to process the aerial photos in SfM effectively. A previous research conducted by the project team revealed that when the accuracy of the GCPs are close to the spatial resolution of the aerial photos, the orthophotos and DSMs created by SfM has similar horizontal accuracy and vertical accuracy to the GCPs *(15)*.

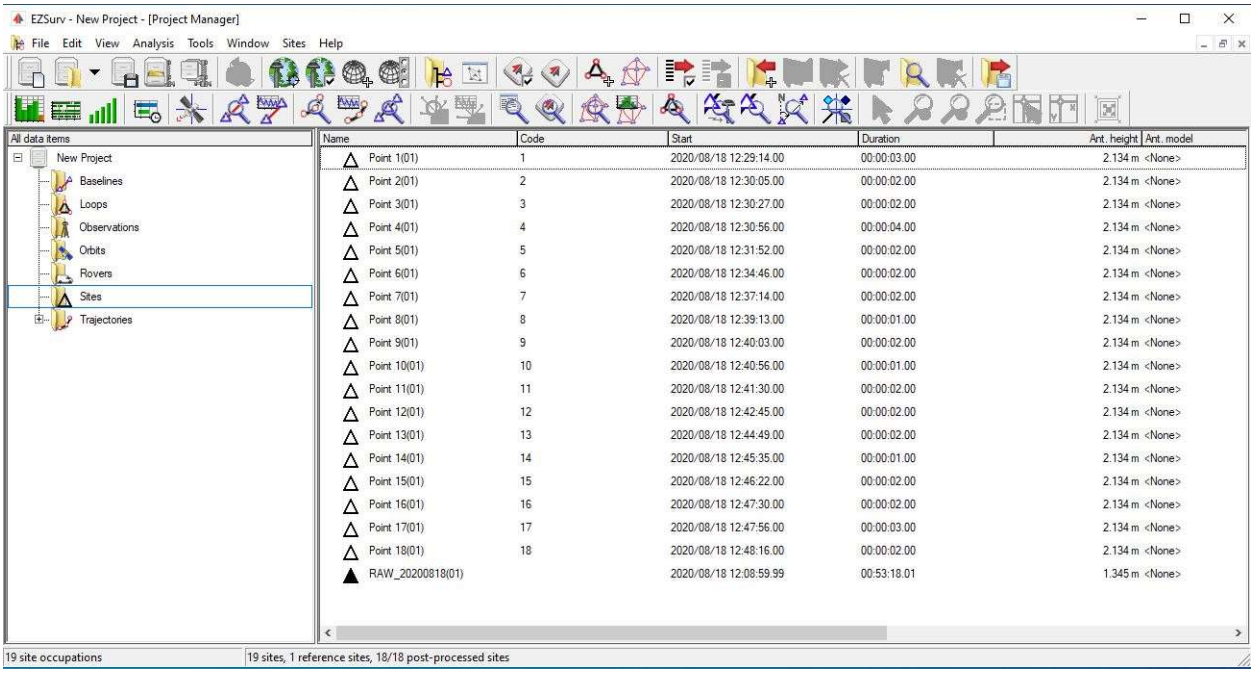

Figure 16. The user interface of the EZSurv software.

Flir C5 was used for thermal infrared imagery collection. The use of a thermal infrared camera for imagery collection is referred to as passive infrared thermography because the energy from sunlight or ambient temperature change are the main heating source for this application *(13)*. Thermal infrared cameras can capture the radiant temperature of an object's surface and then convert the temperature measurement into a pseudocolor image in which the brighter colors (e.g., red, orange, and yellow) indicate warmer temperatures while darker (e.g., blue, purple, and black) indicate cooler temperatures. In addition, the actual temperature (true kinematic temperature) of an object reported on the Flir C5 camera are automatically corrected based on the object's emissivity, which is a measure of the object's ability to emit infrared energy. It is the ratio of the energy radiated by an object at a given temperature to the energy emitted by a blackbody (perfect radiator), and its value ranges from 0 to 1, with 0 being as a perfect reflector and 1 being as a perfect emitter. An object emissivity is influenced by many factors, including but not limited to, surface roughness, angle of view, field of view, object moisture, and color. The emissivity of concrete is approximately 0.95 *(13)*.

The concept behind the use of a thermal infrared camera in delamination evaluation is that the anomalies and subsurface delamination in concrete will interrupt the heat transfer, and ultimately, influence the amount of radiant energy emitted from the concrete surface *(13)*. As the ambient temperature rises during the day, concrete will absorb heat and at the same time emit radiant energy. However, delamination and air voids in concrete will resist heat transfer, which make them warm up at a faster rate than the surrounding concrete that is in good shape. Subsequently, delamination appears warmer on thermal infrared images. On the contrary, as the ambient temperature decreases during evening time, delamination and air voids in concrete will lose heat at a faster rate than the surrounding good concrete, and subsequently, delamination appears coolers on thermal infrared images *(13, 27)*.

For thermal infrared thermography, time of data collection is the most critical factor to consider. This is because different materials in the outdoor environment respond differently to ambient temperature change, which ultimately influence their radiant energy emission processes throughout the day. Two crossover times have been identified as threshold times, including local sunrise and sunset time, because at these two times radiant temperatures of all materials are the same *(13)*. A study revealed that the effective time to conduct thermal imaging tasks depends on the depth of concrete delamination: on the thermal infrared images, the most contrast appears on four hours after sunrise for a 5.1 cm (2-inch) deep delamination and 7 hours after sunrise for a 7.6 cm (3-inch) deep delamination *(27)*. Additionally, the study revealed that thermal infrared imaging techniques are not possible to detect any delamination that is deeper than 7.6 cm *(27)*.

It should be noted that other factors such as moisture, asphalt stains, oil spills, and even environmental factors also affect the thermal infrared imaging results – a hot or cold spot on a thermal infrared image does not always attribute to delamination *(28)*. A few studies have been focused on exploring the ideal condition for using thermal infrared imaging techniques for detecting concrete delamination, but it is not operationally practical to achieve these ideal conditions for most field missions *(13)*.

For this project, the data collection for thermal infrared images has been discussed at the beginning of this section. The project team collected data on August 18, 2020 and the sunrise time for that day was 6:29 am. The best time for data collection was 10:30 am and the actual data collection time was 11:10 am. The humidity of data collection time was 26%. The high temperature of that

day was 33°C (92°F) and the low temperature was 20°C (68°F). The project team collected thermal infrared images for 10 locations but only one location has delamination issues, and the depth of the delamination is approximately 5.1 cm (2-inch). A natural color photo (5-megapixle) that is co-registered to the thermal image was also taken by the Flir C5 camera (Figure 17). The unit of the temperature in Figure 17 (a) is degree Celsius. It should be noted that these photos are not geotagged because the Flir C5 does not have built-in GPS unit.

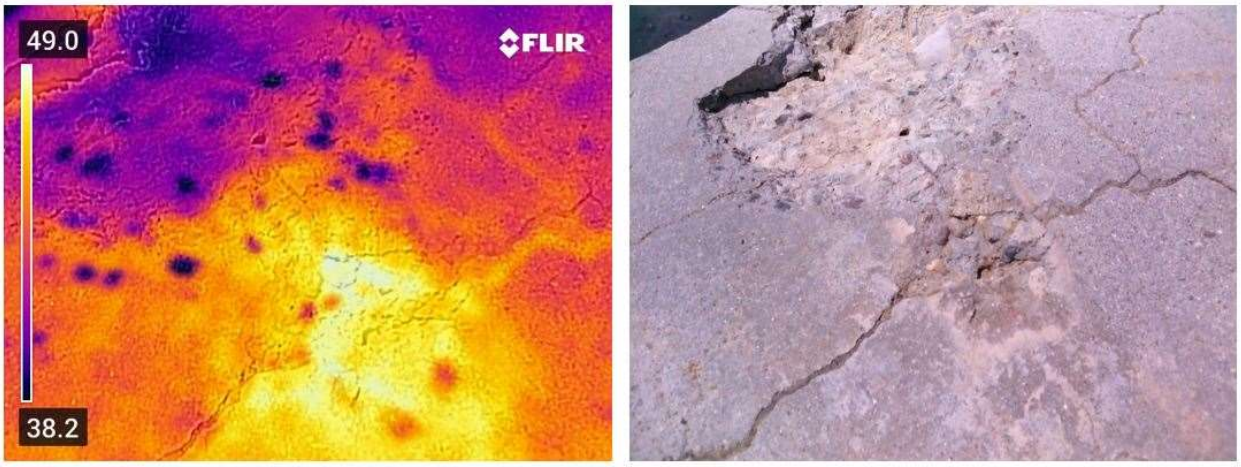

(a) Thermal Infrared Image (b) Natural Color Image

Figure 17. An illustration of the collected thermal-infrared image and matching natural color image.

4.2. Data Processing

This section focuses on discussing the major steps of using SfM technique to process the collected hyper-spatial natural color aerial photos to derive co-registered orthophotos and DSMs, which are then used as the input to the crack detection tool. It should be noted that post-processing of the collected thermal infrared photos is not required. That being said, the collected thermal infrared photos will be used directly as the input to the delamination detection tool.

As aforementioned, SfM is a photogrammetric technique that can be used to create 3D objects by analyzing overlapping aerial images captured from varied perspective at approximately the spatial resolution of input images *(17-18)*. For instance, if the input aerial photos have a spatial resolution of 5 mm, the output orthophotos and DSMs will have approximately same spatial resolution (i.e., 5mm).

In recent years, many commercial or free and open sources software programs for SfM have emerged. The project team has access to a few of them, including Agisoft Metashape, Menci APS, Pix4D Mapper, Trimble Inpho UASMaster, DroneDeploy, Imagine UAV, ArcGIS Drone2Map, PhotoMOD UAS, WebODM, and VisualSFM. Both WebODM and VisualSFM are free and open source, and the remaining programs are commercial. The project team has explored all software packages and evaluated them in the following criteria shown in Table 6: (1) operational simplicity (e.g., learning curve); (2) control parameters (e.g., the amount of available parameters for the output products); (3) output quality; (4) processing speed; and (5) cost. Each of the criteria was scored on a scale of 1 to 5 (1 = Very Poor, 2 = Poor, 3 = Fair, 4 = Good, and 5 = Very Good). The total score for a perfect option will be 25, and a passing grade needs to be 15 (60%).

Table 6. A list of available software programs for SfM.

Software	Operational Simplicity	Control Parameters	Output Quality	Processing Speed	Cost	Total Score
Agisoft Metashape	5	5	5	5	$3,499 perpetual (4)	24
Menci APS	5	3	4	5	$6,300 perpetual (2)	19
Pix4d Mapper	5	4	4	4	$4,990 perpetual (3)	20
Trimble Inpho UASMaster	4	3	3	4	$9,680 perpetual (1)	15
DroneDeploy	5	4	4	5	$5,400 annual (4)	22
Imagine UAV	3	3	3	3	$5,200 Perpetual (4)	16
ArcGIS Drone2Map	4	3	4	3	$1,500 Annual (5)	19
PhotoMOD UAS	3	4	4	3	$2,300 perpetual (5)	19
WebODM	5	2	3	5	Free (5)	20
VisualSFM	3	2	2	5	Free (5)	17

As it revealed in Table 6, based on the project team's evaluation, the best software program (the one with the highest score) for SfM is Agisoft Metashape. The project team used this software to conduct SfM to process the collected hyper-spatial resolution natural color aerial photos. This software is previously known as Agisoft Photoscan, which was developed by Agisoft LLC. It is widely used in the UAS mapping field and it can run on multiple operating systems, including Microsoft Windows, MacOS, and Linux.

The following section discusses the general steps in SfM. It should be noted that no matter what software programs are used to conduct SfM, the steps below are generally involved. This section focuses on discussing the main concepts underlying the SfM method. Detailed mathematical equations or algorithms are intentionally not discussed. That said, the section aims to present the typical processed involved in the reconstruction of 3D geometry from a sequence of overlapped standard aerial imagery.

In photogrammetry and remote sensing, the full name of the technique used to process S-UAS acquired aerial photos to generate co-registered orthophotos and DSMs is referred to as Structure-from-Motion and Multiple-View Stereo (SfM-MVS), which is also known as aerial triangulation (AT). SfM is only one of the steps in SfM-MVS. For simplification purpose, this study used SfM to indicate SfM-MVS. There are eight primary steps in SfM (Figure 18), which are discussed in the following sections. It should be noted that the keypoint correspondence step and the keypoint filtering step are conducted concurrently in a typical software program.

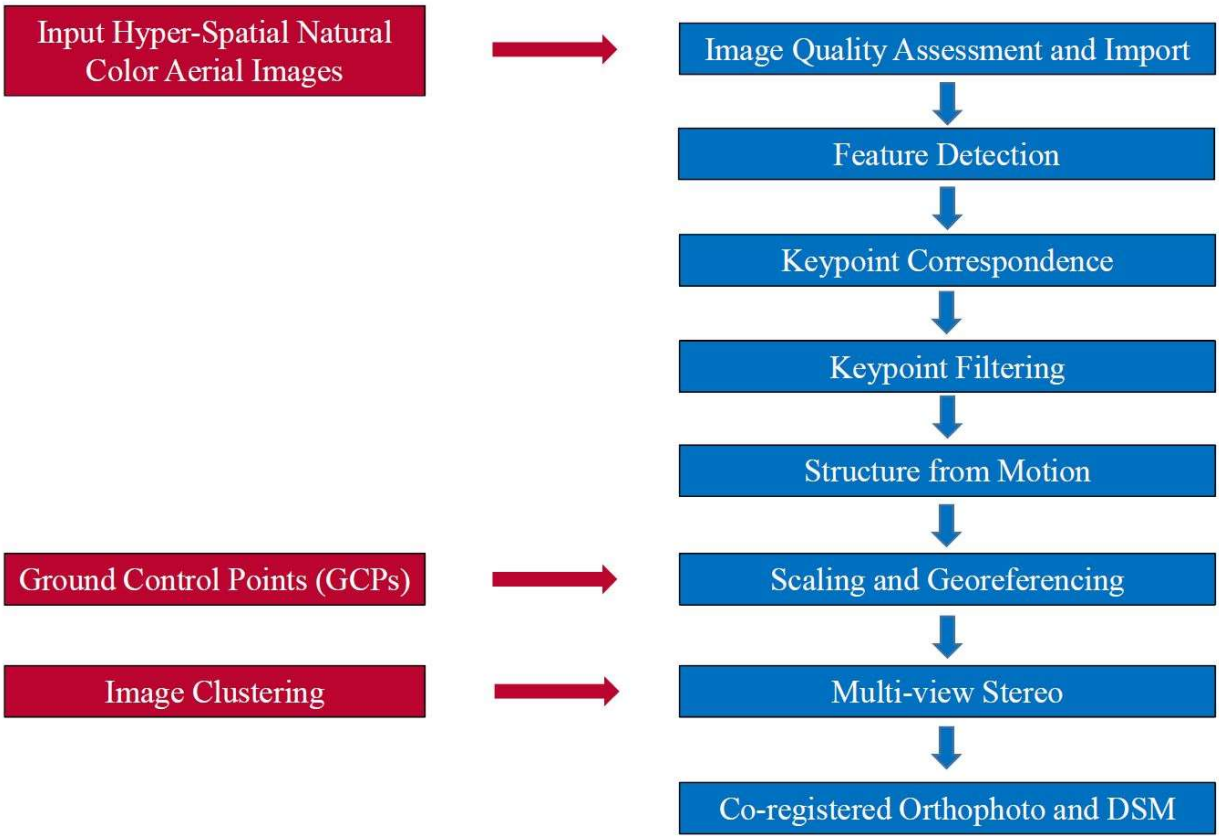

Figure 18. The typical steps in SfM. Blue color items indicate steps while red color items indicate inputs.

4.2.1. Image Quality Assessment and Import

In this step, each collected hyper-spatial resolution aerial photo will be assessed in four criteria to ensure its quality, including brightness, contrast, sharpness, and coordinates. Brightness refers to the overall lightness or darkness of the photo. Contrast refers to the difference in brightness between objects or sections in the photo. Sharpness refers to clarify of detail in the photo. An aerial photo in good quality should have balanced brightness, contrast, and sharpness. Additionally, each aerial photo should be assessed to examine if they have been geotagged. That said, each aerial photo should be assessed to examine if they have missing geographic coordinate information. An aerial photo should be excluded from processing if they are blurry and unusable (e.g., not geotagged). For this study, all 92 aerial photos are in good quality and they can be imported into Agisoft Metashape for the next processing step.

4.2.2. Feature Detection

This step focuses on identifying common points on several aerial images that are overlapped and then matching a point to itself in each image (Figure 19). These points are referred to as keypoints, and they enable the different photos to be matched and the scene geometry to be reconstructed. This is a computational challenging task because keypoints need to be matched on images with variable 3D position, scale, and orientation *(29)*. Many techniques have been developed to identify keypoints, and each of them has both strengths and weakness. The widely adopted method for identifying keypoints focuses on recognizing feature object (a group of pixels that comprise an

object in the photo) and then locating each matching keypoint. The feature detection algorithm used in Agisoft Metashape is the scale-invariant feature transform (SIFT) object recognition system *(30)*.

Figure 19. An illustration of the concept of keypoint identification (adopted from opencv.org). The blue points are keypoints identified in each image.

4.2.3. Keypoint Correspondence

Once keypoints have been identified and located in each aerial image, correspondence between keypoints in different images need to be determined and established (Figure 20). It should be noted that there is no assurance that any given keypoint will definitely have a matching point in another image, and therefore, this step involves discarding points without matching partner as well. There are many methods for determining and establishing correspondence between keypoints, and as for feature detection, each of them has both strengths and weaknesses. In Agisoft Metashape, the method for determining and establishing keypoint correspondence, which is also implemented by SIFT, is the approximate nearest neighbor (ANN) method *(31)*.

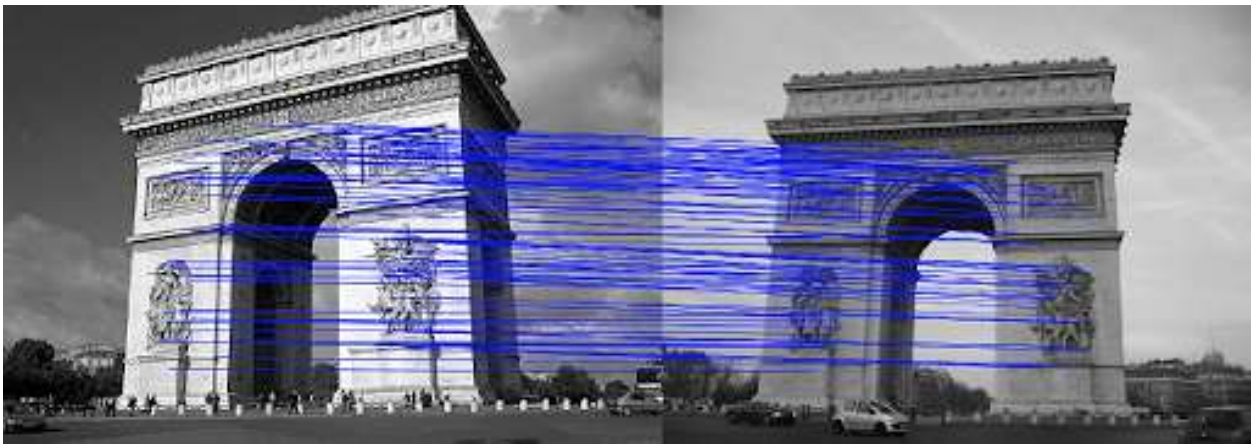

Figure 20. An illustration of the concept of keypoint correspondence (adopted from ismailsirma.com). The blue lines are established keypoint correspondence.

4.2.4. Keypoint Filtering

To obtain high-quality keypoint correspondence, a further step is needed to filter out any erroneous matches to ensure that only correct ones remain. Many methods are available for the filtering process, but each of them has both strengths and weaknesses. The method used by Agisoft Metashape is a robust and accurate Random Sample Consensus (RANSAC) filter *(30)*. The

RANSAC method assumes that all keypoints can be divided into two groups, including outliers and inliers. All outliers will be removed from the keypoint correspondence dataset.

4.2.5. Structure from Motion (SfM)

This step focuses on estimating camera poses as well as the 3D geometry of a scene. In this step, the geometrically correct keypoint correspondence identified in the previous section is used to estimate extrinsic camera calibration parameters (e.g., camera positions and orientations) and intrinsic camera calibration parameters (e.g., sensor distortions). After the camera parameters are estimated, bundle block adjustment is used for simultaneously refining the 3D coordinates describing the scene geometry, the parameters of the relative motion, and camera calibration parameters. Bundle block adjustment produces jointly optimal 3D structure and viewing parameter estimates using all input images simultaneously *(32)*. At the end of this step, a sparse point cloud and reconstructed camera poses are generated (Figure 21). The sparse point cloud is used in many applications of SfM, although further processing such as multiple-view stereo is required to create more detailed scene surface. For this study, a sparse point cloud with a total 3,479,183 points was created.

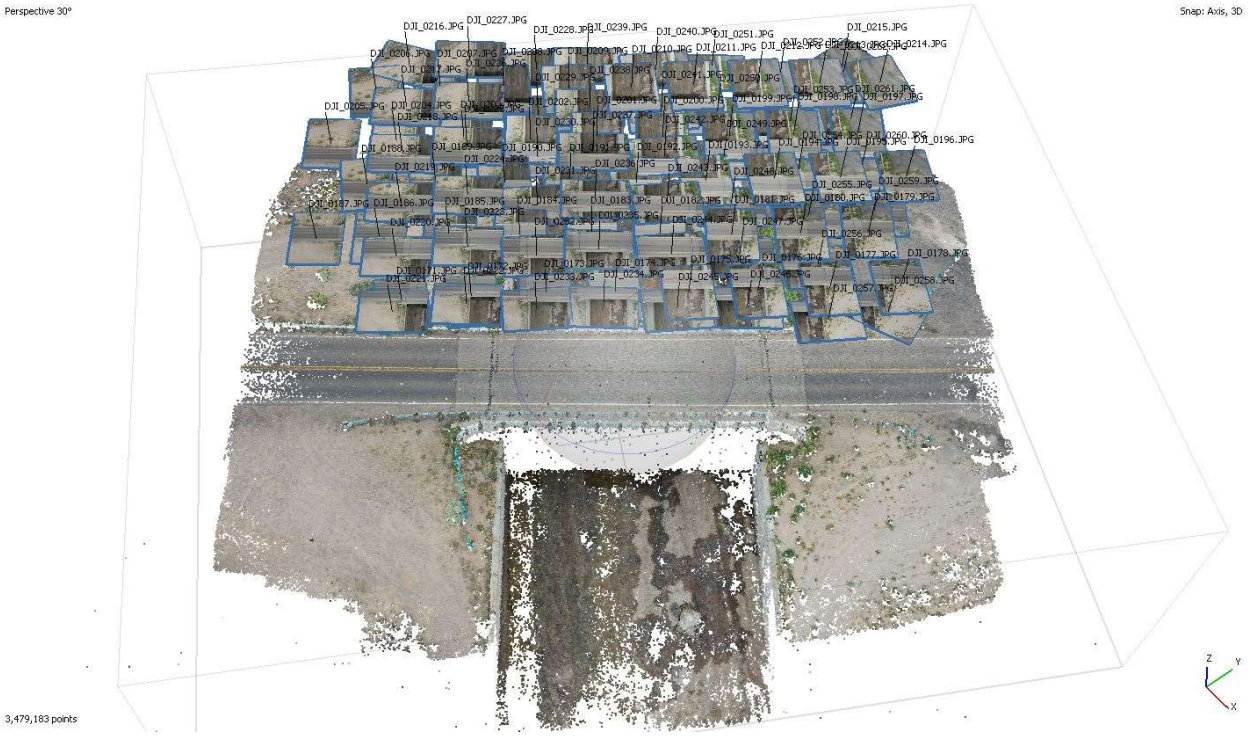

Figure 21. An illustration of reconstructed sparse point cloud and camera poses.

4.2.6. Scaling and Georeferencing

It should be noted that the SfM step only estimates relative camera locations and scene geometry. Absolute distances between cameras or between reconstructed points cannot be recovered from aerial images alone, regardless of how many cameras or points are used *(33)*. If the aerial photos are not geotagged, the output sparse point cloud is produced in an arbitrary coordinate system. If the aerial photos are geotagged, the output sparse point cloud is produced in a coordinate system as the aerial photos. Although the aerial photos used in this study are geotagged, in general the

built-in GPS receiver in S-UAS is not as accurate as a ground survey unit, which leads to a 3D scene geometry with low accuracy. Therefore, this study used GCPs surveyed with RTK equipment are used to improve the accuracy of the 3D coordinates describing the scene geometry. Figure 22 shows the use of GCPs to georeference and scale a sparse point cloud.

It should be noted that S-UAS with onboard RTK receiver can greatly improve geometry accuracy of the sparse point cloud, but most S-UAS only have built-in GPS receivers. It should also be noted that accuracy requirement varies – it depends on survey purposes. Fine-scale distresses are expected for bridge condition evaluation, and therefore, a 3D scene with high-accuracy geometry (i.e., sub-centimeter level) is recommended. However, for other purposes such as terrain mapping for a large area, a 3D scene with low-accuracy geometry (e.g., sub-meter) is generally suggested, and therefore, built-in GPS receivers are adequate.

Markers	Longitude	Latitude	Altitude (m)	Accuracy (m)	Error (m)	Projections	Error (pix)
point 1	-106.599462	35.204256	1513.585000	0.005000	0.198197	36	0.953
point 2	-106.599424	35.204270	1513.600000	0.005000	0.170981	38	0.572
point 3	-106.599384	35.204337	1513.629000	0.005000	0.137583	43	0.590
point 4	-106.599271	35.204423	1513.607000	0.005000	0.115457	29	0.361
point 5	-106.599255	35.204388	1513.853000	0.005000	0.113435	29	0.550
point 6	-106.599411	35.204239	1513.724000	0.005000	0.114228	31	0.712
point 7	-106.599290	35.204441	1513.570000	0.005000	0.182897	34	0.867
point 8	-106.599361	35.204361	1513.618000	0.005000	0.157935	42	0.540
point 9	-106.599458	35.204303	1513.567000	0.005000	0.162073	40	0.673
point 10	-106.599488	35.204254	1513.586000	0.005000	0.121016	34	0.512
Total Error							
Control points					0.150333		0.656

Scale Bars	Distance (m)	Accuracy (m)	Error (m)
Total Error			
Control scale ...			
Check scale b...			

Figure 22. An illustration of using GCPs for georeference and scaling a sparse point cloud.

4.2.7. Multi-View Stereo (MVS)

This step uses SfM estimated camera parameters to create depth maps to conduct dense reconstruction. Many methods are available for MVS, and each of them has both strengths and weaknesses, but in general, they can be classified into three groups, including Voxel-based methods, surface evolution-based methods, depth map merging methods, and patch-based methods *(34)*. Agisoft Metashape uses depth map merging method, which builds a depth map for each image and merges them to produce a dense reconstruction. This allows for parallelization but at the expense of noisy and highly redundant depth maps that require further post-processing to clean and merge *(35)*. When the amount of image increases, the required random-access memory (RAM) for depth map merging method increases rapidly and issues of scalability emerge. The solution to this RAM issue is image clustering, which splits a large project into many small chunks. For this research project, the amount of input aerial photos is 92, which does not need image clustering. A computer with 64GB RAM should be able to process 1,000 aerial images with ultra-high quality, which is sufficient for most bridges in the U.S. This step creates a georeferenced and scaled dense

point cloud (Figure 23). For this study, a sparse point cloud with a total 126,609,438 points was created.

Figure 23. An illustration of a reconstructed dense point cloud.

4.2.8. Co-Registered Orthophotos and DSMs

The dense point cloud generated in the previous step is used in this step to create a triangulated irregular network (TIN) mesh. Subsequently, the dense point cloud is rasterized to create a DSM, which is a grid representation of the Earth surface. The DSM is then used as a project surface during orthocorrection of the input aerial images. The orthocorrected images are then mosaicked to generate an orthophoto that is co-registered with the DSM. The orthophoto and DSM are generated in a single processing routine and they can be exported as rasters in GeoTIFF format. For this study, the exported orthophoto and DSM are at a spatial resolution of 0.005 m (Figure 24).

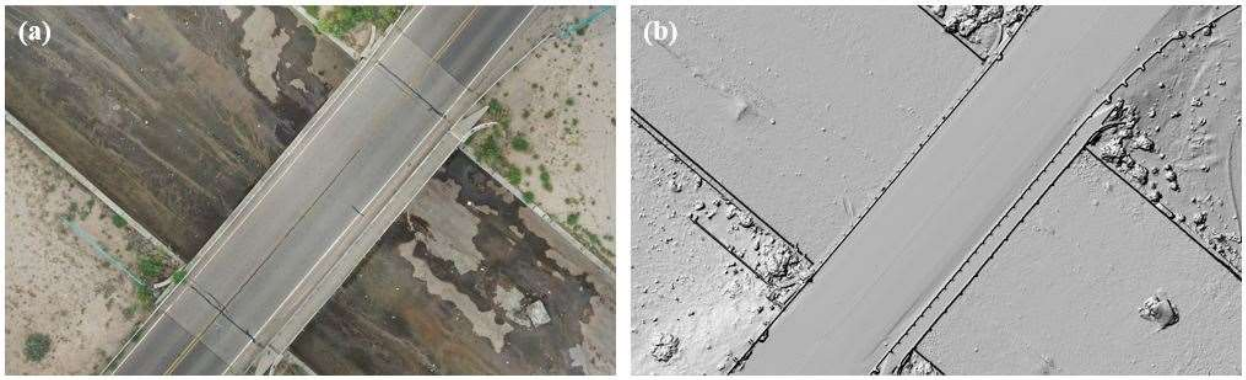

Figure 24. An illustration of a co-registered orthophoto (a) and DSM (b).

4.3. Analysis Tool Development

For this task, a toolset that is compatible with standard GIS software program (i.e., ArcGIS ArcMap) was developed to analyze the natural color orthophoto and DSM as well as thermal-infrared imagery to extract bridge deck wearing surface distresses (i.e., cracking) and subsurface distress (i.e., delamination). Specifically, the co-registered natural color orthophoto and DSM were analyzed to extract bridge deck wearing cracking. Additionally, the thermal-infrared imagery was analyzed to extract subsurface delamination. It should be noted that this toolset was developed with the Python programming language.

4.3.1. Cracking Extraction Tool

Cracking extraction tool was developed with three image processing techniques, including image enhancement, image fusion, and image difference. This tool has two primary outputs, including an orthophoto and DSM fused image to accentuate bridge deck wearing surface cracking and a height difference image to highlight bridge deck wearing surface cracking.

In this tool, eight shaded relief images are created from the input DSM at a 45-degree interval (i.e., 45, 90, 135, 180, 225, 270, 315, 360 degrees). Then an average of these eight shaded relief images are conducted to create a mean shaded relief image. Additionally, the orthophoto is used to create an albedo image based on the average pixel value of the visible red, green, and blue bands. Finally, the mean shaded relief image and the albedo image are fused based on an average operation to create the fused image to accentuate bridge deck wearing surface cracking (Figure 25).

Figure 25. An illustration of the orthophoto and DSM fused image.

This tool also conducts image enhancement to the DSM image through a 5 x 5 focal statistics tool with maximum values to enhance geometric information. Then the enhanced DSM and the original DSM are differenced based on a subtract operation to create a differenced DSM image. Subsequently, the differenced DSM image is reclassified to assign null values to any pixels that

have an elevation value that is greater than 0.016 m. (0.75-inch). According to Mr. George Baca, most wearing surface cracks are less than 0.016 m. Figure 26 shows the height difference image to highlight bridge deck wearing surface cracking.

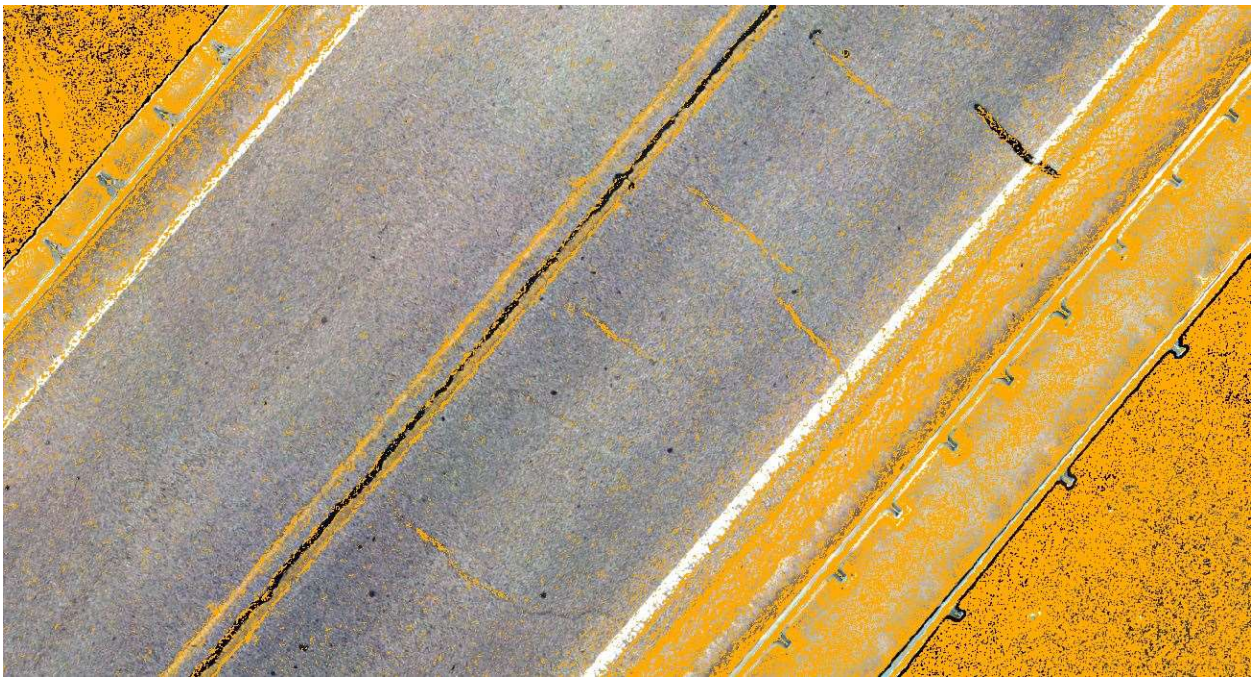

Figure 26. An illustration of the enhanced DSM and original DSM differenced image.

4.3.2. Delamination Extraction Tool

Delamination extraction tool was developed with a couple of image processing techniques, including principal component analysis (PAC) and OBIA. PCA can reduce the dimensionality of an image. It transforms an original band correlated image into a substantially smaller set of un-correlated components. The result of this technique is a multiband image with the same number of bands as the specified number of components. The input thermal-infrared image has three bands, and therefore, the output image of PCA has three components. The delamination section was most noticeable in the second component, and therefore, Component 2 was used as the input for the following step of OBIA (Figure 27).

As mentioned in the Literature Review section, OBIA segments an image by grouping pixels together into vector objects, which are then used for the classification process (assigning a pixel or a group of pixels to a land cover class). The segmentation process defines homogenous image pixels into spectrally, spatially, geometrically, and contextually similar regions. These regions Couple with the Random Forest Classifier, OBIA was used to segment the Component 2 image. The resultant segmented image has a pixel value range of 19 to 251. The project team examined the segmented image and identified that any pixels that have a value greater than 125 were located in the delamination area. Subsequently, only the pixels that have a value greater than 125 were selected and the remaining pixels were set to no values (null). The selected pixels were polygonized and exported as a single shapefile for further engineering evaluation (Figure 28). It should be noted that the delamination shapefile is not georeferenced, and therefore, it can only help locate the delamination spot. Users are recommended to use their GPS enabled cell phone or cameras to capture a picture of the same scene for revisiting purposes.

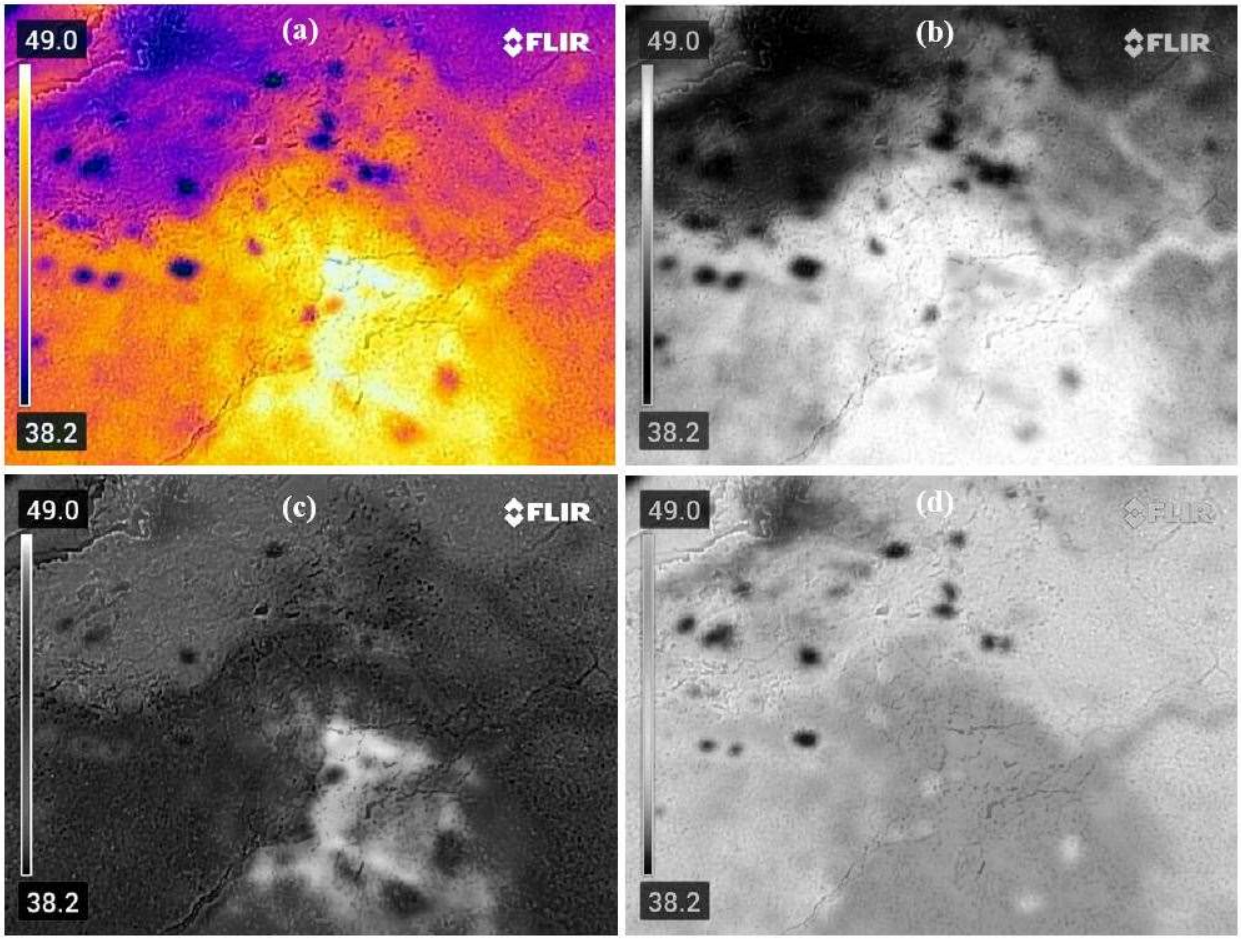

Figure 27. An illustration of PCA with the original thermal-infrared image and three components; (a) original thermal-infrared image; (b) the Component 1 image; (c) the Component 2 image; (d) the Component 3 image. Degree Celsius.

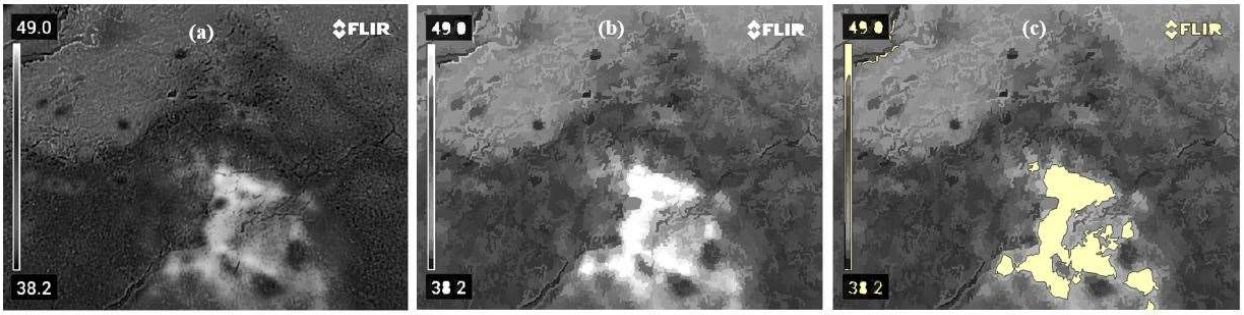

Figure 28. An illustration of OBIA with the Component 2 image. Specifically, Figure 28 (a) shows the Component image; Figure 28 (b) shows the segmented image; and Figure 28 (c) show the polygonized hotspot to indicate the delamination location.

4.4. Accuracy Validation

For this task, the project team conducted a validation study to investigate the accuracy of the detected bridge deck wearing surface cracking and subsurface delamination. For bridge deck wearing surface cracking evaluation, the project team studied the count, length, and width of the detected cracks. For count study, the fused image and the differenced image were used separately

and jointly to digitize cracks. Then the successful detection rates were studied. For length and width study, the project team obtained the measurements from the images and then statistically compared them with the ground-truth measurements. The project team had a sample size of 16, which is less 30, and therefore non-parametric statistical tests were used in this study *(36)*. Non-parametric Wilcoxon Signed Rank Test and Mann-Whitney U Test were used to examine if aerial imagery-based measurements and ground-based measurements are statistically similar. For subsurface delamination evaluation, the project team digitized the delamination area based on the thermal-infrared image and then compared it with the tool detected area. However, the project team cannot conduct any formal statistical test because there are no adequate samples. Detailed information for accuracy validation is provided in the Analysis and Findings section.

5. ANALYSIS AND FINDINGS

This section focuses on discussing the analysis results and findings. It should be noted that some of the results have been discussed in the Methodology section, and therefore, they are not discussed in this section again to avoid duplication work.

5.1. Data Collection Results

An S-UAS, DJI Mavic Pro 2 was selected as the optimal platform for hyper-spatial natural color aerial imagery collection. A handheld Flir C5 camera was selected as the sensor for thermal-infrared imagery collection. A set of 92 hyper-spatial resolution aerial photos were successfully collected with the selected S-UAS. A thermal-infrared image was also successfully collected.

5.2. Image Processing Results

Hyper-spatial resolution natural color aerial images (0.005 m) were processed with SfM technique to create a co-registered orthophoto and DSM. The orthophoto is a natural color image that has a spatial resolution of 0.005 m. The DSM is a single band image with Z values depicting elevations of the top of reflective surfaces such as building and vegetation. Figure 29 shows the co-registered orthophoto and DSM in shaded relief view. As it shows in this figure, the cracks on the wearing surface are observable in both Orthophoto and DSM. The cracks in the orthophoto are visible but the observation is lack of depth perception. When coupled with DSM, cracks are not only visible but also depth perceptible, which enables cracking detection simpler.

Figure 29. An illustration of the SfM products; (a) an overview of the orthophoto; (b) an overview of the DSM in shaded relief view; (c) a zoomed in view of the orthophoto; and (d) a zoomed in view of the DSM in shaded relief view.

5.3. Analysis Tool Development

An analysis toolset was successfully developed by the project team. This toolset has two tools, which include a cracking detection tool (Figure 30) and a delamination detection tool (Figure 31).

Both tools were developed with the Python programming language and the code base will be make publicly available and accessible through EDAC's GitHub account. Detailed methods and steps of developing these tools can be found in the Methodology section. Additionally, detailed instruction on how to use these tools are provided in Appendix A. The project team will also develop an instruction video and upload it to EDAC's YouTube channel.

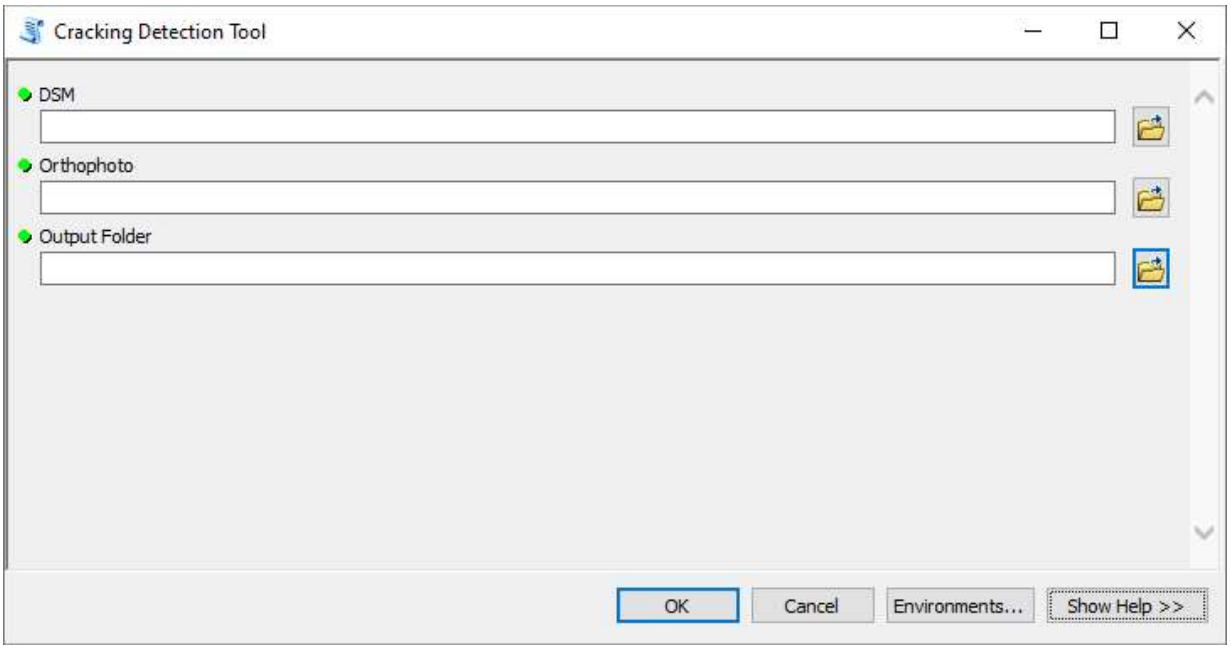

Figure 30. The user interface of the cracking detection tool.

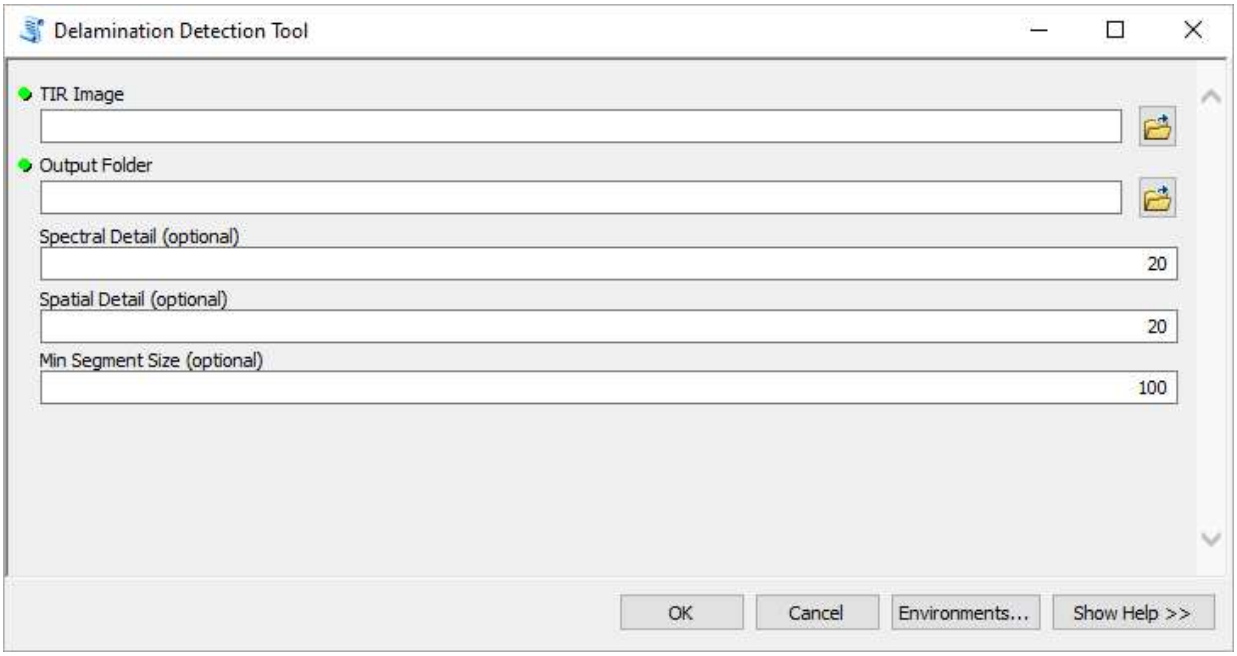

Figure 31. The user interface of the delamination detection tool.

The cracking detection tool was developed to detect cracks on the wearing surface of a bridge deck. As it shown in Figure 30, users only need to provide a co-registered orthophoto and DSM and the tool will automatically produce two maps with one accentuating cracks and another one highlighting cracks. That being said, this tool only needs two input parameters – an orthophoto and a DSM. Subsequently, the use of this tool is straightforward, and the learning curve is not deep. Figure 32 shows workflow of the cracking detection tool.

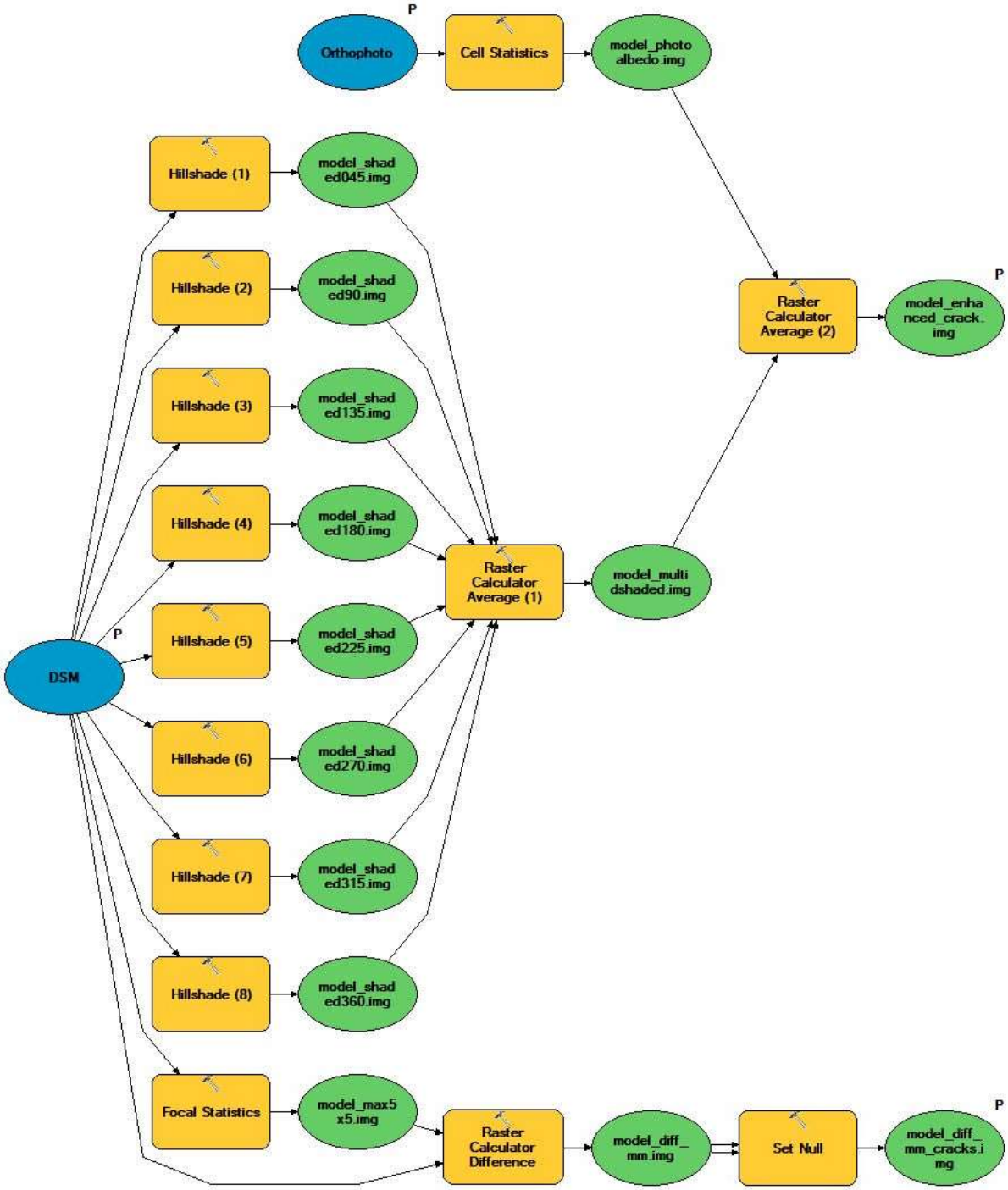

Figure 32. The workflow of the cracking detection tool.

The delamination detection tool was developed to detect delamination spots in a bridge deck. As it shown in Figure 31, users need to provide a thermal-infrared image and then provide values for spectral detail, spatial detail, and minimum segment size in pixels. Users are encouraged to use the default values of 20, 20, and 100, respectively. Spectral detail indicates the level of importance of spectral difference to identify features, and its values range from 1.0 to 20.0. A higher value is more appropriate when the individual features to be identified have similar spectral characteristics. Spatial detail indicates the level of importance of proximity to identify features, and its values range from 1.0 to 20.0. A higher value is more appropriate when the individual features to be identified are small and clustered together. Minimum segment size in pixels indicate a size that any segment smaller than it will be merged to create a segment section. Figure 33 shows the workflow of the delamination detection tool.

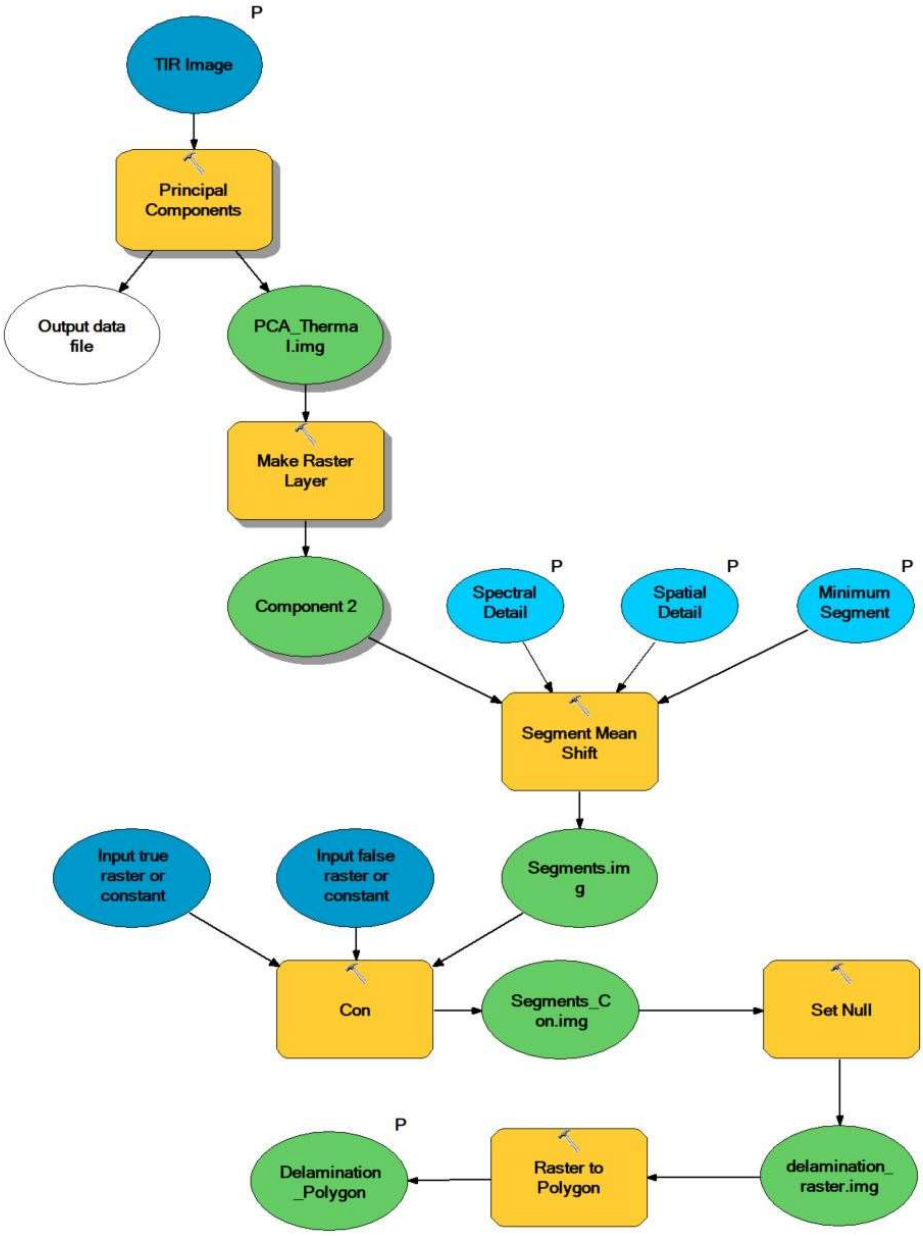

Figure 33. The workflow of the delamination detection tool.

5.4. Accuracy Validation

5.4.1. Wearing Surface Cracking Validation

For count accuracy validation, the project team used the ground survey results as the ground-truth data. The total amount of cracks identified through field survey is 16 (Figure 34). When using only the crack-highlighting image, ten cracks were identified, including crack ID 2, 3, 5-9, 12, and 14 (Figure 35). However, when using only the crack-accentuating image, all 16 cracks were successfully identified (Figure 36). The results were summarized in Table 7.

Results revealed that the crack-accentuating image can effectively identify cracks on the wearing surface of a bridge deck. In addition, the crack-highlighting image cannot effectively identify all cracks. However, crack-highlighting image can assist bridge inspectors with quick engineering reviews and high-level information checks. It also provides a good starting point for crack identification. When coupled with the crack-accentuating image, crack-highlighting image can also be effectively used to identify cracks on the wearing surface of a bridge deck.

Figure 34. The locations of the cracks identified through field survey.

Table 7. A Summary of the Identified Cracks through Various Methods.

Methods	Identified Cracks	Total Cracks	Successful Rate
Ground Survey	16	16	100%
Crack-Highlighting Image Survey (1)	9	16	56%
Crack-Accentuating Image Survey (2)	16	16	100%
Combination of (1) and (2)	16	16	100%

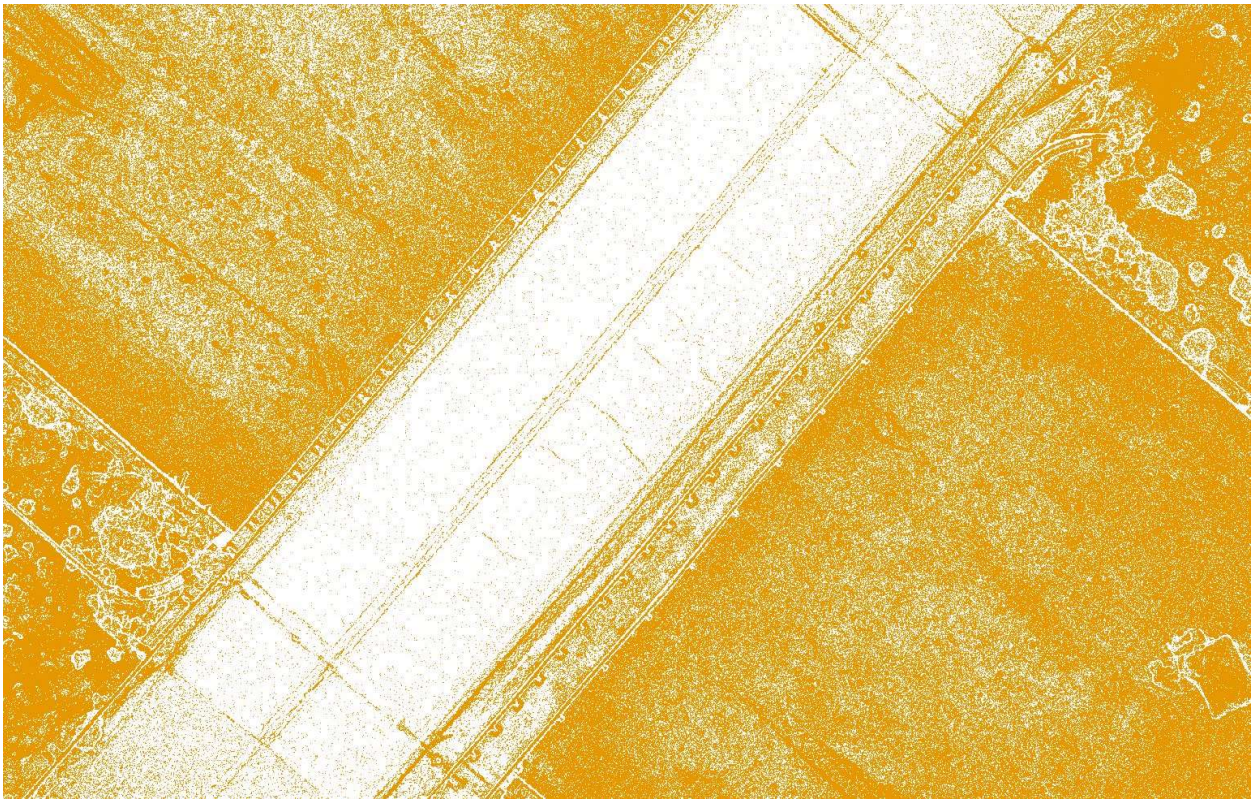

Figure 35. The cracks identified when using the crack-highlighting image.

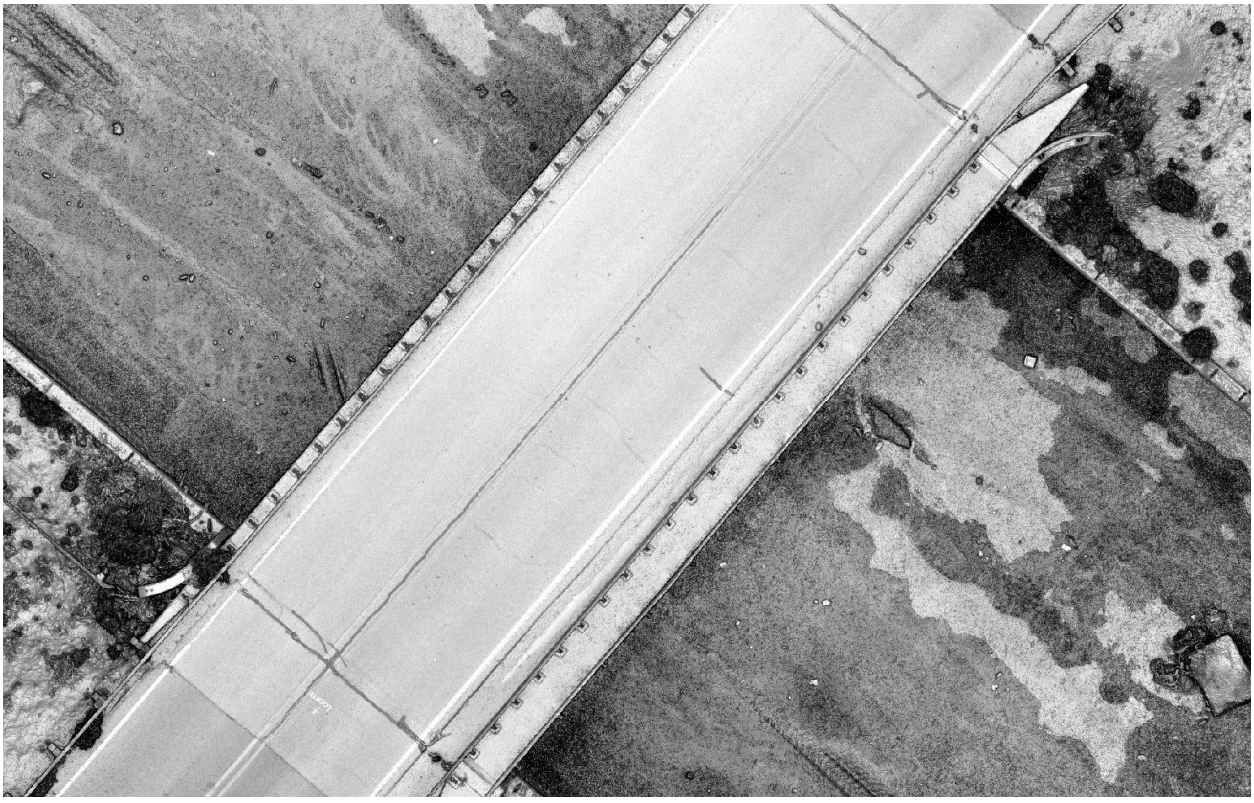

Figure 36. The cracks identified when using the crack-accentuating image.

For length and width accuracy validation, the project team also used the ground survey results as the ground-truth data. In addition, the project team used the orthophoto to conduct on-screen image measurement to record the length and width for each crack. The measurement results were summarized in Table 8.

Table 8. A Summary of Crack Length and Width Measurements.

Crack ID	Length Ground Survey (meter)	Length Orthophoto Survey (meter)	Width Ground Survey (meter)	Width Orthophoto Survey (meter)
1	2.675	2.673	0.023	0.021
2	1.875	1.871	0.029	0.025
3	2.965	2.959	0.013	0.015
4	0.641	0.648	0.015	0.013
5	1.089	1.095	0.011	0.013
6	1.270	1.268	0.025	0.026
7	1.564	1.562	0.022	0.024
8	1.147	1.153	0.013	0.017
9	0.686	0.687	0.021	0.018
10	0.075	0.077	0.023	0.022
11	0.675	0.672	0.018	0.016
12	0.961	0.963	0.020	0.016
13	0.728	0.731	0.017	0.016
14	2.247	2.240	0.013	0.011
15	1.495	1.492	0.017	0.018
16	1.397	1.395	0.022	0.019

The histogram distribution pattern of length and width measurements were presented in Figure 37. As it shows, for length measurements, ground survey results exhibit the same histogram distribution pattern. For width measurements, ground survey results exhibit similar histogram distribution. This is because there are not many samples and the measurement interval may affect the visualization results. Therefore, a box plot was also used to examine the distribution pattern of length and width measurements. Figure 38 and Figure 39 were used for length measurements and width measurements respectively to investigate if the ground-based measurements and the orthophoto-based measurements have substantial difference in medians. As shown in Figure 38, box plot did not show a substantial difference in the medians between ground-based length measurements and orthophoto-based length measurements. There also did not appear to be a substantial difference in the box sizes. As shown in Figure 39, box plot did not show a substantial difference in the medians between ground-based width measurements and orthophoto-based width measurements. However, there appeared to be a minor difference in the box sizes. No aforementioned plots revealed a substantial difference in the shape and spread of distribution between the two sets of measurements for both crack length and width.

Continuing with visual analysis, formal statistical tests were conducted. It should be noted that the measurement results were compared as a paired group and unpaired group. Paired group tests are more appropriate when the two groups of measurements are dependent (e.g., repeated measurement for the same subject but at two different time). Unpaired group tests are more appropriate when the two groups of measurements are independent (e.g., measurement for one

sample in Group A has no influence on the measurement for one sample in Group B). The relationship between ground-based measurement and orthophoto-based measurement can be interpreted in both a dependent way and independent way, and therefore, both of them were performed in this study.

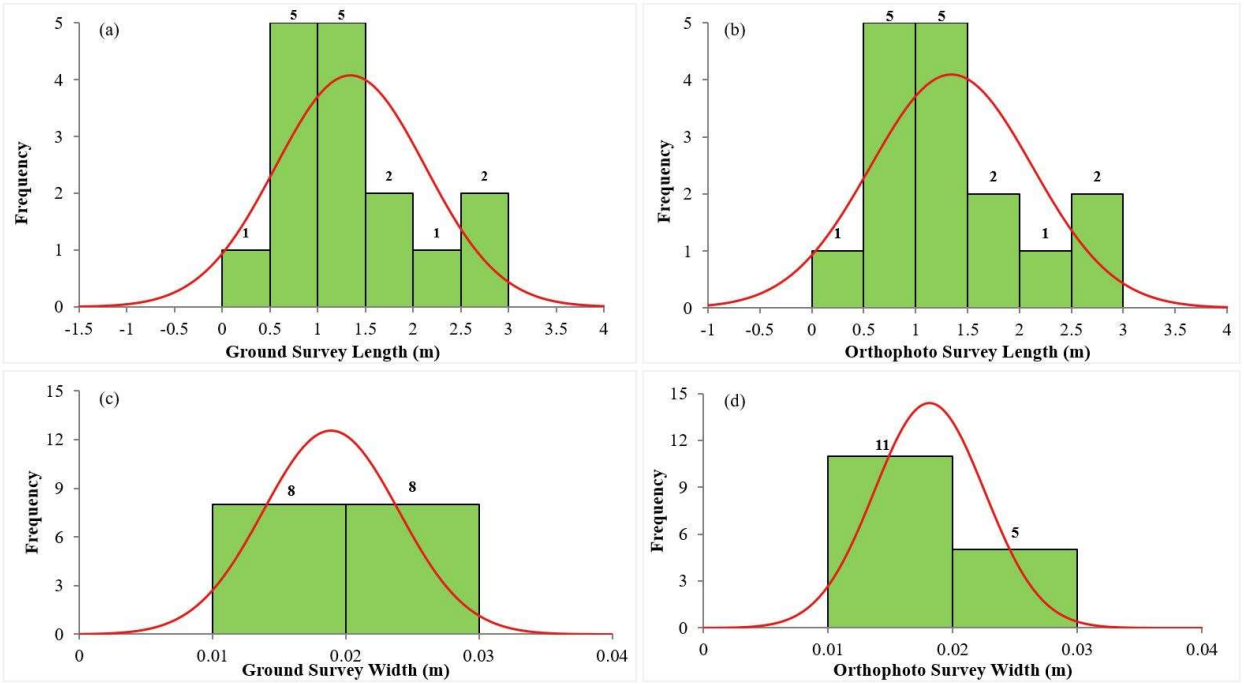

Figure 37. Histogram shapes of crack length and width measurements; (a) ground survey length; (b) orthophoto survey length; (c) ground survey width; and (d) orthophoto survey width.

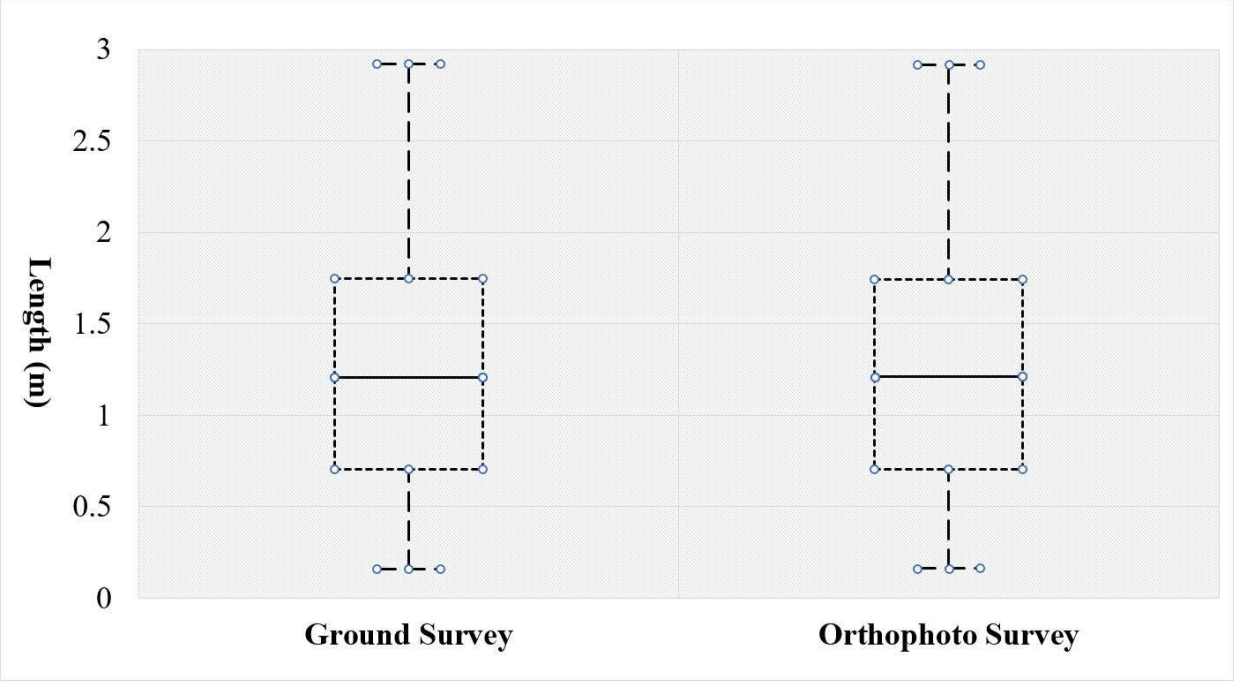

Figure 38. Box plot of crack length measurements; (a) ground survey length; and (b) orthophoto survey length.

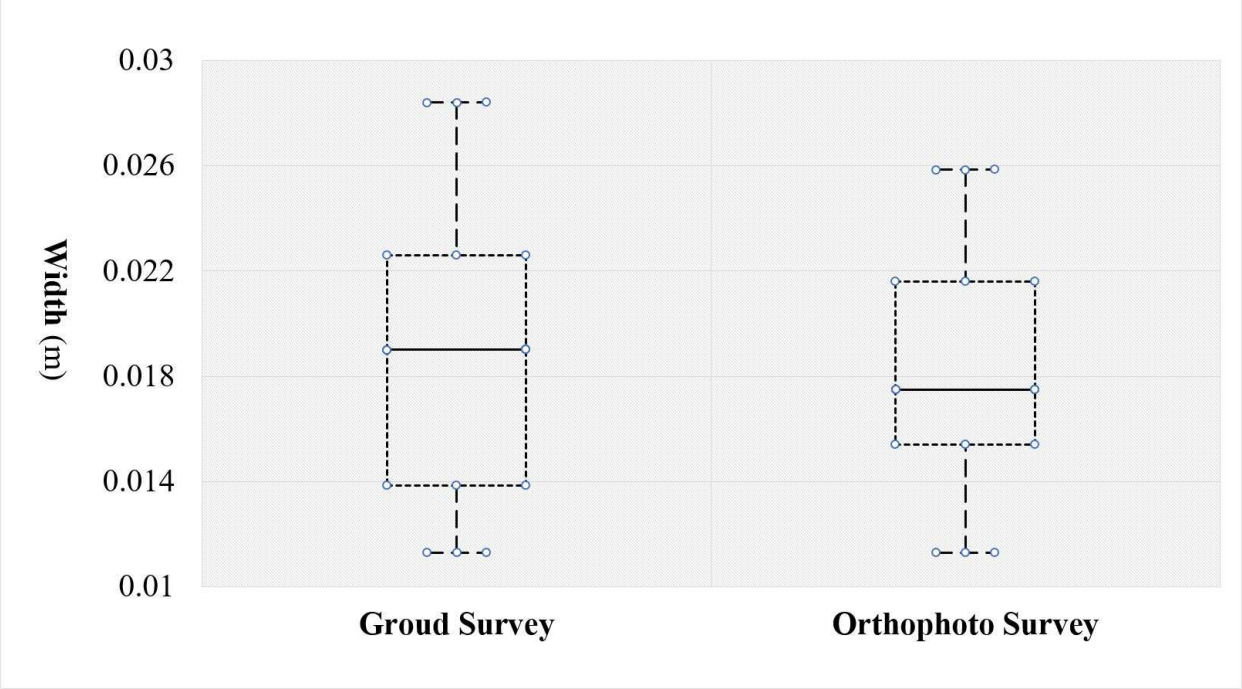

Figure 39. Box plot of crack width measurements; (a) ground survey width; and (b) orthophoto survey width.

In the dependent way, repeated measurements of length and width for a specific crack were performed on the ground and from the orthophoto at two different times, and therefore, they are dependent. In the independent way, the ground-based measurements of a specific crack have no influence on the orthophoto-based measurements because they are measured from two different data sources. Since the relationship can be interpreted in both ways, to err on the side of caution, this research used both paired group and unpaired group statistical tests.

As previously mentioned in the Methodology section, non-parametric Wilcoxon Signed Rank Test and Mann Whitney U Test were used to examine if ground-based length and width measurements are statistically different from orthophoto-based length and width measurements. This is because the sample size is 16, which is less than 30 *(36)*, which indicates the sample values might not be normally distributed. Parametric statistical tests assume a normal distribution lf values. More specifically, the Wilcoxon Signed Rank Test is a paired group test, and its matching parametric test is paired T-test, while the Mann Whitney U Test is an unpaired group test, and its matching parametric test is unpaired T-test.

Wilcoxon Signed Rank Test was performed to compare the measurement results of both length and width at the paired group level. Results were summarized in Table 9. As it shown in Table 9, for both length and width measurements, the p-value is greater than 0.05, and therefore, the null hypothesis should be accepted, and subsequently indicating that for both length and width the median difference between the paired ground-based measurement and orthophoto-based measurement is zero at a 5% significance level. In other words, for both length and width, ground-based measurements and orthophoto-based measurements are not statistically different at a 5% significance level.

Table 9. Wilcoxon Signed Rank Test Results for Length and Width Measurements.

Test ID	Measurement Type	Null Hypothesis	p-Value
1	Length	The median difference between the two-paired measurements (ground-based measurement vs. orthophoto-based measurement) is zero.	0.8036
2	Width	The median difference between the two-paired measurements (ground-based measurement vs. orthophoto-based measurement) is zero.	0.4545

The Mann Whitney U Test was performed to compare the measurements in an unpaired group way. Although this test does not require normally distributed data, it requires data from each population must be an independent random sample, and the population must have equal variances. For non-normally distributed data, the Levene's Test and Bartlett's Test are usually used to examine variance equability.

For the Levene's Test and Bartlett's Test, the null hypothesis is that the population variances are equal. Test results were summarized in Table 10. For both length and width, the p-value is greater than 0.05, and therefore, the null hypothesis should be accepted, and subsequently indicating that the population variances for both length and width measurements are equal at a 5% significance level. Ultimately, the Mann Whitney U Test is appropriate for both length and width.

Table 10. Levene's Test and Bartlett's Test Results.

Type	Comparison	Null Hypothesis	Levene's Test p-Value	Bartlett's Test p-Value
Length	Ground-based vs. Orthophoto-based Measurement	Population variances are equal	0.9857	0.9891
Width	Ground-based vs. Orthophoto-based Measurement	Population variances are equal	0.4315	0.6064

Continuing with the Mann Whitney U Test, the null hypothesis is that there is no difference in the distribution (shape and spread) of ground-based length and width measurements and orthophoto-based length and width measurements. Test results were summarized in Table 11.

Table 11. Mann Whitney U Test for Length and Width.

Test ID	Measurement Type	Null Hypothesis	p-Value
1	Length	The distribution pattern of ground-based and orthophoto-based measurement is the same.	0.9699
2	Width	The distribution pattern of ground-based and orthophoto-based measurement is the same.	0.7052

For both length and width, the p-value is 0.9699 and 0.7052, respectively. This proves that the null hypothesis was accepted, which indicates there is no significant difference in the distribution pattern at a 5% significance level.

All the aforementioned test results revealed that there is no evidence showing that the ground-based length and width measurements and orthophoto-based length and width measurements are statically different at a 5% significance level. Visual examination of the plotted data also supports this finding. Ultimately, these results collectively prove that the imagery acquired by S-UAS and the developed analysis tool can be effectively used to characterize cracks on the wearing surface of a bridge, and the accuracy is comparable to that of ground-based manual measurement.

It should be noted that further investigation revealed that orthophoto-based measurements generally have lower values than ground-based manual measurement. For example, for length measurement, orthophoto-based method has nine measurements have lower values than ground-based measurement. While for width measurement, orthophoto-based method has ten measurements have lower values than ground-based measurement. This discrepancy could be from either method because measurements made by inspector in the field involve random errors and equipment errors that cannot be avoided. On the other hand, the orthophoto created in the SfM technique could also produce errors that cannot be avoided.

5.4.2. Delamination Validation

For subsurface delamination evaluation, the delamination area was digitized based on the thermal-infrared image and then it was compared with the tool detected area (Figure 40). As it shown in Figure 40, the location of the delamination area is very close, indicating that the thermal-infrared imagery and the develop analysis tool can be effectively used to characterize the subsurface delamination issues. Unfortunately, the project team cannot conduct any formal statistical test because the spatial resolution of the Flir C5 camera acquired image is unknown. The project team cannot find the camera sensor size and other specifications, which are needed for spatial resolution calculation. Additionally, at the time of conducting this research, the project team did not identify an operationally suitable S-AUS for thermal-infrared aerial imagery collection to conduct bridge deck subsurface delamination evaluation. However, in the long term, along with the technology progresses, an S-UAS for delamination evaluation could potentially be available with a low cost.

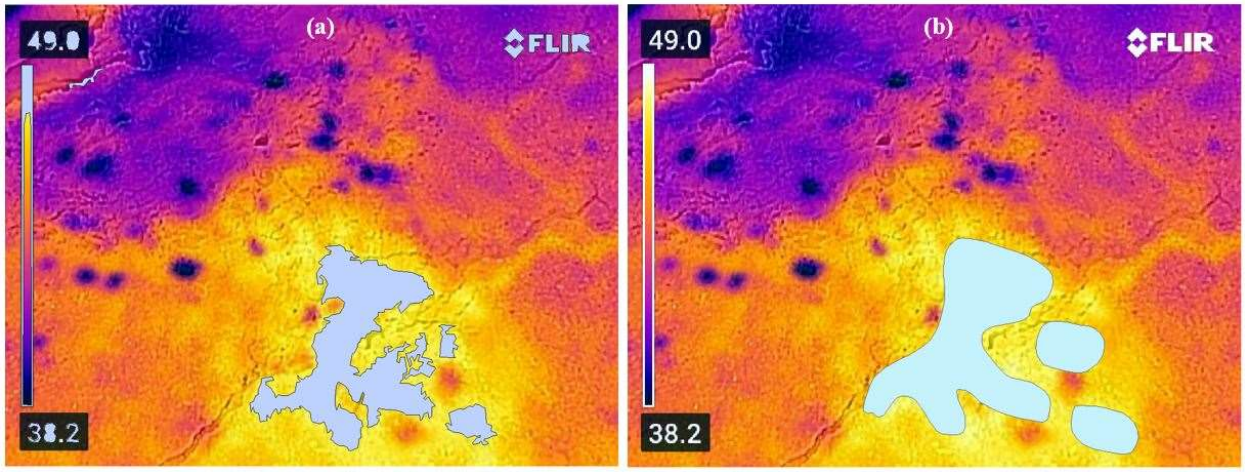

Figure 40. The detected delamination area: (a) tool detected delamination area; (b) manual detected delamination area.

6. CONCLUSIONS

Bridges are critical transportation infrastructure assets because they provide passage over physical obstacles to substantially reduce travel time and travel cost. Similar to other types of transportation infrastructure, bridges deteriorate over time. Therefore, bridges should be consistently monitored and routinely inspected to ensure their serviceability, capacity, and safety under current traffic. In the United States, routine and in-depth bridge inspections are conducted by transportation infrastructure management agencies at all levels (e.g., federal, state, local, and tribal) to detect the signs of deterioration, identify the causes, and make decisions on the distribution of limited resources for maintenance, repair, rehabilitation, and construction projects.

Traditional bridge deck inspection is conducted on the ground by having inspectors either visually inspect surface conditions or interpret the acoustic feedback from hammer sounding or chain dragging method to determine subsurface conditions. These traditional methods are expensive, time-consuming, labor-intensive, unsafe, and requiring specialized staff on a regular basis. They can also exhibit a high degree of variability.

To overcome these aforementioned challenges, the project team explored the utility of S-UAS based airborne imaging techniques in bridge deck surface and subsurface condition evaluation. The research team tested various S-UAS and selected DJI Mavic Pro 2 as the most effective one for collecting hyper-spatial resolution aerial images. The research team also tested various thermal-infrared cameras and selected Flir C5 for collecting thermal-infrared images. The research team also compared and selected Agisoft Metashape as the software application to conduct SfM for the production of co-registered hyper-spatial resolution orthophoto and DSM. In addition, the research team utilized image enhancement techniques, image fusions techniques, image difference techniques, PCA, and OBIA to analyze the derived orthophotos and DSMs to detect and evaluate bridge deck surface (i.e., cracking) and subsurface (i.e., delamination) distresses.

This research also developed a robust and powerful toolset that be used in standard GIS for operational implementation. This toolset can be used to detect and map bridge deck surface and subsurface distresses with an adequate degree of accuracy while maximizing the ability to assist inspectors with varying expertise. Research results revealed that there is no evidence showing that the ground-based length and width measurements and the orthophoto-based length and width measurements are statically different at a 5% significance level. Statistical analysis results prove that the imagery acquired by S-UAS and the developed analysis tool can be effectively used to characterize cracks on the wearing surface of a bridge, and the accuracy is comparable to that of ground-based manual measurement. In addition, the analysis tool detected location of the delamination area is very close to that of manually detected, indicating that the thermal-infrared imagery and the develop analysis tool can be effectively used to characterize the subsurface delamination issues. However, the project team cannot conduct any formal statistical analysis for delamination detection because the spatial resolution of the collected thermal-infrared imagery is unknown, which could a future research topic.

An additional benefit of the proposed bridge deck surface and subsurface distress inspection system is that the aerial photography also provides a visual record of the study area. Aerial photos can provide a synoptic view of the bridge being inspected; permitting the documentation the bridge at the time the photos were taken. Unlike textual documents, aerial photos can document scenes and events without topical selection and human interpretation.

This research also developed a guidebook on using the developed tools for professional education and training. The ultimate goal of this research is to train a new generation of transportation engineers that can effectively use the developed S-UAS based data collection and analysis system to accurately and rapidly detect, extract, and map bridge deck surface and surface distresses at a low cost.

REFERENCES

1. La, H. M., R. S. Lim, B. Basily, N. Gucunski, J. Yi, A. Maher, F. A. Romero, and H. Parvardeh. Autonomous Robotic System for High-Efficiency Non-Destructive Bridge Deck Inspection and Evaluation. *Proceedings of the 2013 IEEE International Conference on Automation Science and Engineering*, Madison, WI, 2013.

2. Rashidi, M. B. Samali, and P. Sharafi. A New Model for Bridge Management: Part A: Condition Assessment and Priority Ranking of Bridges. *Australian Journal of Civil Engineering*, 2016. 14(1): 35–45.

3. Chang, M. and M. Maguire. *Developing Deteriorate Models for Wyoming Bridges*. Final Report. Utah State University, Logan, UT, 2016.

4. Bettis, G. A. *Bridge Inspection Manual*. Manual Notice: 2020-1. Texas Department of Transportation, Austin, TX, 2020.

5. Vaghefi, K. R. C. Oats, D. K. Harris, T. M. Ahlborn, C. N. Brooks, K. A. Endsley, C. Roussi, R. Shuchman, J. W. Burns, and R. Dobson. Evaluation of Commercially Available Remote Sensors for Highway Bridge Conditional Assessment. *ASCE Journal of Bridge Engineering*, 2012. 17(6): 886–895.

6. Abu Dabous, S. S. Yaghi, S. Alkass, and O. Moselhi. Concrete Bridge Deck Condition Assessment Using IR Thermography and Ground Penetrating Radar Techniques. *Automation in Construction*, 2017. 81: 340–354.

7. Gee, K. W. and G. Henderson. *Highway Bridge Inspection*. U.S. Department of Transportation, Washington, D. C. Download Link. Accessed Aug. 28, 2020.

8. Phares, B. M. G. A. Washer, D. D. Rolander, B. A. Graybeal, M. Moore. Routine Highway Bridge Inspection Condition Documentation Accuracy and Reliability. *ASCE Journal of Bridge Engineering*, 2004. 9(4): 403–413.

9. M. J. Sprung, and M. Chambers. *Transportation Statistics Annual Report 2017*. U.S. Department of Transportation, Washington, D. C. https://www.bts.gov/archive/publications/transportation_statistics_annual_report/2017/index. Accessed Aug. 28, 2020.

10. Scott, M. J. J. C. Duke, N. Davidson, G. Washed, and R. Weyers. Automated Characterization of Bridge Deck Distress Using Pattern Recognition Analysis of Ground Penetrating Radar Data. *Materials Evaluation*, 2000. 58: 1305–1309.

11. Varnavina. A. V. *Non-Destructive and Destructive Bridge Deck Condition Assessment*. Missouri University of Science and Technology, Rolla, MO, 2015.

12. Bureau of Bridges and Structures. *Bridge Condition Report Procedures and Practices*. Illinois Department of Transportation, Springfield, IL. http://www.idot.illinois.gov/Assets/uploads/files/Doing-Business/Manuals-Guides-&Handbooks/Highways/Bridges/Planning/BCR%20Procedures%20and%20Practices%20.pdf. Accessed Aug. 28, 2020.

13. Vaghefi, K. T. M. Ahlborn, D. K. Harris, and C. N. Brooks. Combined Imaging Technologies for Concrete Bridge Deck Condition Assessment. *ASCE Journal of Performance of Constructed Facilities*, 2015. 29(4): 04014102.

14. Moore, M. B. Phares, B. Graybeal, D. Rolander, and G. Washer. *Reliability of Visual Inspection for Highway Bridges, Volume 1: Final Report*. FHWA-RD-01-020. FHWA, U.S. Department of Transportation, 2001.

15. Zhang, S. C. D. Lippitt, S. M. Bogus, and P. R. H. Neville. Characterizing Pavement Surface Distress Conditions with Hyper-spatial Resolution Natural Color Aerial Photography. *Remote Sensing*, 2016. 8(5): 392.

16. Chen, S. C. Rice, C. Boyle, and E. Hauser. Small-Format Aerial Photography for Highway-Bridge Monitoring. *ASCE Journal of Performance of Constructed Facilities*, 2011. 25(2): 105–112.

17. Yuan, X. J. Fu, H. Sun, and C. Toth. The Application of GPS Precise Point Positioning Technology in Aerial Triangulation. *ISPRS Journal of Photogrammetry and Remote Sensing*, 2009. 64: 541–550.

18. Zhang, Y. J. Xiong, and L. Hao. Photogrammetric Processing of Low-Altitude Images Acquired by Unpiloted Aerial Vehicles. *The Photogrammetric Record*, 2011. 26(134): 190–211.

19. Blaschke, T. Object Based Image Analysis for Remote Sensing. *ISPRS Journal of Photogrammetry and Remote Sensing*, 2010. 65: 2–16.

20. Blaschke, T. G. J. Hay, M. Kelly, S. Lang, P. Hofmann, E. Addink, R. Q. Feitosa, F. van der Meer, H. van der Werff, F. van Coillie, and D. Tiede. Geographic Object-Based Image Analysis – Towards a New Paradigm. *ISPRS Journal of Photogrammetry and Remote Sensing*, 2014. 87: 180–191.

21. Vaghefi, K. H. A. de Melo e Silva, D. K. Harris, and T. M. Ahlborn. Application of Thermal IR Imagery for Concrete Bridge Inspection. *Proceedings of the PCI Convention and National Bridge Conference*, Salt Lake City, UT, 2011.

22. Morgan, D. and E. Falkner. *Aerial Mapping: Methods and Applications, 2nd edition*. CRC Press, Boca Raton, FL, 2001.

23. Jensen, J. *Remote Sensing of the Environment: An Earth Resource Perspective, 2nd edition.* Pearson, Upper Saddle River, NJ, 2006.

24. Kaundinya, S. E. Arnold, F. Rodriguez-Morales, and A. Patil. A UAS-Based Ultra-Wideband Radar System for Soil Moisture Measurements. *Proceedings of the 2018 IEEE Radar Conference*, Oklahoma City, OK, 2018.

25. American Society for Testing and Materials. *Standard Test Method for Detecting Delaminations in Bridge Decks Using Infrared Thermography*. ASTM D4788-03. ASTM, West Conshohocken, PA, 2007.

26. Hughes, A. E. Teuten, T. Starnes, N. Cowie, T. Swinfield, R. Humpidge, J. Williams, D. Bridge, C. Casey, A. Asque, and D. Morris. *Drones for GIS – Best Practices*. Conservation Data Management Unit, Royal Society for Protection of Birds, Sandy, UK, 2018.

27. Washer, G. A. R. Fenwick, and N. Bolleni. *Development of Hand-Held Thermographic Inspection Technologies*. NUTC R198. Center for Transportation Infrastructure and Safety, Missouri University of Science and Technology, Rolla, MO, 2009.

28. Clark, M. R. D. M. McCann, and M. C. Forde. Application of Infrared Thermography to the Non-Destructive Testing of Concrete and Masonry Bridges. *NDT&E International*, 2003. 36: 265–275.

29. Carrivick, J. L. M. W. Smith, D. J. Quincey. *Structure from Motion in the Geosciences: New Analytical Methods in Earth and Environmental Science*. Wiley-Blackwell, Hoboken, NJ, 2016.

30. Agisoft Forum. *Algorithms Used in Photoscan*. Agisoft LLC. https://www.agisoft.com/forum/index.php?topic=89.0. Accessed Aug. 31, 2020.

31. Lowe, D. G. Distinctive Image Features from Scale-Invariant Keypoints. *International Journal of Computer Vision*, 2004. 60: 91–110.

32. Granshaw, S. I. Bundle Adjustment Methods in Engineering Photogrammetry. *The Photogrammetric Record*, 1980. 10(56): 181–207.

33. Szeliski, R. *Computer Vision Algorithms and Applications*. Springer, London, NY, 2011.

34. Seitz, S. M. B. Curless, J. Diebel, D. Scharstein, and R. Szeliski. A Comparison and Evaluation of Multi-View Stereo Reconstruction Algorithms. *Proceedings of the 2006 IEEE Computer Society Conference on Computer Vision and Pattern Recognition*, New York, NY, 2006.

35. Furukawa, Y. B. Curless, S. M. Seitz, and R. Szeliski. Towards Internet-Scale Multi-View Stereo. *Proceedings of the 2010 IEEE Computer Society Conference on Computer Vision and Pattern Recognition*, San Francisco, CA, 2010.

36. Arnold, T. B. and J. W. Emerson. Nonparametric Goodness-of-Fit Tests for Discrete Null Distributions. *The R Journal*, 2011. 3(2): 34–39.

APPENDIX A: S-UAS BASED AIRBORNE IMAGING AND ANALYSIS SYSTEM GUIDEBOOK

This guidebook has been developed to assist transportation management agencies with professional training and education and workforce development. This guidebook provides detailed instructions on how to use the identified small-unmanned aircraft system (S-UAS), real time kinematics (RTK) system, and developed ArcGIS compatible analysis tools to detect the distresses of the wearing surface of a bridge deck and the distresses of the subsurface of a bridge deck.

Part A. S-UAS Operation

1. The selected S-UAS is DJI Mavic 2 Pro. Detailed specifications regarding this S-UAS can be found at https://www.dji.com/mavic-2/info.

2. The Quick Start Guide of the selected S-UAS (DJI Mavic 2 Pro) can be found at https://dl.djicdn.com/downloads/Mavic_2/20180823/Mavic_2_Pro_Quick_Start_Guide_EN.pdf.

3. Prior to heading out into the field, make sure the controller and all batteries are fully charged. Depending on the size of the study site, various amounts of batteries are needed. In general, four batteries are recommended, which can provide a total flight duration of two hours. This setup can cover almost any bridges across the State of New Mexico. Press the power button on the controller once to make sure it is fully charged. Similarly, press the power button once on the batteries to ensure they are fully charged. In addition, make sure the Micro SD card has been inserted. It is also suggested to obtain two sets of S-UAS as a backup. Additionally, the data collection crew should develop a checklist to ensure all equipment and accessories are ready for data collection.

4. In the field, make sure there is on obstacles for flight. Additionally, make sure the weather is preferable for flight, and the wind speed is less than 15 miles per hour. In the field, insert one battery into DJI Mavic 2 Pro's battery bay and slide the battery forward until it clicks into place.

5. Hold on the power button until you see the controller startup screen to power on the controller. You should feel a vibration from the controller to indicate the power is on.

6. Turn on the DJI by holding the battery power button. When DJI Mavic 2 Pro powers on, the battery displays and LED animation and you hear the startup tone.

7. Connect your smartphone or tablet to the controller via a USB cable provided by DJI. This will connect your smartphone or tablet to DJI Mavic 2 Pro. You can check the connection via the DJI Go mobile app or the Map Pilot mobile app.

8. Upload the flight plan onto DJI Mavic 2 Pro. Detailed information about how to design and upload a flight plan onto DJI Mavic 2 Pro will be provided in the next section. At the completion of flight plan uploading, your smartphone or tablet should pop up a message to indicate plan has been completely uploaded to DJI Mavic 2 Pro (100%).

9. Click on the Start button next to Upload button to start the designed mission. DJI Mavic 2 Pro should automatically take off and flying to the data collection area.

10. Once the mission is completed, turn off DJI Mavic 2 Pro by pressing the battery power button and turn off the controller by pressing the power button.

11. Copy the collected images to a laptop for imagery backup.

Part B. S-UAS Flight Plan

The selected mobile app for DJI Mavic 2 Pro flight design and upload is Map Pilot by Drones Made Easy. It costs $9.99 to purchase a license. There are other options for S-UAS flight plan design and upload, such as 3DSurvey Pilot or DroneDeploy. They are free mobile apps but they may have operation limitations.

1. The Quick Start guide of Map Pilot can be found at https://support.dronesmadeeasy.com/hc/en-us/articles/206019863-Quick-Start-A-Start-to-Finish-Guide.

2. Download and install Map Pilot onto your smartphone or tablet. It should be noted that this mobile app only works with iOS.

3. Start Map Pilot by taping it on your smartphone and tablet.

4. Tap on Create New Mission.

Figure A1. The main user interface of Map Pilot.

5. The following window should show up. Tap on OK.

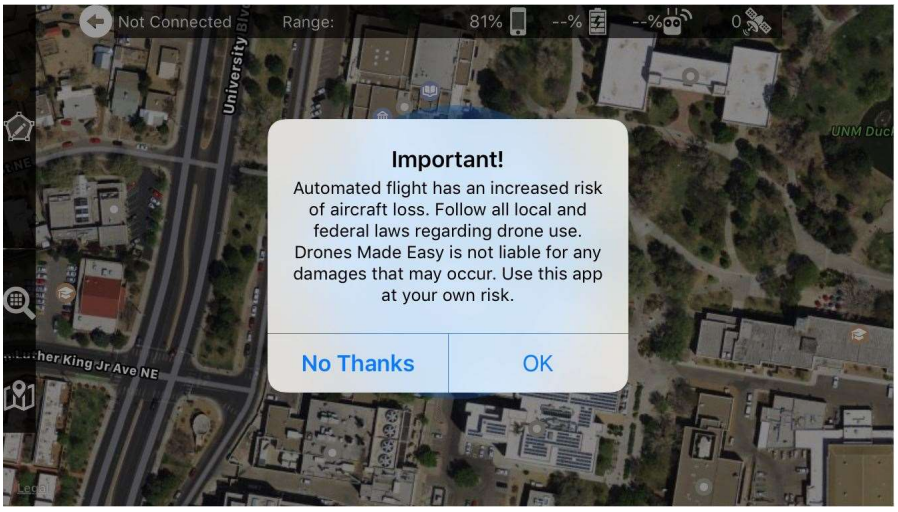

Figure A2. The user interface after taping Create New Mission.

6. Browse the base map to the area of interest (AOI). It should be noted that if you are designing the flight plan in the field, make sure you have cellular connection to download the base maps. If you are designed the flight plan in your office, make sure you have either cellular or Wi-Fi connection to download the base maps.

7. Click the first three corners of your AOI and then drag the last corner point of your AOI to create a rectangular bounding box. Subsequently, double click at any location to create another point as your take-off and landing point. As it shows in the following screen capture, the purple solid point indicates the take-off and landing point, the green solid dot indicates the start point of data collection, and the red solid dot indicates the end point of data collection.

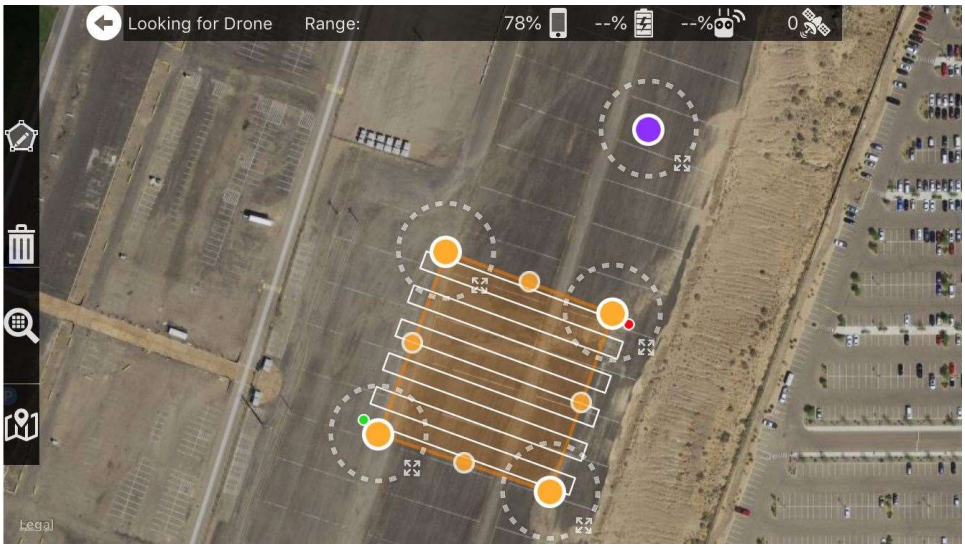

Figure A3. The user interface for designing flight plans.

8. Decide what forward overlap and sidelap for data collection and assigning the overlap by clicking the black strip on the top the user interface. It is suggested using 80% for forward overlap and 75% for sidelap.

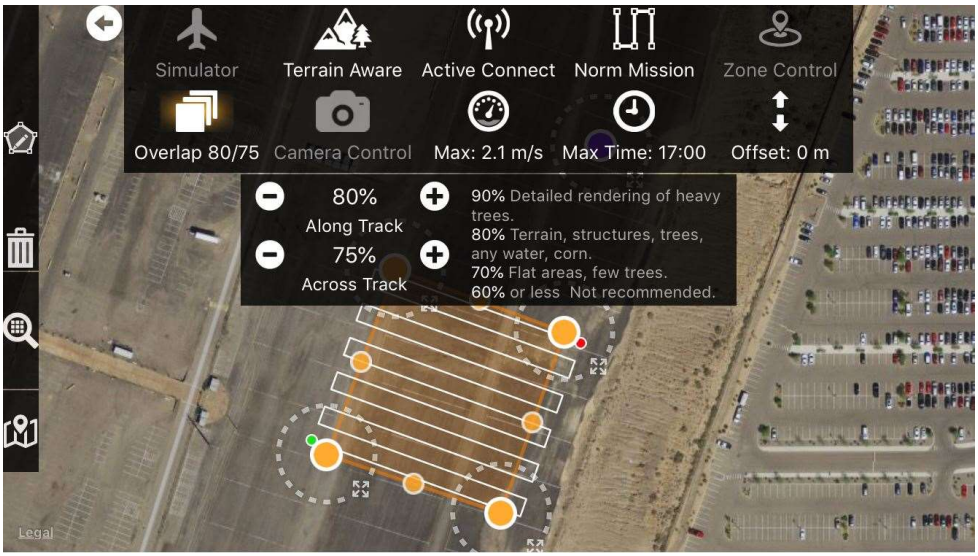

Figure A4. The user interface of changing overlap settings.

9. Tap on the magnifier button under the trash can button to change the flight altitude. It is suggested to collect sub-centimeter spatial resolution aerial images. For example, the study used 0.5 cm as the resolution, which has a flight altitude of 23 m.

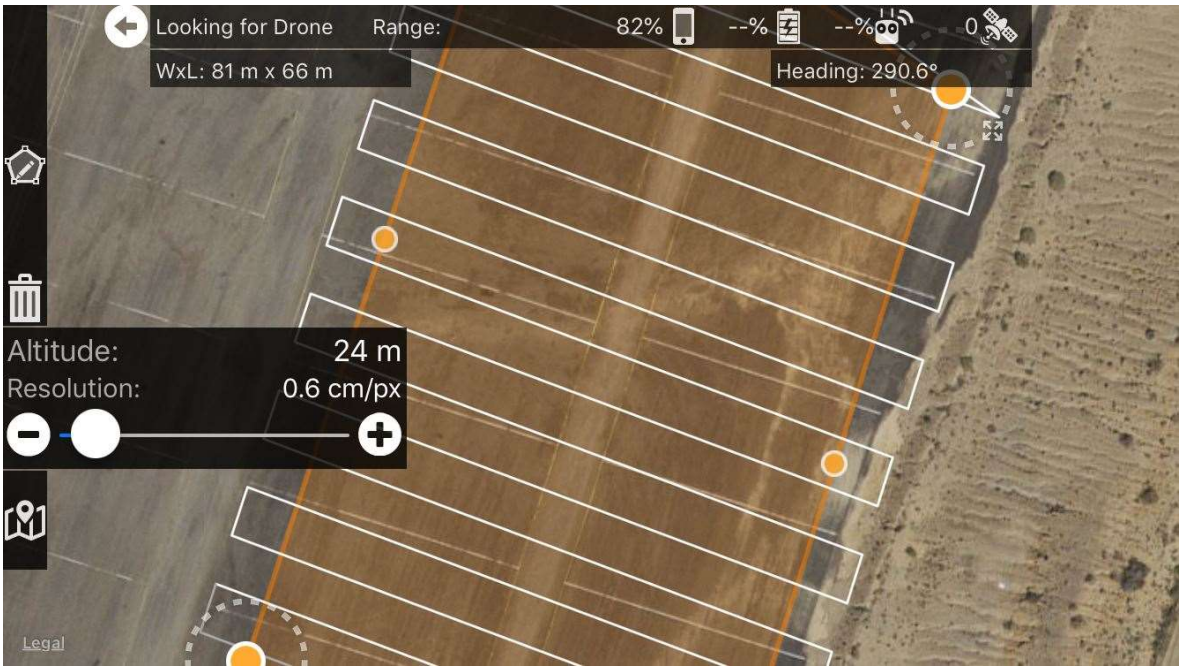

Figure A5. The user interface of changing altitude settings.

10. Tap on the pentagon button above the trash can button to see flight statistics include duration, batteries, images, points, and storage.

Figure A6. The user interface of displaying flight statistics.

11. Connect DJI Mavic 2 Pro to the app. Users only need to power on the drone and the controller. The app will automatically connect to the drone.

12. Once connected, tap on the aircraft icon on the right-hand side of the app.

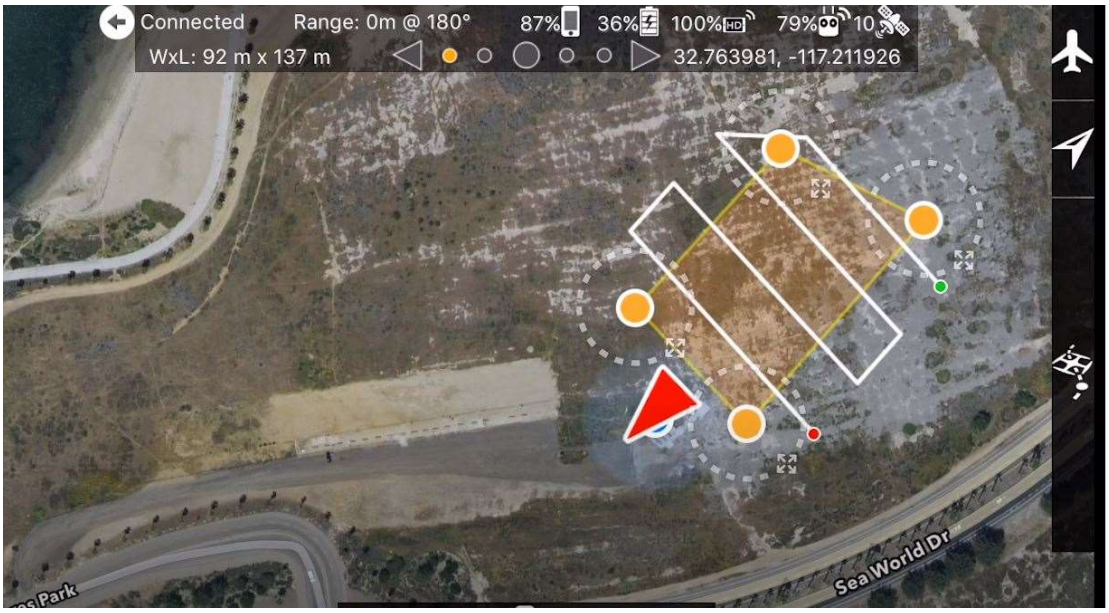

Figure A7. The user interface prior to uploading a flight plan.

13. Once the slide bar appears, tap on the Upload button to upload the flight plan, and then tap on Start to start data collection. If an emergency occurs during flight, tap on Home or Stop button to adjourn data collection.

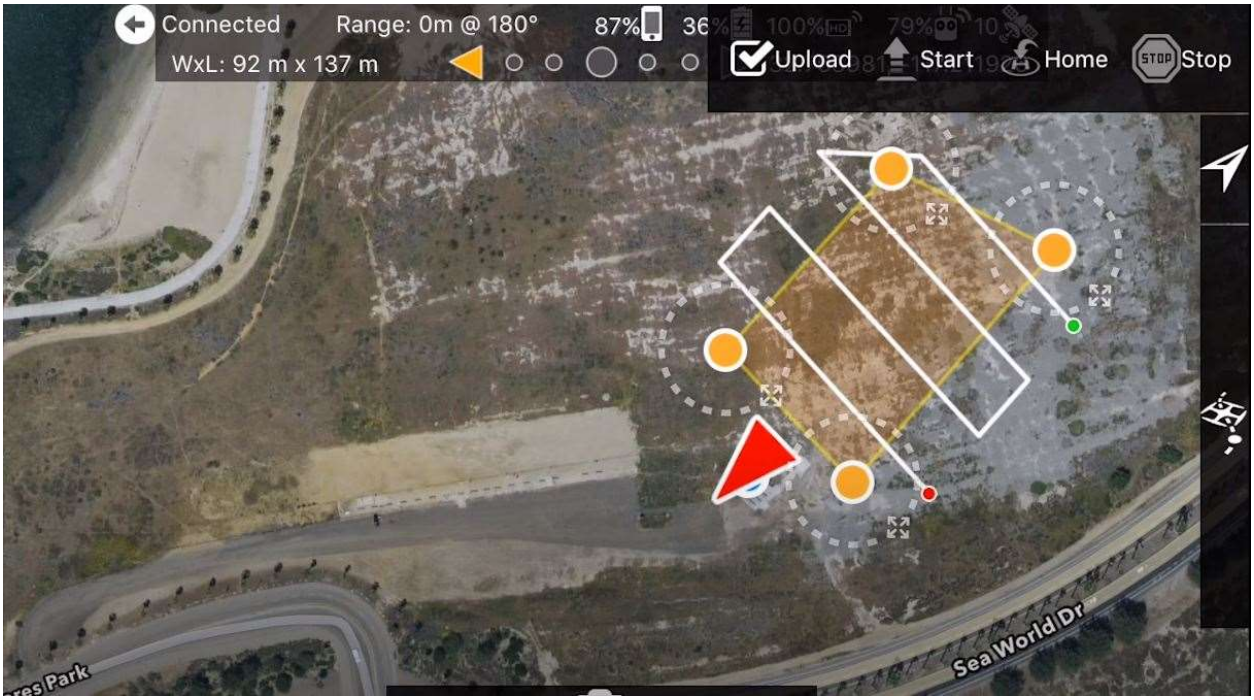

Figure A8. The user interface of uploading a flight plan.

Part C. RTK System Operation

The Emlid Reach RS2 system was selected as the RTK system for ground control points (GCPs) data collection. The complete system costs approximately $4,000. The software for post-processing is EZSurv by developed by Effigis. The software package costs approximately $1,600.

1. Make sure all batteries are fully charged before field trips.

2. First setup can be found at https://docs.emlid.com/reachrs2/common/quickstart/first-setup/.

3. Base and Rover setup can be found at https://docs.emlid.com/reachrs2/common/quickstart/base-rover-setup/.

4. It should be noted that users need to user their smartphone or tablet as the data collection controller. It should also be noted that users need to measure the distance from the benchmark to the base antenna, and they need to measure the distance from the spike of survey pole to the rover antenna as well.

5. The ReachView mobile app will be used as the data collection controller software. It is free and users can download them from Apple Store or Google Play. The instruction on how to use this mobile app can be found at https://docs.emlid.com/reachrs2/common/reachview/.

6. In the field, users need to place the base first. The detailed process for base setup in the field can be found at https://docs.emlid.com/reachrs2/common/tutorials/placing-the-base/.

7. In the field, users need to collect GCPs in RTK mode. The detailed process for RTK mode setup and data collection can be found at https://docs.emlid.com/reachrs2/common/tutorials/placing-gcps/.

8. When data collection is completed, users need to transfer the data to a desktop computer.

9. Start the EZSurv software and follow the steps to post process the GCPs. Processing steps can be found at http://www.onpoz.com/Support/KBData/KbDisplayPage.aspx.

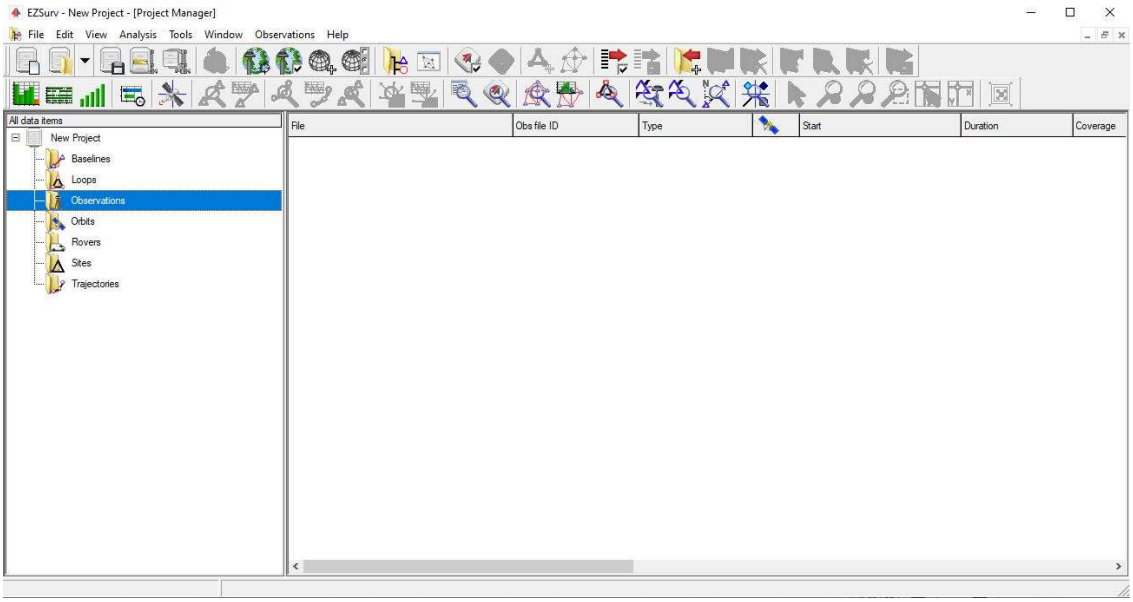

Figure A9. The user interface of the EZSurv software.

Part D. Structure from Motion Operation

The selected software for Structure from Motion (SfM) is Agisoft Metashape. This software packages costs approximately $3,499. The education license costs approximately $549.

1. The complete tutorial for the beginner level for Agisoft Metashape can be found by clicking this link https://www.agisoft.com/support/tutorials/beginner-level/.

2. Add Photos, browser to the folder that contains all aerial phots.

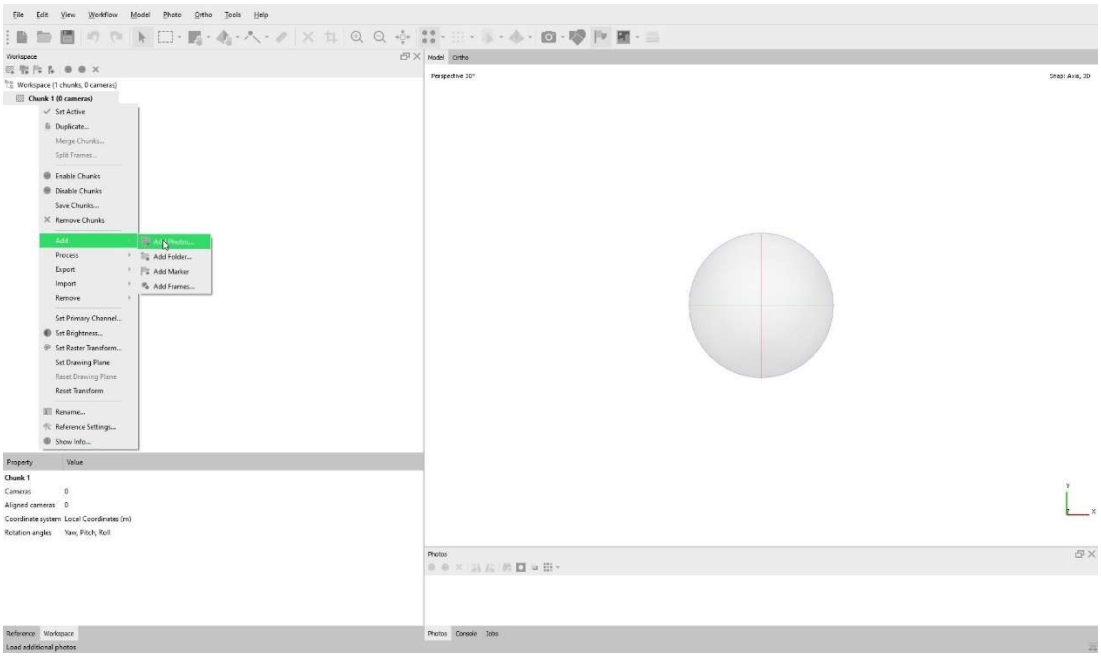

Figure A10. The user interface of adding photos.

3. Align Photos, parameter values see the figure below.

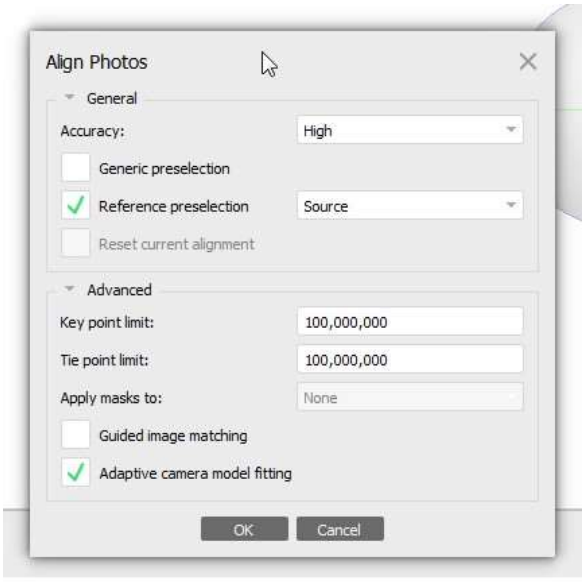

Figure A11. The user interface of aligning photos.

4. Build mesh from sparse point cloud, parameter values see the figure below.

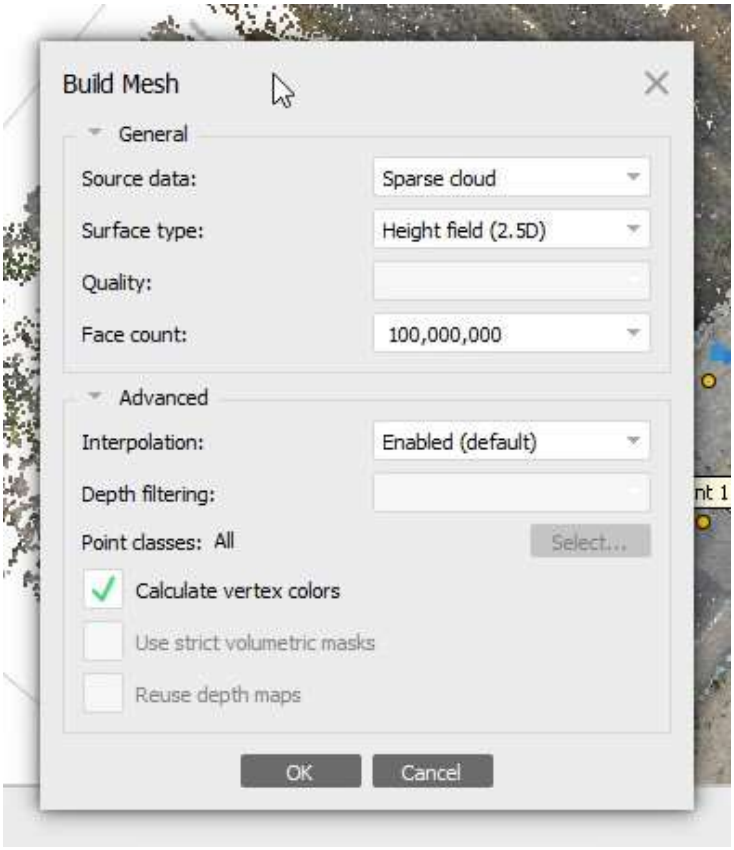

Figure A12. The user interface of building mesh.

5. Place markers for ground control points. Place makers on photos that contain most of the markers. Point names will be point 1, point 2, point 3, and to the last point.

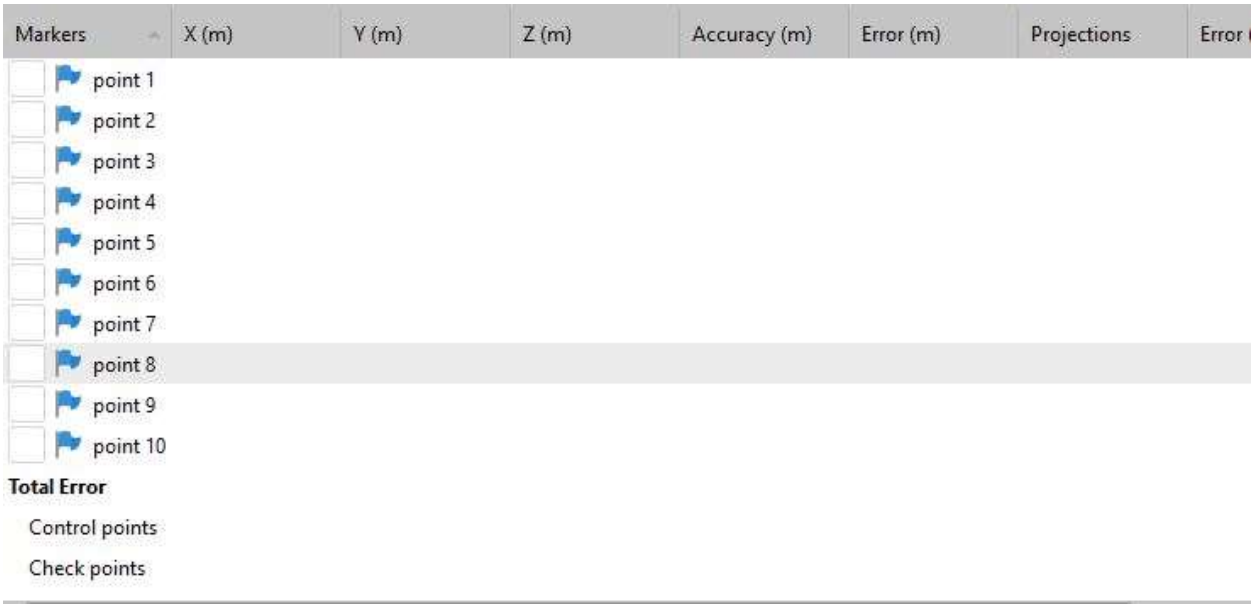

Figure A13. The user interface of placing markers.

6. Change reference settings. Camera coordinate systems and marker coordinate systems. Parameter values see the figure below.

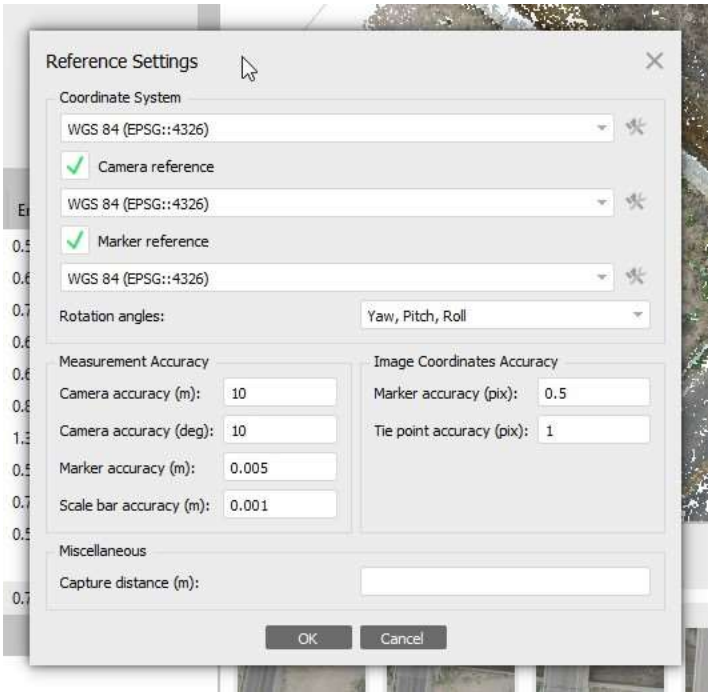

Figure A14. The user interface of changing reference settings.

7. Import reference from the post-processed GCP survey file.

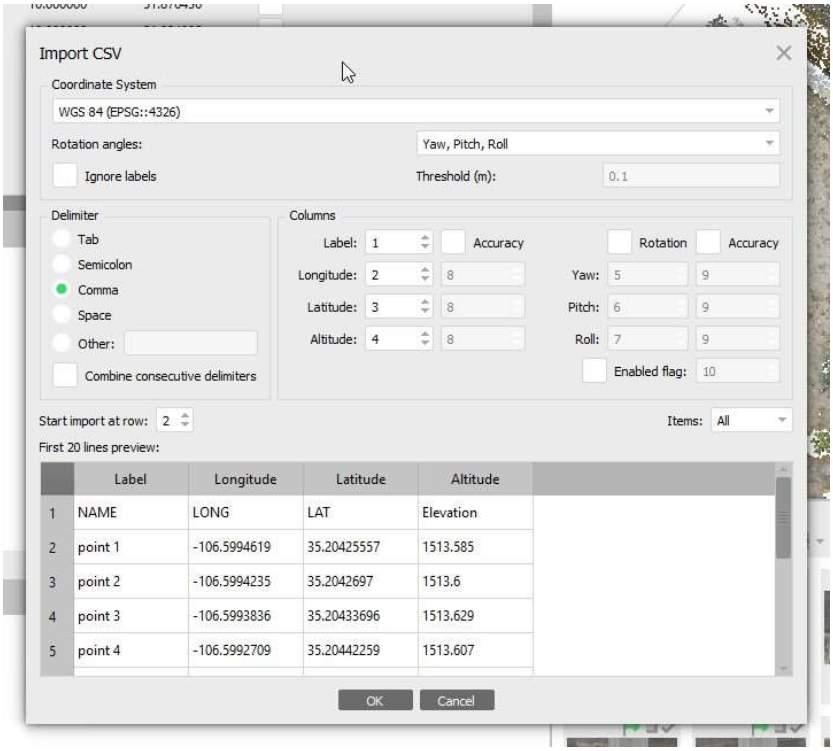

Figure A15. The user interface of importing CSV.

8. Uncheck all photos and check on the markers to be used in optimization.

Cameras	Longitude	Latitude	Altitude (m)
DJI_01...	-106.599422	35.204187	1485.050000
DJI_01...	-106.599392	35.204221	1485.050000
DJI_01...	-106.599357	35.204259	1485.150000
DJI_01...	-106.599325	35.204293	1485.150000
DJI_01...	-106.599290	35.204331	1485.150000
DJI_01...	-106.599258	35.204364	1485.150000
DJI_01...	-106.599225	35.204400	1485.150000
DJI_01...	-106.599192	35.204436	1485.150000
DJI_01...	-106.599254	35.204446	1485.150000
DJI_01...	-106.599287	35.204410	1485.250000
DJI_01...	-106.599319	35.204375	1485.250000

Markers	Longitude	Latitude	Altitude (m)
point 1	-106.599462	35.204256	1513.585000
point 2	-106.599424	35.204270	1513.600000
point 3	-106.599384	35.204337	1513.629000
point 4	-106.599271	35.204423	1513.607000
point 5	-106.599255	35.204388	1513.853000
point 6	-106.599411	35.204239	1513.724000
point 7	-106.599290	35.204441	1513.570000
point 8	-106.599361	35.204361	1513.618000
point 9	-106.599458	35.204303	1513.567000
point 10	-106.599488	35.204254	1513.586000

Total Error

Figure A16. The user interface of unlocking all photos and checking on the makers.

9. Optimize camera alignment.

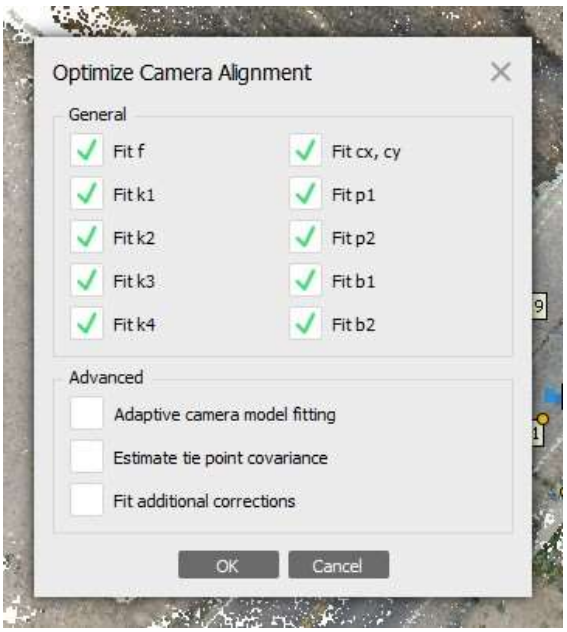

Figure A17. The user interface of optimizing camera alignment.

10. Optimized results check.

Markers	Longitude	Latitude	Altitude (m)	Accuracy (m)	Error (m)	Projections	Error (pix)
point 1	-106.599462	35.204256	1513.585000	0.005000	0.196675	36	0.595
point 2	-106.599424	35.204270	1513.600000	0.005000	0.169383	38	0.689
point 3	-106.599384	35.204337	1513.629000	0.005000	0.137416	43	0.743
point 4	-106.599271	35.204423	1513.607000	0.005000	0.115837	29	0.697
point 5	-106.599255	35.204388	1513.853000	0.005000	0.110486	29	0.658
point 6	-106.599411	35.204239	1513.724000	0.005000	0.111172	31	0.886
point 7	-106.599290	35.204441	1513.570000	0.005000	0.181762	34	1.350
point 8	-106.599361	35.204361	1513.618000	0.005000	0.157305	42	0.596
point 9	-106.599458	35.204303	1513.567000	0.005000	0.160536	40	0.753
point 10	-106.599488	35.204254	1513.586000	0.005000	0.119948	34	0.595
Total Error							
Control points					0.149057		0.781

Figure A18. The user interface of optimized results.

11. Build dense point cloud.

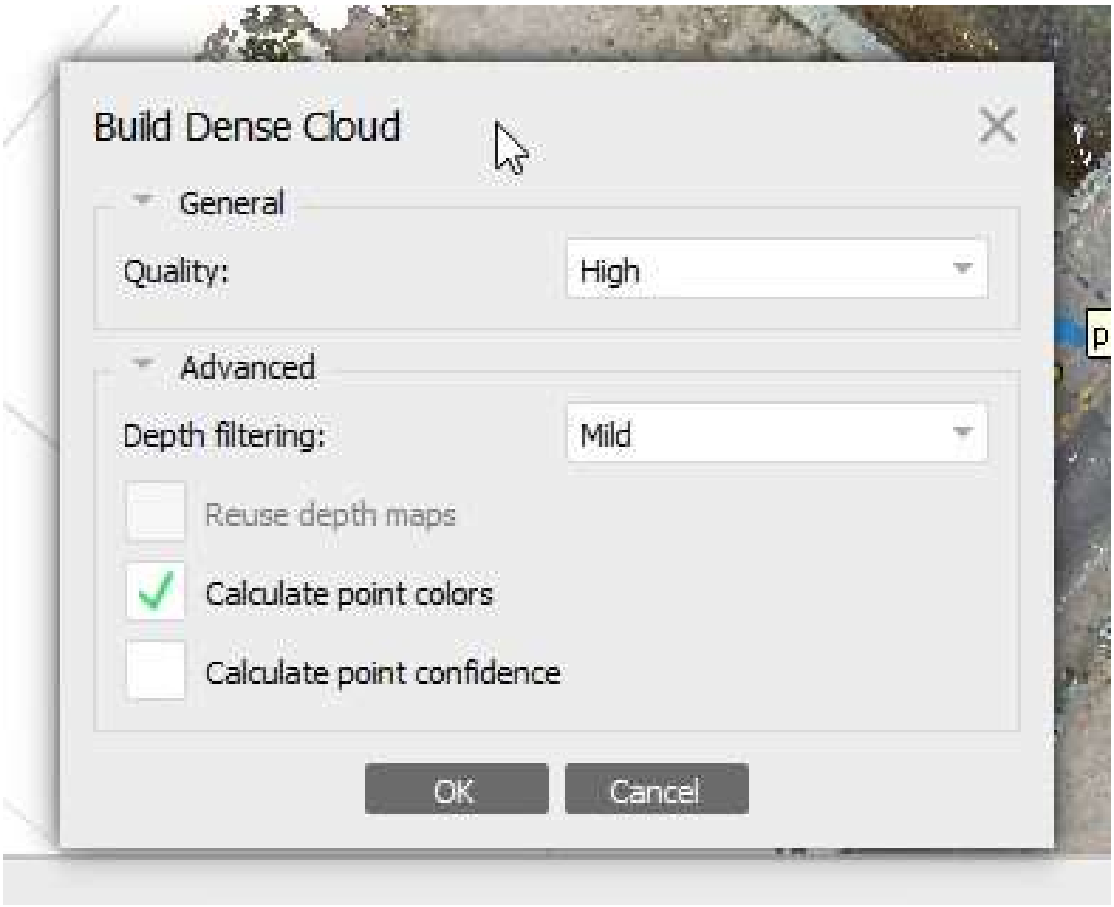

Figure A19. The user interface of building dense point cloud.

12. Build mesh from dense point cloud.

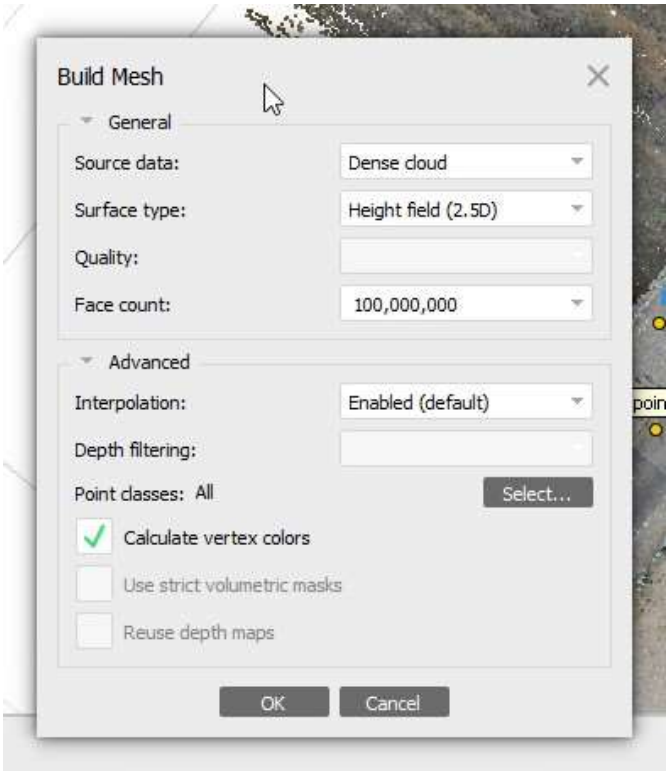

Figure A20. The user interface of building mesh from dense point cloud.

13. Build texture.

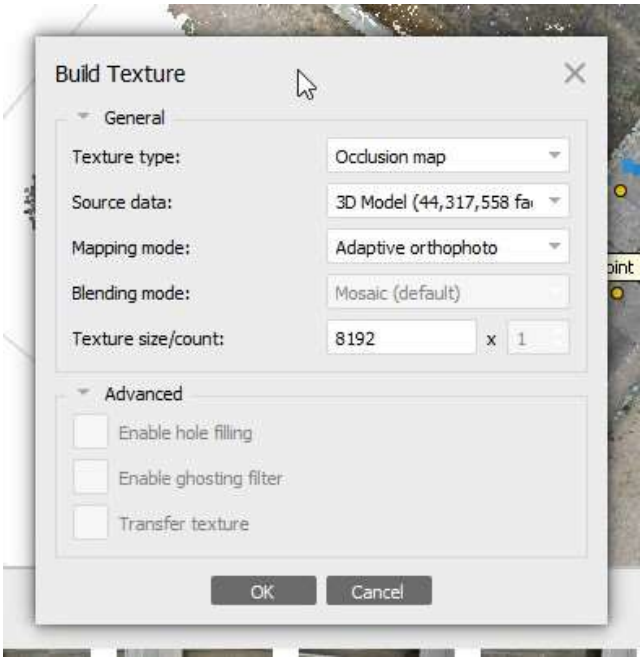

Figure A21. The user interface of building texture.

14. Build DEM

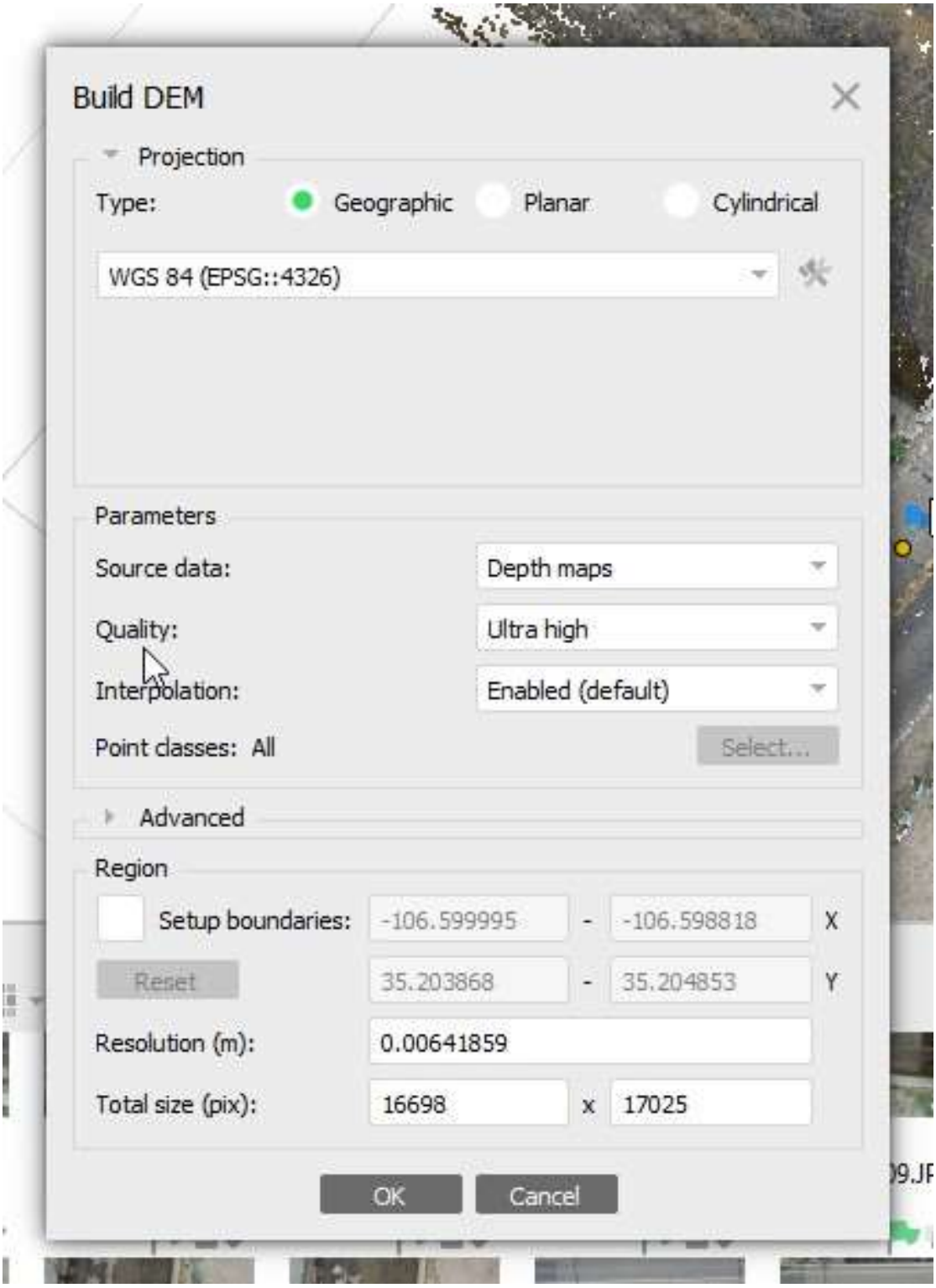

Figure A22. The user interface of building DEM.

15. Build Orthomosaic

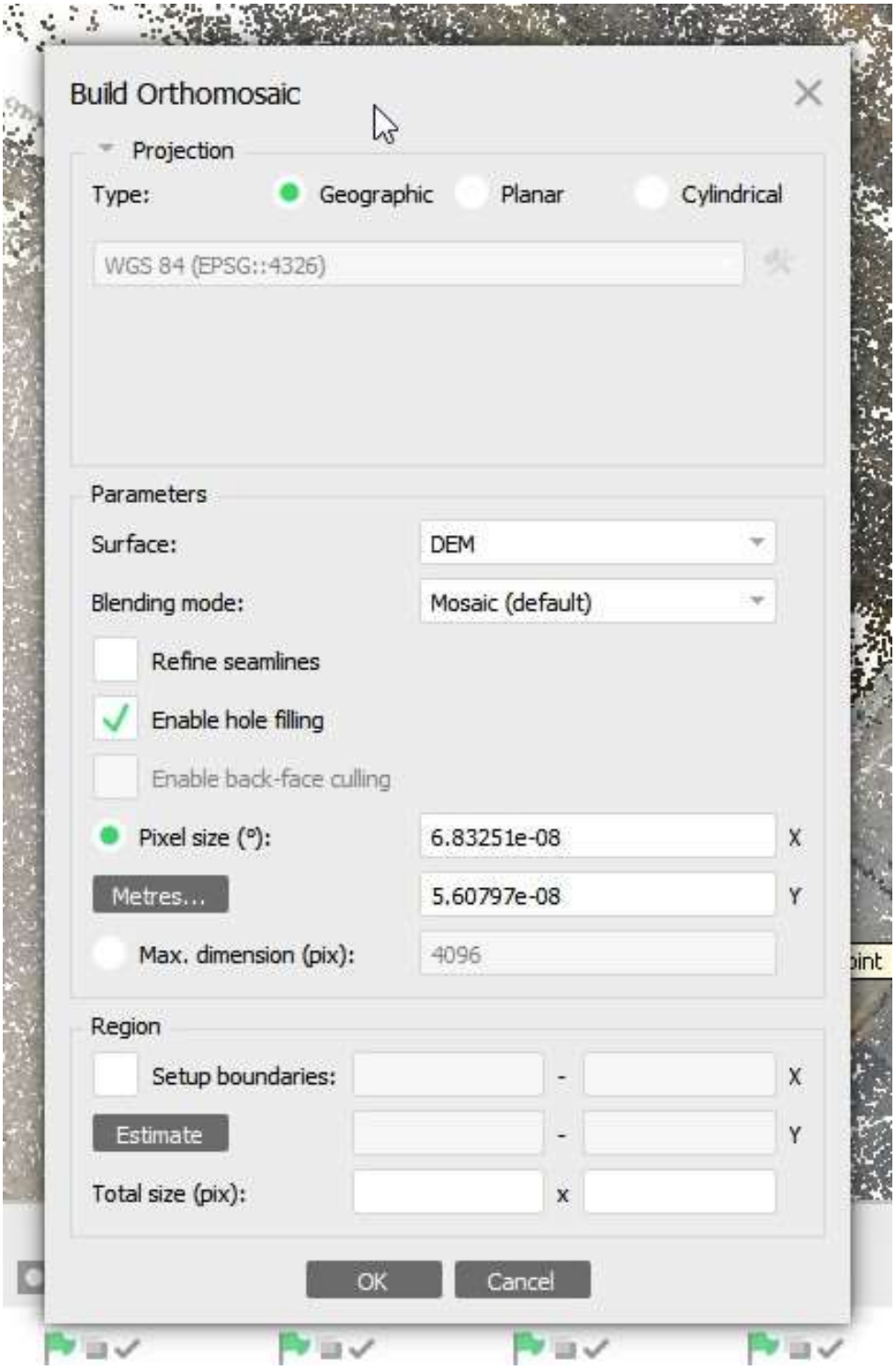

Figure A23. The user interface of building orthomosaic.

16. Export DEM

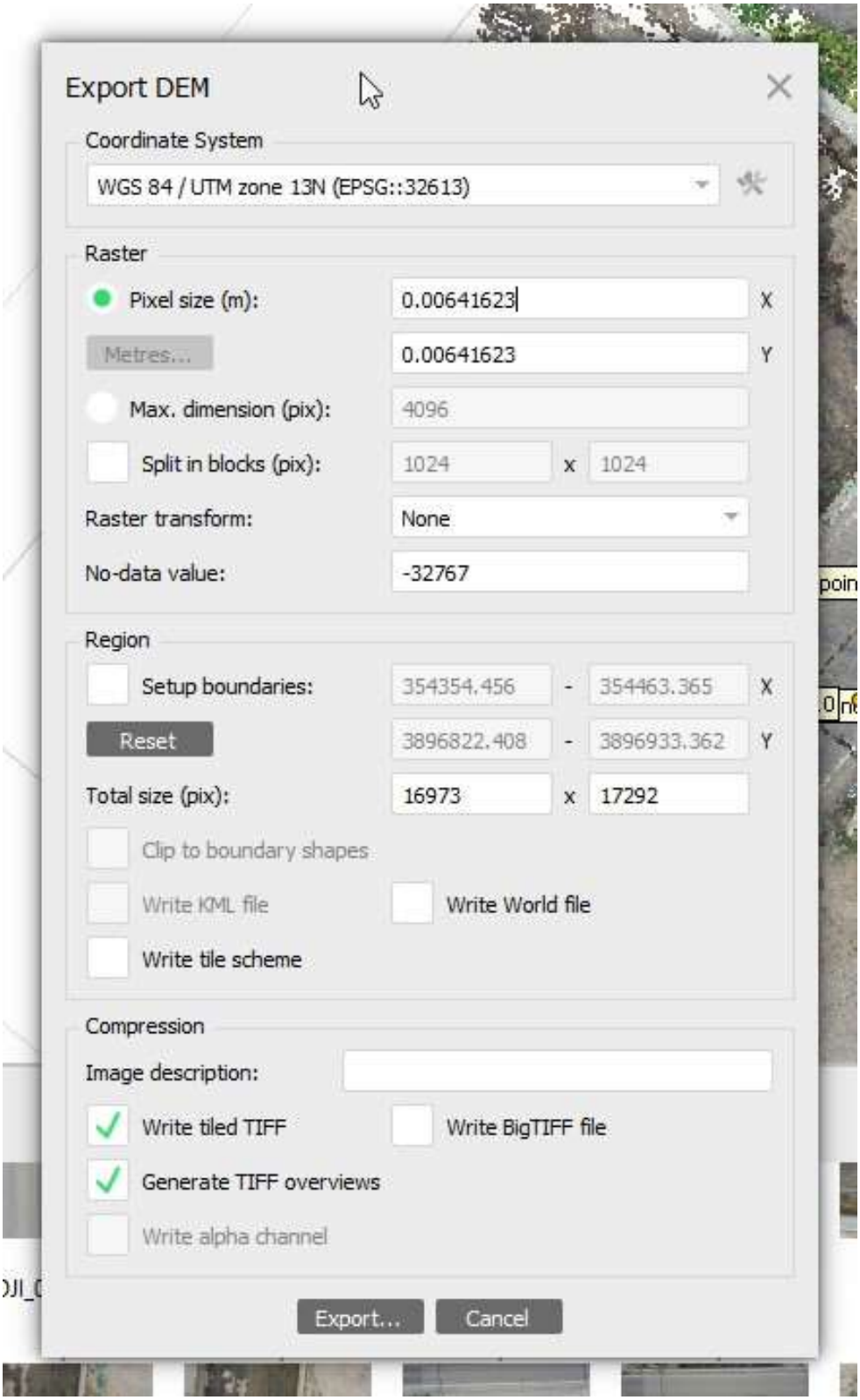

Figure A24. The user interface of exporting DEM.

17. Export Orthomosaic

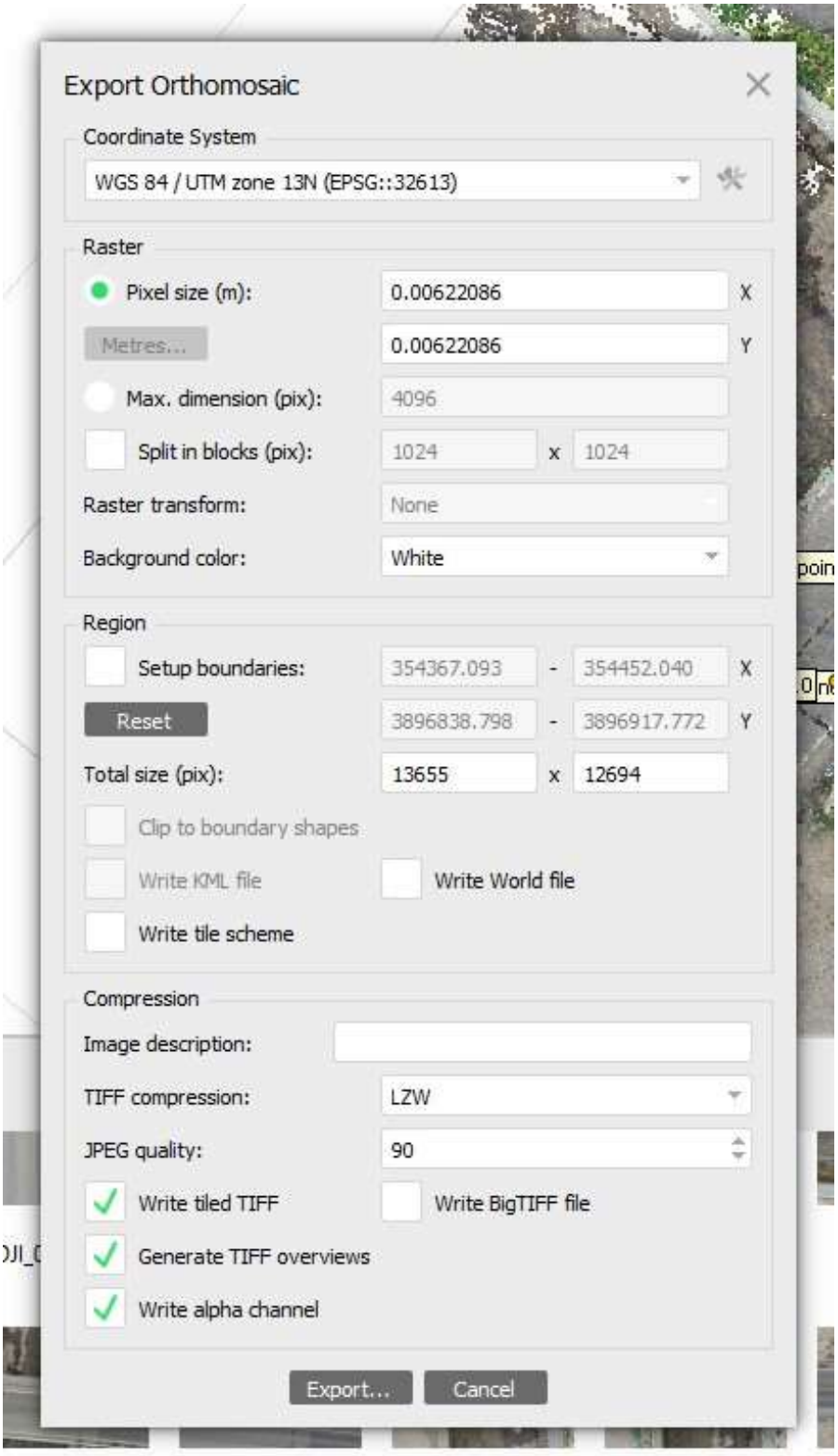

Figure A25. The user interface of exporting orthomosaic.

Part D. Analysis Tool Operation

The analysis toolset was developed in the Python programming language. It is compatible with ArcGIS ArcMap software and users with intermediate level GIS skills should be able to use it without any issues.

1. Download the toolset from this link. https://github.com/edac/BridgeInspectionToolbox.

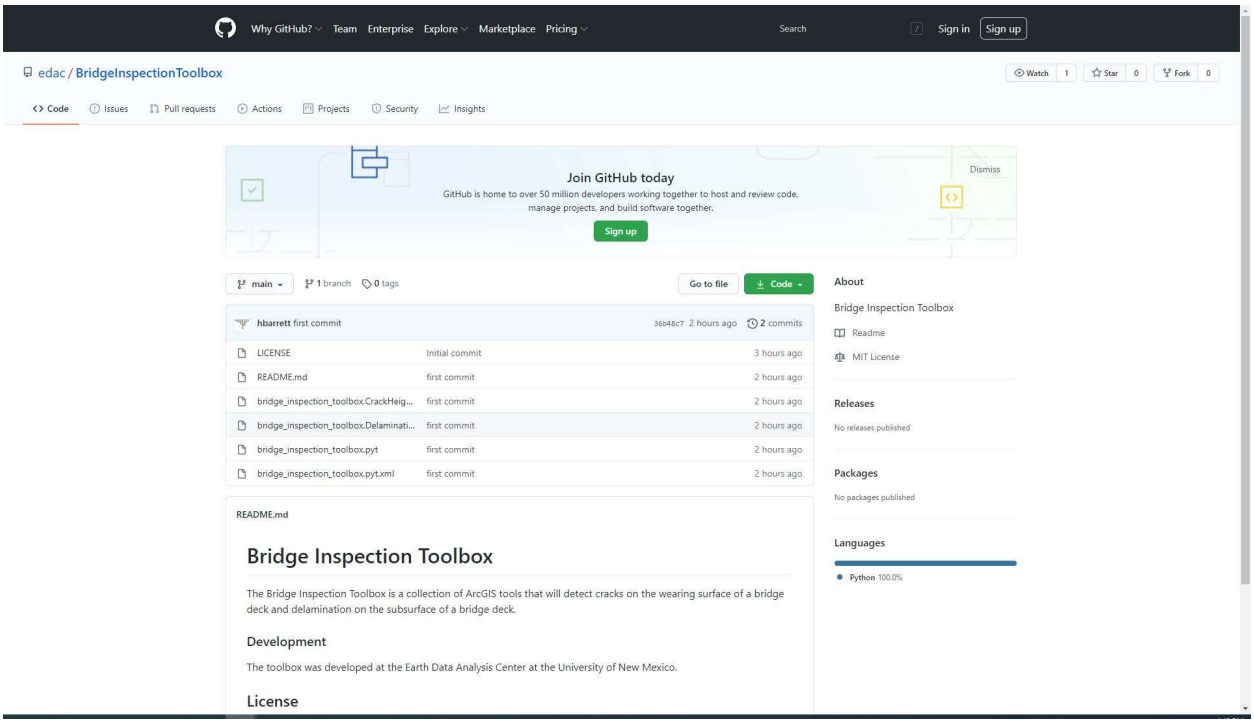

Figure A26. The user interface of the GitHub page.

2. Click on the “Code” button. The following dialog will pop up.

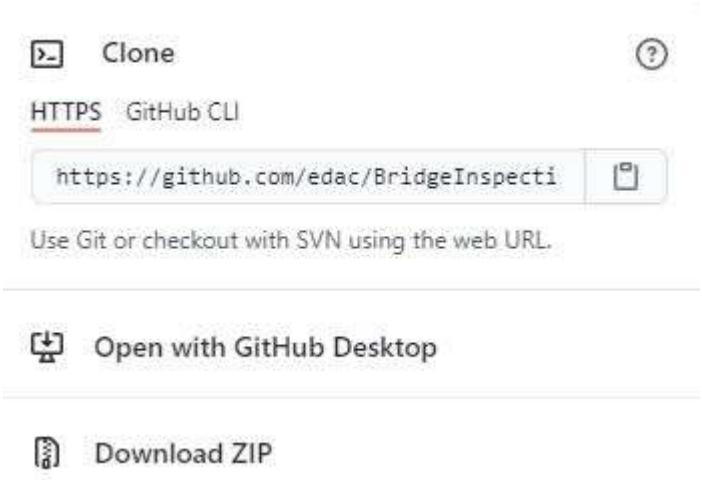

Figure A27. The user interface of the downloading process.

3. Click on Download ZIP. The download will start in a few seconds.

4. Users can find the toolset is compressed in a zip file once the download completed.

5. Unzip the downloaded toolset.

6. Open ArcMap 10.3.1 or newer version.

7. The ArcMap user interface looks like below.

8. In the Standard Toolbar, click on the ArcToolbox button below (the icon with the red box).

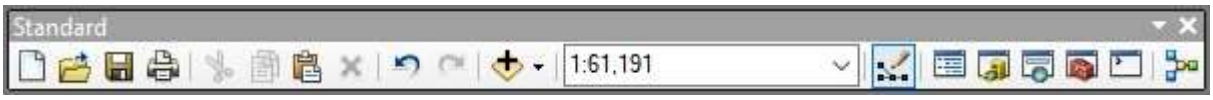

Figure A28. The standard toolbar of ArcMap.

9. The ArcToolbox dialog will open.

Figure A29. The ArcToolbox dialog.

10. Right-click on any blank space in the ArcToolbox, and then the Add Toolbox button will show up.

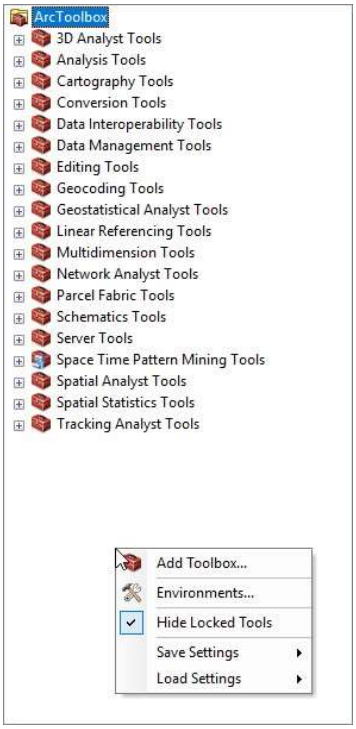

Figure A30. The user interface of Adding Toolbox.

11. Click on the Add Toolbox button.

12. Browse to the folder where the bridge toolset was saved.

13. Select the Bridge toolbox and then click on Open. The toolset will be added to the ArcToolbox.

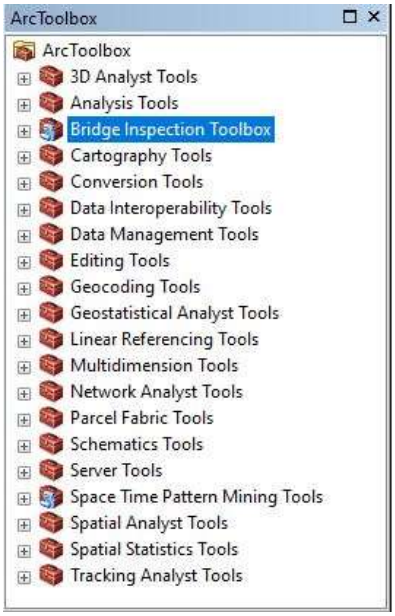

Figure A31. The inserted Bridge Inspection Toolbox.

14. Click on the plus sign next the Bridge Toolbox. The two tools associated with this toolset will show up.

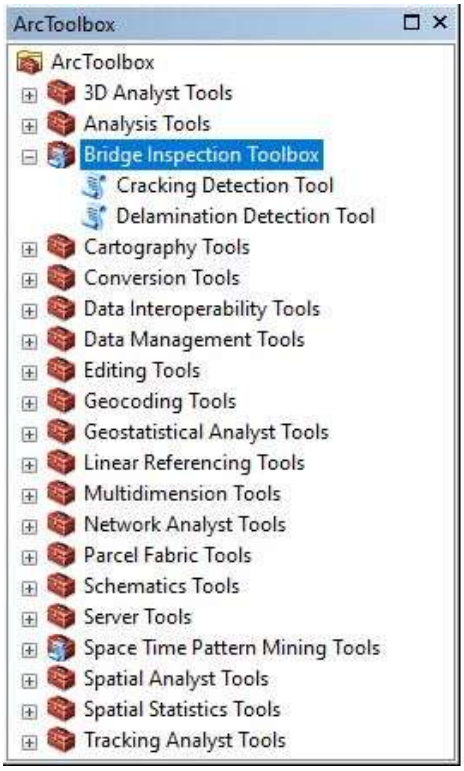

Figure A32. The two tools in the Bridge Inspection Toolbox.

15. Double-click on the Cracking Detection tool. The user interface looks as the following.

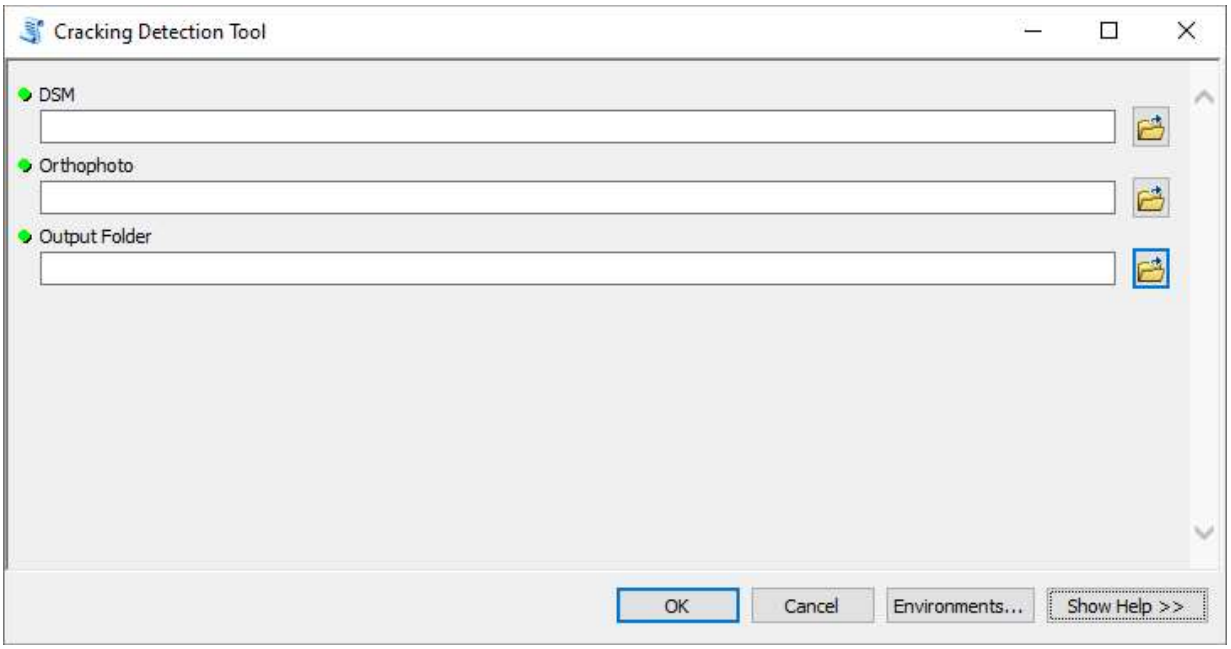

Figure A33. The user interface of the Cracking Detection Tool.

16. Double-click on the Delamination Detection tool. The user interface looks as the following.

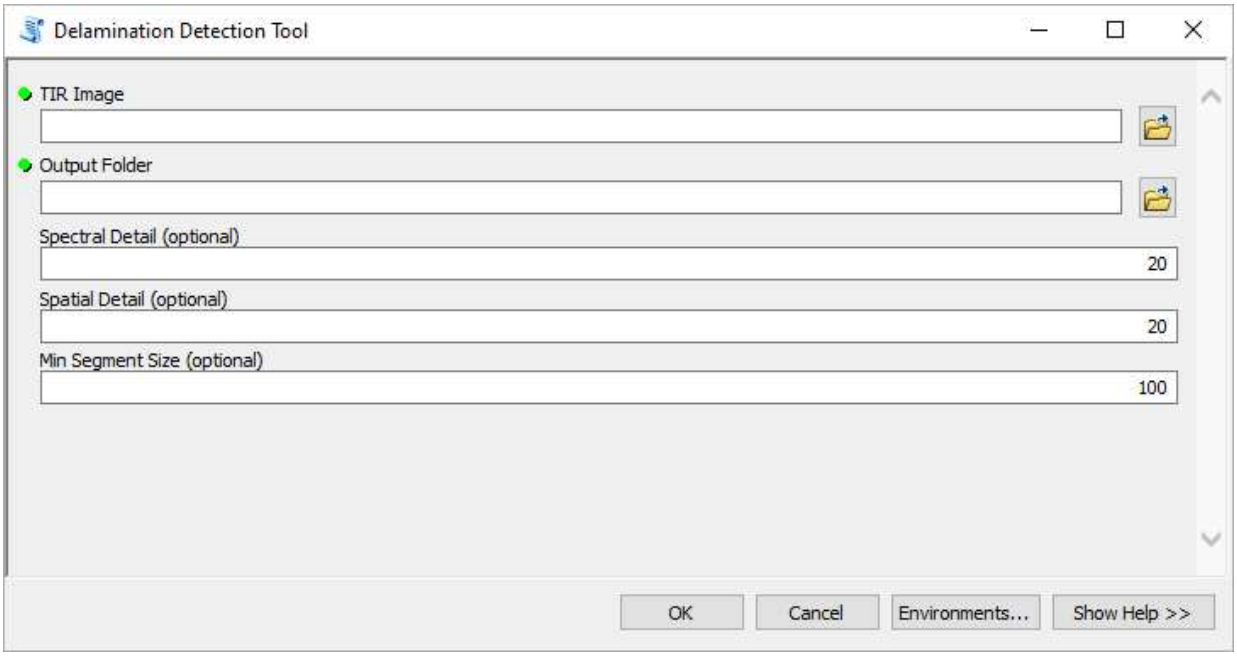

Figure A34. The user interface of the Delamination Detection Tool.

17. Users can click on the Hide Help to hide the tool instruction on the right column of the tools. Users can also click on the Show Help to display the tool instruction again.

18. For the Cracking Detection tool. Users can determine the input orthophoto and DSM and then the output location for the cracking enhancement image and cracking highlight image.

19. For the Delamination Detection tool. More parameters are involved. Users need to select the input thermal-infrared image and the output location of the detected delamination image. Additionally, users need to determine the following parameter values.

(1) Spectral Detail: during the image segmentation process, this sets the level importance given to the spectral differences of features in the imagery. A default value is set to 20 but valid values range from 1.0 to 20.0. A higher value is appropriate when the features are spectrally similar. Smaller values create smoother outputs. If the output does not identify enough features, then raise the value. If it identifies too many features then lower the value.

(2) Spatial Detail: during the image segmentation process, this sets the level importance given to the spatial differences of features in the imagery. A default value is set to 20 but valid values range from 1.0 to 20.0. A higher value is appropriate when the features are spatially similar. Smaller values create smoother outputs. If the output does not identify enough features, then raise the value. If it identifies too many features then lower the value.

(3) Min Segment Size: the minimum size of the raster object that will be output from the image segmentation process. Area is measured in no units but the pixel itself. The default value is set to 100.

APPENDIX B: ANALYSIS TOOLSET CODES

```
import arcpy
from arcpy.sa import *
import os
arcpy.ClearWorkspaceCache_management()
arcpy.env.overwriteOutput = True
class Toolbox(object):
    def __init__(self):
        """Bridge Inspection Toolbox."""
        self.label = "Bridge Inspection Toolbox"
        self.alias = "Bridge Inspection Toolbox"

        # List of tool classes associated with this toolbox
        self.tools = [CrackHeightEnhancement,DelaminationDetectionTool]



class CrackHeightEnhancement(object):
    def __init__(self):
        """Enhances Crack Height"""
        self.label = "Cracking Detection Tool"
        self.description = "This tool can be used to detect cracks on the wearing surface of a bridge deck."
        self.canRunInBackground = False

    def getParameterInfo(self):
        """Define parameter definitions"""
        dsm = arcpy.Parameter(
        displayName="DSM",
        name="DSM",
        datatype="DEFile",
```

```
        parameterType="Required",
        direction="Input")

        orthophoto = arcpy.Parameter(
        displayName="Orthophoto",
        name="Orthophoto",
        datatype="DEFile",
        parameterType="Required",
        direction="Input")

        output_folder = arcpy.Parameter(
        displayName="Output Folder",
        name="Output Folder",
        datatype="DEFolder",
        parameterType="Required",
        direction="Input")

        parameters=[dsm,orthophoto,output_folder]

        return parameters

    def isLicensed(self):
        """Set whether tool is licensed to execute."""
        return True

    def updateParameters(self, parameters):
        """Modify the values and properties of parameters before internal
        validation is performed.  This method is called whenever a parameter
        has been changed."""
        return
```

```
    def updateMessages(self, parameters):
        """Modify the messages created by internal validation for each tool
        parameter.  This method is called after internal validation."""
        return

    def execute(self, parameters, messages):
        """The source code of the tool."""
        arcpy.AddMessage("Creating Hillshades")
        dsm=parameters[0].valueAsText
        orthophoto=parameters[1].valueAsText
        output_folder=parameters[2].valueAsText
        azimuth=45
        hillshade_list=[]
        while azimuth<=360:

            outRaster=os.path.join(output_folder,"hillshade"+str(azimuth)+'.img')
            arcpy.AddMessage("Creating Hillshade for azimuth:"+str(azimuth))
            hillshade_list.append(outRaster)
            arcpy.HillShade_3d(dsm, outRaster, azimuth, 45, False, 4)

            azimuth=azimuth+45
        arcpy.AddMessage("Creating Hillshade Average")

        hillshade_average = (Raster(hillshade_list[0]) + Raster(hillshade_list[1])+
Raster(hillshade_list[2])+ Raster(hillshade_list[3])+ Raster(hillshade_list[4])+
Raster(hillshade_list[5])+ Raster(hillshade_list[6])+ Raster(hillshade_list[7])) / 8



        #Orthophoto Albedo
```

```
        arcpy.AddMessage("Creating Orthophoto Average")
        orthophoto_average = CellStatistics(orthophoto, "MEAN", "DATA")
        #final
        arcpy.AddMessage("Creating Hillshade-Orthophoto Average")
        outFinal=(orthophoto_average+hillshade_average)/2

        enhanced_crack=os.path.join(output_folder,"enhanced_crack.img")
        outFinal.save(enhanced_crack)

        arcpy.AddMessage("Creating 5X5 Statistics")
        max5x5_out=FocalStatistics(dsm,NbrRectangle(5,5,'CELL'),'MAXIMUM',True)
        diff_mm=(max5x5_out-Raster(dsm))*1000
        arcpy.AddMessage("Creating diff_mm_cracks.img")
        outSetNull = SetNull(diff_mm,diff_mm, "VALUE >16")
        diff_mm_cracks=os.path.join(output_folder,"diff_mm_cracks.img")
        outSetNull.save(diff_mm_cracks)

        arcpy.AddMessage("Cleaning up Hillshade Files.")
        for hs_file in hillshade_list:
            arcpy.Delete_management(hs_file)

        return

class DelaminationDetectionTool(object):
    def __init__(self):
        """Define the tool (tool name is the name of the class)."""
        self.label = "Delamination Detection Tool"
        self.description = "This tool can be used to detect delamination on the subsurface of a bridge
deck."
        self.canRunInBackground = False
```

```
def getParameterInfo(self):
    """Define parameter definitions"""
    tir_image = arcpy.Parameter(
        displayName="TIR Image",
        name="TIR Image",
        datatype="DEFile",
        parameterType="Required",
        direction="Input")

    output_folder = arcpy.Parameter(
        displayName="Output Folder",
        name="Output Folder",
        datatype="DEFolder",
        parameterType="Required",
        direction="Input")

    spectral_detail = arcpy.Parameter(
        displayName="Spectral Detail",
        name="spectral_detail",
        datatype="GPDouble",
        parameterType="Optional",
        direction="Input", )
    spectral_detail.value =20

    spatial_detail = arcpy.Parameter(
        displayName="Spatial Detail",
        name="spatial_detail",
        datatype="GPLong",
        parameterType="Optional",
```

```
        direction="Input", )
    spatial_detail.value = 20

    min_segment_size = arcpy.Parameter(
        displayName="Min Segment Size",
        name="min_segment_size",
        datatype="GPLong",
        parameterType="Optional",
        direction="Input", )

    min_segment_size.value = 100



    parameters=[tir_image,output_folder,spectral_detail,spatial_detail,min_segment_size]
    return parameters

def isLicensed(self):
    """Set whether tool is licensed to execute."""
    return True

def updateParameters(self, parameters):
    """Modify the values and properties of parameters before internal
    validation is performed.  This method is called whenever a parameter
    has been changed."""
    return

def updateMessages(self, parameters):
    """Modify the messages created by internal validation for each tool
    parameter.  This method is called after internal validation."""
    return
```

```
    def execute(self, parameters, messages):
        """The source code of the tool."""
        tir_image=parameters[0].valueAsText
        output_folder=parameters[1].valueAsText
        spectral_detail=parameters[2].valueAsText
        spatial_detail=parameters[3].valueAsText
        min_segment_size=parameters[4].valueAsText
        Component_2='Component_2'
        arcpy.AddMessage("Running Pricipal Components on Thermal Image.")
        outPrincipalComp = PrincipalComponents(tir_image, 3)
        arcpy.AddMessage("Building Raster Layer for Component 2")
        arcpy.MakeRasterLayer_management(outPrincipalComp, Component_2, "", "", "2")
        arcpy.AddMessage("Running Segment Mean Shift on Component 2 Layer")
        seg_raster = SegmentMeanShift(Component_2, spectral_detail, spatial_detail,
min_segment_size,"")
        arcpy.AddMessage("Setting any Value Greater Than 125 to 1 and All Others to 0")
        segments_con=Con(seg_raster,1,0,"Value>125")
        arcpy.AddMessage("Setting all 0 Values to Null")
        delamination_raster = SetNull(segments_con, segments_con, "VALUE = 0")
        arcpy.AddMessage("Crating Polygon of all true (1) values:")
        delamination_polygon=os.path.join(output_folder,'Delamination_Polygon.shp')
        arcpy.RasterToPolygon_conversion(delamination_raster, delamination_polygon,
"SIMPLIFY","VALUE")
        return
```